

Structural Behaviour of Mechanical Connections in Weld-Free Modular Aluminum Bridge Decks

by

Melanie Perreault

A thesis
presented to the University of Waterloo
in fulfillment of the
thesis requirement for the degree of
Master of Applied Science
in
Civil Engineering

Waterloo, Ontario, Canada, 2020

© Melanie Perreault 2020

I hereby declare that I am the sole author of this thesis. This is a true copy of the thesis, including any required final revisions, as accepted by my examiners.

I understand that my thesis may be made electronically available to the public.

Abstract

This research was done in collaboration with MAADI Group Inc. who designs and fabricates aluminum bridges. Aluminum in bridge engineering is effective since it is a lightweight and highly corrosion-resistant material. MAADI Group Inc. recently unveiled a new bridge deck product called GuarDeck®[®], which was designed for installation on steel girder bridges for pedestrians and occasional maintenance vehicle use. The structural behaviour of this new deck product is the focus of this research and in particular, the mechanical connections.

The mechanical connections distinguish GuarDeck®[®] from other aluminum deck products, which typically have welded components while GuarDeck®[®] has none. GuarDeck®[®] is composed of long extruded beams that are placed perpendicular to the flow of traffic and girders. The extruded beams are connected to form a continuous surface using tongue and groove connections that are part of the extruded cross-section. The deck is held in contact with the girders using stainless steel T-bolts and extruded aluminum clamps. The tightened bolt forces the deck and clamp to “sandwich” the top flange of the girder. No on-site drilling or welding is required. An isolation layer is applied to the clamps and beams to prevent galvanic corrosion between aluminum and steel.

Experimental testing of the deck components in a laboratory setting under static loading was conducted. Two types of tests were performed: beam tests and clamp tests. The beam tests consisted of testing one or multiple simply supported, extruded beams with a point load in the middle of the span. The point load was representative of a small truck tire and smaller than the width of an extruded beam. The location of the tire load on the middle cross-section was varied. One beam tested by itself failed due to the rupture of the tension flange. Two beams connected resulted in either rupture of the tension flange or failure of the tongue and groove connection depending on the location of the tire load. Three beams with the load in the middle resulted in connection failure and a short beam held between two normal beams also failed due to the connection. A short beam was lastly tested by itself, which did not have a typical slender beam failure and failed by rupture of the top flange due to shear stress.

The clamp tests were designed to test the deck-to-girder (DG) connections. Since the girder is sandwiched between the deck and clamp, friction between these components provide the resistance to applied forces such as longitudinal thermal expansion and vehicle braking. The tests determined the capacity of the connection in this direction. Additionally, isolation layers are applied to aluminum/steel interfaces which is nearly every interface in the DG connection. Two surface finishes on the steel plate were tested. The finishes were

mill scale and sandblasted. The results showed that the connection reached a peak load then decreased gradually. The isolation layer was worn down and dust was observed beneath the specimens. Sandblasted specimens resulted in higher peak loads than the mill scale specimens.

The beam test results were compared to predictions made using theoretical structural analysis methods. The tests were first compared to predictions made using the Canadian design code for aluminum structures (CSA S157) and then two types of finite element (FE) models. The first FE model was a three-dimensional model of the experiment made with two-dimensional shell elements, where only the overall shape of the extrusion was modelled. The second was also three-dimensional, but made with three-dimensional brick elements. This model represented the extrusion in nearly its entirety, including the tongue and groove connections. The design code calculations were found to be conservative. The shell models were effective at determining the peak load when the failure mode was tension flange rupture and the brick models were effective in predicting the peak load when tongue and groove connection failure governed the capacity.

The clamp tests were compared to mechanics-based, design calculations and an FE model with brick elements, which were based on several design considerations including torque-wrenching for tightening bolts and an assumed friction coefficient. The peak loads from testing were all higher than the calculated and FE model results.

Thermal expansion is particularly important to the design of a bridge with GuarDeck® or a similar deck product because the aluminum deck will expand approximately twice as much as the steel girders. Generally, the deck will either need to resist the forces caused by restricted thermal expansion or the DG connections must allow the change in geometry but resist other forces such as vehicle braking. An analytical parametric study was conducted to determine how geometry, temperature, and vehicle braking affect the DG reactions using a linear-elastic FE model of a steel girder with an aluminum plate, representing the deck, connected using linear spring elements. The goal was to develop a means to determine DG reactions as a function of the linear connection stiffness and the various parameters mentioned using empirical equations. The results of the preliminary study showed that geometric changes to the bridge cross-section have a non-linear influence on the DG reactions. In contrast, the effect of changing the temperature parameters is linear and changing the value of the temperature gradient have practically no effect. The braking force results in the highest DG reaction when the vehicle is entering the bridge.

Acknowledgements

I need to thank my supervisor Professor Scott Walbridge for the opportunity to do this master's and for everything that came with it. I was able to work on a project I wanted, which was testing large-scale structures for something very industry-relevant. My specimens didn't end up being all that large but at least I could move them around somewhat easily. My professor sent me to Japan for an international aluminum conference which is most certainly the highlight of this degree. Professor Walbridge provided support and mentoring throughout this degree and I couldn't be more grateful.

I would like to thank MAADI Group Inc. and the Natural Science and Engineering Research Council of Canada (NSERC) for funding this research. In particular, I need to thank MAADI Group Inc. for providing input into the work to ensure it remained industry-relevant. I look forward to one day visiting the bridge that was used as a case study for this work.

I would like to thank the Civil Engineering Structures Laboratory technicians; Richard Morrison, Doug Hirst, and Peter Volcic as well as Victor Lewis for all their help. I would often be scrambling to get things done for research or for the steel bridge design team and they would always give me a hand when needed. They gave plenty of expertise and assistance throughout all the time I spent in the lab in the last few years. In addition, I would like to acknowledge the Steel Bridge Design Team for which I learned about steel fabrication, the most interesting of which was welding, and was able to go to several competition with a lot of great people.

There are many other people I'd like to acknowledge throughout my time at Waterloo, which is a long time since I did undergrad here as well. I want to thank my friends from undergrad who remind me of how grateful I am to be in grad school. I need to acknowledge the friends I made in grad school who were the highlight of many days, always willing to lend a hand, and most of which came together to form a great but unskilled dodgeball team named "Team Haas". I need to thank my friends outside of the university who also helped make the last two years amazing. Lastly, I need to thank my parents for always supporting me in all my endeavours.

My master's degree has been a fantastic experience in every way and although the COVID-19 pandemic was a bit of a downer and I would have gone to the CSCE conference in Saskatoon if not for it, it hasn't changed a thing and I'm looking forward to new challenges in the future.

Table of Contents

List of Tables	x
List of Figures	xii
1 Introduction	1
1.1 Objectives	2
1.2 Scope	2
1.3 Thesis Organization	3
2 Literature Review	4
2.1 Aluminum Bridges	4
2.2 Modular Aluminum Bridge Deck Products	6
2.3 GuarDeck®	8
2.4 Previous Aluminum Bridge Deck Analyses	10
2.4.1 FE Modelling of Bridge Deck Products	10
2.4.2 Experimental Testing of Bridge Deck Products	13
2.5 Relevant Applied Forces	16
2.5.1 Maintenance Vehicle Load	16
2.5.2 Thermal Expansion	19
2.5.3 Vehicle Braking	21

3	Experimental Program	23
3.1	Beam Tests	23
3.1.1	Load Requirements	24
3.1.2	Beam Terminology	24
3.1.3	2 m Span	25
3.1.4	650 mm Span (1B-T-S)	26
3.2	Clamp Tests	29
3.2.1	Experimental Layout	29
3.2.2	Surface Finishes and Test Matrix	31
4	Experimental Results	33
4.1	Beam Tests	33
4.2	Clamp Tests	39
5	Analysis of Results	43
5.1	Beam Tests	43
5.1.1	Comparison of Beam Test Results	43
5.1.2	Aluminum Properties	45
5.1.3	Theoretical Analysis Results	47
5.1.4	Discussion of Theoretical Results	58
5.2	Clamp Tests	62
6	Deck-to-Girder Connections	69
6.1	FE Model	69
6.2	Thermal and Braking Parameters	71
6.3	Thermal Analysis	71
6.4	Braking Force	78
6.5	GuarDeck® Example	81

7	Conclusions & Recommendations	83
7.1	Conclusions	83
7.1.1	Experimental Testing of the Beams	83
7.1.2	Experimental Testing of the DG Connections	84
7.1.3	Beam Tests Compared to Design Provisions and FE Analysis	84
7.1.4	Clamp Tests Compared to Design Provisions and FE Analysis	86
7.1.5	DG Reactions under Thermal and Braking Loads	86
7.2	Recommendations	87
7.2.1	Experimental Testing of the Beams	87
7.2.2	Experimental Testing of the DG Connections	88
7.2.3	Beam Tests Compared to Design Provisions and FE Analysis	89
7.2.4	Clamp Tests Compared to Design Provisions and FE Analysis	89
7.2.5	DG Reactions under Thermal and Braking Loads	90
	References	91
	APPENDICES	94
A	Experimental Results	95
A.1	Beam Tests	95
A.2	Clamp Tests	100
B	Beam Calculations	106
B.1	Sample Calculation	106
B.1.1	Bending	106
B.1.2	Shear	108
B.1.3	Bearing	109
B.2	CSA S157 Properties and Resistance Factors	112
B.3	Mill Certificate Properties and Resistance Factors Set to Unity	116

C Deck-to-Girder Parametric Study Results	120
C.1 Thermal Expansion	120
C.2 Vehicle Braking	128

List of Tables

2.1	Maximum and minimum effective temperatures [5].	20
3.1	Static beam test matrix.	28
3.2	Clamp test matrix.	32
4.1	Clamp test results.	39
5.1	Initial elastic stiffness.	45
5.2	Aluminum properties for theoretical analysis.	46
5.3	Simply-supported beam calculations for Tests 1B-T-L and 1B-T-S.	49
5.4	Peak load reported for each analysis method.	51
5.5	Corresponding vertical displacement reported for each analysis method.	51
5.6	Friction coefficient for static clamp tests from design calculations.	63
5.7	Friction coefficient for static clamp tests from FE analysis.	67
6.1	Secant stiffness for static clamp tests.	82
B.1	CSA S157 calculations for 1B-T with CSA S157 material properties.	112
B.2	CSA S157 calculations for 2B-T & 2B-G with CSA S157 material properties.	113
B.3	CSA S157 calculations for 3B-M with CSA S157 material properties.	114
B.4	CSA S157 calculations for 650 mm with CSA S157 material properties.	115
B.5	CSA S157 calculations for 1B-T with mill certificate material properties.	116

B.6	CSA S157 calculations for 2B-T & 2B-G with mill certificate material properties.	117
B.7	CSA S157 calculations for 3B-M with mill certificate material properties. . .	118
B.8	CSA S157 calculations for 650 mm with mill certificate material properties.	119
C.1	Spring force in N with large cross-section and varying deck width (Part 1).	121
C.2	Spring force in N with large cross-section and varying deck width (Part 2).	122
C.3	Spring force in N with large cross-section and varying deck width (Part 3).	123
C.4	Spring force in N with large cross-section and varying deck thickness. . . .	124
C.5	Spring force in N with large cross-section and constant deck area.	125
C.6	Spring force in N with large cross-section and varying span length.	126
C.7	Spring force in N with small cross-section and varying deck thickness and deck width.	127
C.8	Spring force in N with large cross-section and varying vehicle location (Part 1).	129
C.9	Spring force in N with large cross-section and varying vehicle location (Part 2).	130
C.10	Spring force in N with large cross-section, vehicle braking at middle location, and varying span length.	131
C.11	Spring force in N with large cross-section, vehicle braking at arriving location, and varying span length.	132
C.12	Spring force in N with large cross-section, vehicle braking at arriving location, and varying deck width.	133
C.13	Spring force in N with large cross-section, vehicle braking at arriving location, and varying deck thickness.	134
C.14	Spring force in N with small cross-section, vehicle braking at arriving location, and varying deck thickness and deck width.	135

List of Figures

2.1	Cross-sections for several extruded bridge decks. [29]	7
2.2	GuarDeck® installed in a pedestrian bridge in Iles-de Boucherville National Park [11].	9
2.3	GuarDeck® cross-section.	9
2.4	Configuration of installed clamp [12].	9
2.5	Isolation layer on a clamp.	10
2.6	FE modelling of Swedish deck using grillage analogy [1].	11
2.7	FE modelling of Polish deck using shell elements [29].	12
2.8	Bolts shearing due to thermal expansion from Leclerc’s analysis [15].	13
2.9	Polish bridge deck system. [29]	15
2.10	Maintenance vehicle load [5].	17
2.11	CL3-W where $W = 625$ kN [5].	18
2.12	Parameters for thermal expansion of bridges [5].	20
2.13	Braking force fraction as a function of stopping distance.	22
3.1	Beam cross-section terminology.	25
3.2	Support clamps for preventing uplift of the beam.	26
3.3	650 mm span test before loading.	27
3.4	Layout of the GuarDeck® DG connection [12].	29
3.5	Experimental layout before testing.	30

3.6	Pots were used for measuring relative displacement between top and bottom plates.	31
4.1	Results of Test 1B-T-L.	34
4.2	Results of Test 2B-T.	34
4.3	Results of Test 2B-G.	35
4.4	Results of Test 3B-M.	35
4.5	Cracked tongue in Test 3B-M.	36
4.6	Results of Test 2L1S-M Attempt 1.	36
4.7	Problem and solution to supports lifting during Test 2L1S-M.	37
4.8	Results of Test 2L1S-M Attempt 2.	37
4.9	Results of Test 1B-T-S.	38
4.10	Buckled web under point load.	38
4.11	Results of MS clamp tests.	40
4.12	Results of SB clamp tests.	40
4.13	Unedited actuator data for Test S-SB-3.	41
4.14	Blue and grey dust accumulated under the experiment.	41
4.15	Results of visual inspection proceeding the clamp tests.	42
5.1	Comparison of all beam tests from Section 4.1.	44
5.2	Ultimate strain, ultimate stress, and yield stress for the beam test specimens.	45
5.3	Stress-strain curve used for theoretical analysis.	46
5.4	Two types of FE models.	50
5.5	Results of Test 1B-T-L theoretical analyses.	52
5.6	Results of Test 2B-T theoretical analyses.	53
5.7	Results of Test 2B-G theoretical analyses.	54
5.8	Results of Test 3B-M theoretical analyses.	55
5.9	Results of Test 2L1S-M theoretical analyses.	56
5.10	Results of Test 1B-T-S theoretical analyses.	57

5.11	Middle cross-section of brick models for Tests 2B-T, 2B-G, and 3B-M at the peak load. Von Mises stress with units of MPa is shown.	59
5.12	Close-up of tongue and groove connection for Test 3B-M at peak load. Von Mises stress with units of MPa is shown.	60
5.13	Middle cross-section of shell and brick models for Test 3B-M at the peak load. Von Mises stress with units of MPa is shown.	60
5.14	Comparison of shear force and deformed shape.	61
5.15	FE model for simulating clamp tests.	64
5.16	Stress and deformation of the model under 10 kN of load.	66
5.17	The high Von Mises stress (Units of MPa) between the clamp edge & steel is shown as a spot of red.	67
5.18	Comparison of the applied, normal, and friction forces plotted against the displacement of the steel.	68
6.1	FE model used to study DG reactions under applied loads.	70
6.2	Results of the case study FE model under thermal expansion conditions for Montreal ($k \rightarrow \infty$, $w = 1372$ mm, $t = 6$ mm).	72
6.3	Maximum spring force as a function of deck width.	73
6.4	Maximum spring force as a function of deck thickness.	74
6.5	Maximum spring force as a function of deck cross-section area with infinite spring stiffness ($k \rightarrow \infty$).	75
6.6	Maximum spring force as a function of maximum temperature difference.	76
6.7	Maximum spring force as a function of temperature gradient.	77
6.8	Gravity force (53.1 kN) and braking force (13.1 kN) at three locations on the case study bridge.	78
6.9	Maximum spring force as a function of vehicle location.	79
6.10	Spring forces due to gravity and braking along the length of a 5 m case study bridge.	80
6.11	S-SB-2 secant stiffness.	82
A.1	Load-displacement graph for Test 1B-T-L.	95

A.2	Load-displacement graph for Test 2B-T.	96
A.3	Load-displacement graph for Test 2B-G.	96
A.4	Load-displacement graph for Test 3B-M.	97
A.5	Load-displacement graph for Test 2L1S-M attempt 1.	97
A.6	Load-displacement graph for Test 2L1S-M attempt 2.	98
A.7	Load-displacement graph for Test 1B-T-S.	98
A.8	Comparison of all beam tests.	99
A.9	Load-displacement graph for S-MS-1.	100
A.10	Load-displacement graph for S-MS-2.	101
A.11	Load-displacement graph for S-MS-3.	102
A.12	Load-displacement graph for S-SB-1.	103
A.13	Load-displacement graph for S-SB-2.	104
A.14	Load-displacement graph for S-SB-3.	105

Chapter 1

Introduction

In 2007, Statistics Canada reported that Canadian bridges and overpasses accounted for 8% of total infrastructure investments, \$286.2 billion, where the average age of the bridges and overpasses is 24.5 years and the mean service life is 43.3 years [4]. A market study from 2013 reported that Canada has 56,000 public roadway bridges and 25% of them are structurally deficient [32]. From these numbers, it is easy to see that bridges are expensive, used for decades, and many are deteriorated. Bridge owners are always looking to minimize their costs, initially and over the lifecycle, but are not always quick to adopt new solutions. Such is the case of aluminum in bridges, which can be readily designed to minimize lifecycle costs (e.g. no repainting) and to be assembled quickly (i.e. accelerated bridge construction). Canada produces 2.9 million tons of primary aluminum a year [20] but whenever a person is questioned, they rarely have noticed an aluminum bridge. Aluminum can be advantageous over other materials in structural engineering applications as it is more corrosion-resistant than steel, and much lighter than steel or concrete, among other reasons. Aluminum structural design is less straight-forward than for traditional materials since aluminum does not have the history that steel and concrete have.

This research was conducted in collaboration with MAADI Group Inc. who design and produce large aluminum products such as bridges. They produced a new product called GuarDeck®[®], which is an aluminum bridge deck that can be installed over steel girders. It was designed to replace deteriorated decks of pedestrian bridges where if a concrete deck is replaced, the dead load will decrease.

As is typical of engineering design, the most complicated aspects are not the large members but what connects them. GuarDeck®[®] is different from similar products in that it does not contain any welding. The members are held together using mechanical connections,

which contribute significantly to the complexity of the deck. The goal of this research is to validate the new bridge deck in a laboratory setting (i.e. by experimental testing) and use theoretical analysis methods to aid in simplifying future aluminum bridge deck designs, particularly with regards to mechanical connections.

1.1 Objectives

The primary goal of this research is to validate a new aluminum bridge deck product designed by MAADI Group Inc. with experimental and theoretical methods. Using this information, a second goal is to develop concepts to aid in the design of similar products or bridges that use similar products. The specific objectives of this research are as follows:

1. perform experimental testing of GuarDeck® panels;
2. perform experimental testing of GuarDeck® deck-to-girder (DG) connections;
3. theoretically analyze the deck product using mechanics principles, such as those described in CSA S157: Strength Design in Aluminum [6], and compare the analysis results to the experimental results;
4. theoretically analyze the deck product using commercial finite element (FE) analysis software and compare the analysis results to the experimental results; and
5. theoretically analyze the deck in a bridge to determine the DG connection forces under various applied loads.

This is a pilot study of the bridge deck product and there is no or minimal repetition of experimental testing. The purpose of the project is to observe the behaviour of the mechanical connection and determine the failure mechanisms involved in the bridge deck.

1.2 Scope

The scope of this research was limited to investigating the static behaviour of the deck and connections. At the time of writing this thesis, the COVID-19 pandemic had postponed fatigue testing of the new bridge deck for several months. Similarly, the parametric analysis presented in this research is also limited to static behaviour.

1.3 Thesis Organization

This thesis consists of seven chapters including this introduction. Brief descriptions of each chapter are provided in this section.

[Chapter 2](#) provides a review of current literature related to the work presented in this thesis. A summary of the literature on bridges with aluminum is presented, followed by a discussion of bridge deck products similar to GuarDeck® and GuarDeck® itself. A short review of research using FE analysis to model other deck products, and also previous experimental testing of aluminum decks is provided. Lastly, design loads relevant to GuarDeck® are discussed.

[Chapter 3](#) presents the experimental program, which includes two test types; beam tests and clamp tests. The beam tests consist of simply-supported beams tested to failure. The clamp tests were used to evaluate the GuarDeck® DG connections.

[Chapter 4](#) presents the experimental results for the two types of tests. Qualitative observations and quantitative results from the tests are presented.

[Chapter 5](#) contains discussion and theoretical structural analysis results for the experiments. The results of the experiments are compared to strength predictions made with structural analysis methods. The methods include CSA S157 beam calculations [6], FE models, and mechanics-based calculations.

[Chapter 6](#) covers the preliminary parametric study developed to expedite the design of bridges with aluminum decks and steel girders. As mentioned previously, the connections between members are usually the most complicated aspect of design and relationships developed in this section are intended to simplify the calculation of DG reactions.

[Chapter 7](#) summarizes the research, draws conclusions from the results, and provides recommendations to expand upon this work.

Chapter 2

Literature Review

This section summarizes literature regarding aluminum bridges and previous aluminum bridge decks similar to the bridge deck product studied in this research. Some background on the investigated deck product is then presented. Lastly, structural analysis topics are discussed including FE, experimental testing, and relevant design code provisions.

2.1 Aluminum Bridges

Aluminum bridges can be found all over the world including Canada. Siwowski [28] provides a detailed history of aluminum bridges throughout the world until 2006. For example, the first bridge with aluminum components is identified as the 1933 reconstruction of the Smithfield Street bridge in Pittsburg, USA where the wooden deck on steel stringers was replaced with an aluminum deck. Subsequently, the first bridge entirely composed of aluminum was constructed in the 1950s over the Saguenay River in Arvida, Canada. Hoglund and Nilson [8] report that Sweden had about 70 bridges in 2006 that were rehabilitated using aluminum with some new bridges being entirely aluminum. In France, aluminum was used for longitudinal and transverse girders during the rehabilitation of the historic Real Ferdinando, a 19th century suspension bridge [18]. Das and Kaufman [2] give several reasons for using aluminum in structures such as bridges:

- low density, only one third that of steel;
- strengths comparable to typical bridge steels;

- excellent corrosion-resistance, with negligible corrosion in the presence of rain and road salts;
- high toughness and resistance to low-ductility fracture, even at very low temperatures, and free of any ductile-to-brittle transition that has sometimes been fatal to older steel bridges; and
- excellent fabricability, including ease of production of extrusions to complex hollow shapes optimized for structural design and assembly.

The excellent fabricability is highlighted in extruded aluminum. Relative to steel, aluminum is a softer material, which is desirable in the fabrication of intricate cross-sections. Extrusions, aluminum or otherwise, are formed by pushing semi-solid material through a die or system of dies, which shapes the material to its final cross-section. The relative softness (i.e. low elastic modulus) of aluminum allow it to be extruded into a variety of complex and hollow shapes that would need to be machined and/or built-up if made of steel.

Of course, aluminum is as imperfect as any material. In 1996, two semi-monocoque airframe aluminum bridges in New York State required rehabilitation primarily due to galvanic corrosion between the steel and aluminum [7]. There are several reasons for the general lack of aluminum bridges in Canada. Arrien et al. [1] give several reasons for this, including but not limited to the relatively high cost of the material, lack of publications and codes, and lack of design training. However, these disadvantages can be overcome and Arrien et al. explain in the same publication that the high cost of the material, relative to steel, can be overcome if lifecycle costs are included in the decision-making process due to the corrosion-resistance of the material. For example, aluminum does not require painting and subsequent re-painting in contrast with steel. In terms of publications and codes, the structural aluminum code in Canada is CSA S157 [6]. This code was first published in 1962, but the Canadian bridge design code (i.e. CSA S6 [5]) only added provisions for aluminum in 2011 [34]. Before this, the generic code for aluminum was used for all structures. Lastly, education and training tend to focus on steel and concrete, which continue their prevalence throughout civil works. Mazzolani [19] gives several applications, including bridges, where aluminum can be superior in comparison to other materials:

- long-span roof systems where live loads are small compared to dead loads (e.g. reticulated space structures);
- construction sites far from the fabrication shop (e.g. remote regions);

- corrosive or humid environments (e.g. pool buildings);
- moving structures (e.g. retractable bridges); and
- low maintenance requirements (i.e. motorway signs).

Aluminum is not simply a replacement for more traditional materials but can be a superior option in many projects. Particularly when one of the points previously listed is involved. Most bridge projects include one or more of these aspects. For example, corrosion is an enormous problem in both steel and reinforced concrete structures, where it is less of a problem in aluminum. A natural oxide layer on the surface makes the aluminum resistant to road salts. For this reason, and other more project-dependent reasons, there has been an interest for decades to develop aluminum deck products for replacement of deteriorated or structurally obsolete bridges. [Section 2.2](#) discusses some of the bridge deck designs developed for this purpose.

2.2 Modular Aluminum Bridge Deck Products

Since aluminum is versatile with high corrosion-resistance, several extruded bridge deck products were designed over the years. Several bridge deck cross-sections are shown in [Figure 2.1](#). From top to bottom, the first cross-section is the Swedish SAPA deck product, the second is the American ALUMADECK deck product, the third is a Japanese deck product, and the last cross-section is a Dutch product. There are others, such as the American Alcoa bridge product [1]. Since cross-section widths and heights are limited by the size of the extruder, connecting the extrusions to form a surface is an essential design step. Some decks are connected using mechanical connections (e.g. SAPA) while others are welded (e.g. ALUMADECK). Welding is fantastic for creating seamless joints but is prone to fatigue, whereas mechanical fasteners are superior in that regard. Interestingly, the SAPA deck was designed to fulfil the bridge deck replacement needs of Sweden; where, similar to Canada, deteriorated bridge decks are caused by severe climate, road salts, and increasing traffic loads [30].

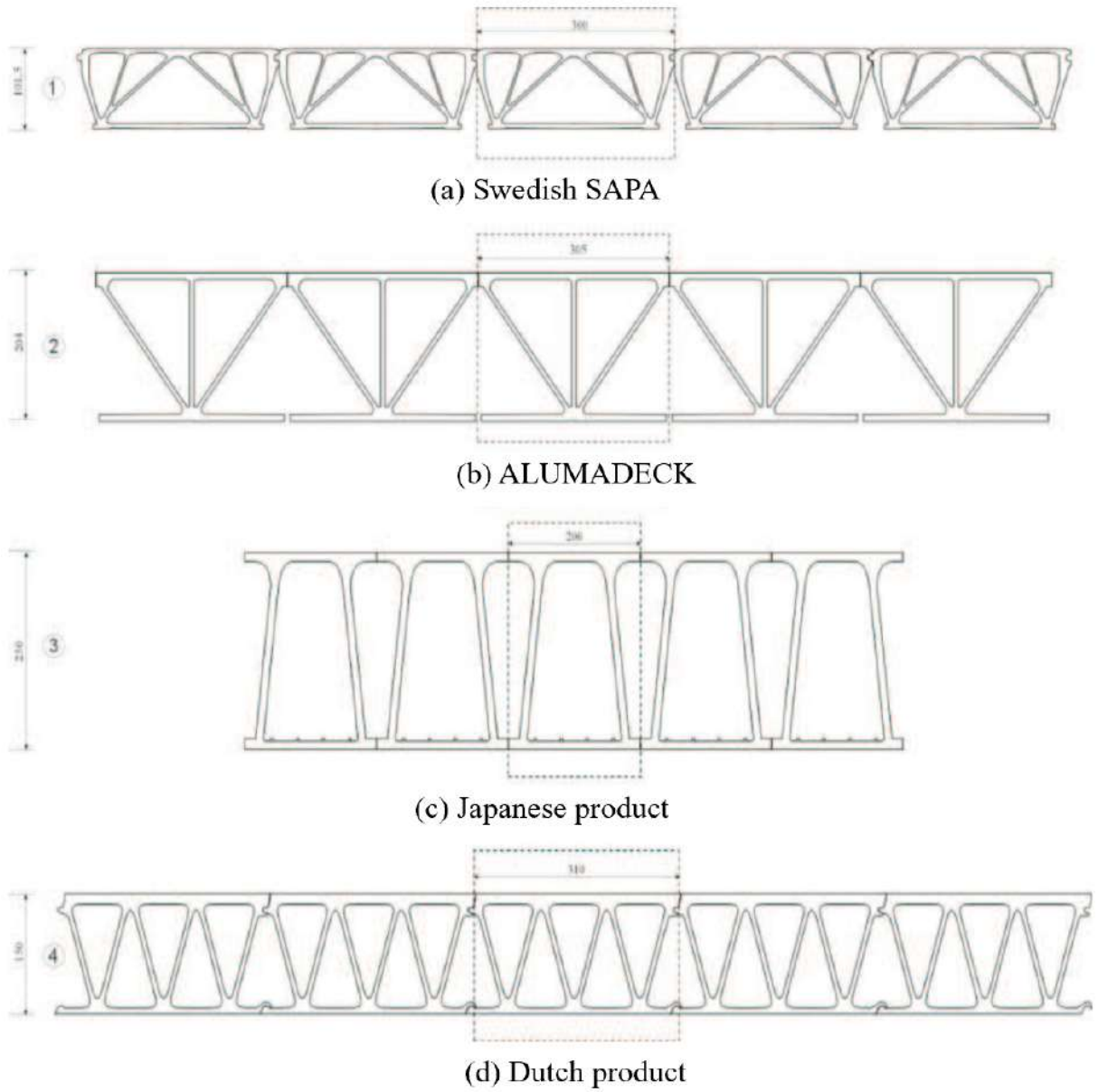


Figure 2.1: Cross-sections for several extruded bridge decks. [29]

2.3 GuarDeck®

The bridge deck studied in this thesis is the new GuarDeck® product [13] by MAADI Group Inc. The first use of the product was in a national park, where pedestrians and maintenance vehicles use it to cross a river, as shown in Figure 2.2. The deck was designed with the intentions of being quick to assemble in the field and for use in rehabilitation of pedestrian bridges. To accomplish the first intention, the bridge is mechanically fastened together, with no on-site drilling or welding at any point. Rehabilitation is possible because the deck product can be used on top of new or existing girders using mechanical connections. The deck also has all of the benefits of aluminum previously mentioned. Beyond the first use, the deck is recommended for use in other situations subject to loading requirements. Some of the other uses MAADI Group Inc. [13] suggests are:

- maritime structures;
- civil security bridges;
- temporary bridges;
- military bridges;
- industrial bridges; and
- extended roadway bridges for cantilevered bike paths.

In comparison with the bridge deck products presented in the previous section, GuarDeck® is most similar to the Swedish SAPA system. Both decks use a type of mechanical connection, commonly called a tongue and groove, to connect extruded members instead of welding.

GuarDeck® has three components plus standard fastening hardware. The deck surface is formed out of identical extruded beams, with a cross-section as shown in Figure 2.3, which are installed perpendicular to steel girders. On the left and right edges of the cross-section are a tongue and a groove, which connect to form a continuous surface. The underside of the trapezoids was designed in conjunction with the second component, T-bolts. The T-bolts are stainless steel and custom-made to directly connect to the aluminum beams. The clamps are the final component of the deck product and wrap around a girder flange when installed. The clamps press against the aluminum beam and the bolt forces the clamp in contact with the steel. This is the DG connection for the GuarDeck® system and is illustrated in Figure 2.4.



Figure 2.2: GuarDeck® installed in a pedestrian bridge in Iles-de Boucherville National Park [11].



Figure 2.3: GuarDeck® cross-section.



Figure 2.4: Configuration of installed clamp [12].

A risk of galvanic corrosion exists when the deck is used on top of steel girders, as steel is much higher than aluminum in the galvanic or electropotential series. All the aluminum parts are 6061-T6, the stainless steel bolts are 316 alloy, and the girders are likely to be mild structural steel (e.g. CSA 300W). Stainless steel bolts are required because the risk of corrosion between aluminum and stainless steel is minimal. To prevent corrosion between the deck, clamps, and girders, an isolation layer is applied to the bottom of the aluminum beams and top of the clamps. To improve friction at these interfaces, a proprietary grit material is added. Figure 2.5 shows the isolation layer installed on a clamp. The grit on the vertical area of the clamp is minimal to ensure a tight fit against the girder flange.

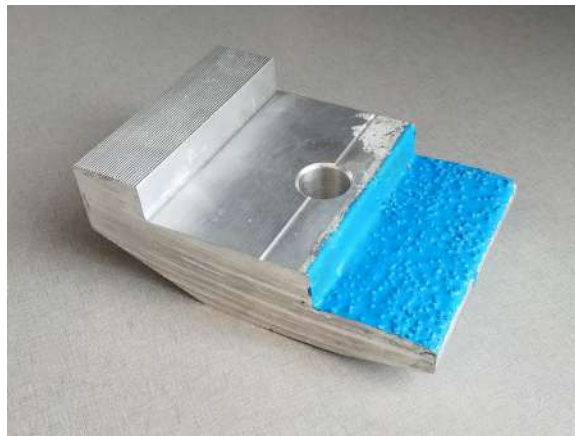


Figure 2.5: Isolation layer on a clamp.

2.4 Previous Aluminum Bridge Deck Analyses

This section summarizes previous research conducted to ensure various aluminum bridge decks perform adequately. The two topics covered are FE modelling and experimental testing.

2.4.1 FE Modelling of Bridge Deck Products

As new bridge deck products were developed over the years, structural analysis using FE evolved as well. In 1990, Svensson and Pettersson [30] used FE to simulate the SAPA extrusions as beam elements with the flexural and torsional stiffness of the deck cross-section. The interaction between extrusions was simulated using beam elements with almost

infinite flexural stiffness and hinges. The FE model described is a grillage analogy model. The load was applied as a pair of truck tires to result in the largest deformation. The model was subsequently used by Arrien et al. [1] to analyze the replacement of a wood deck with the Swedish deck. The model used by Arrien et al. is shown in Figure 2.6 and included more beam elements to represent the girders.

In 2001, Dobmeier et al. [3] modelled the ALUMADECK in three-dimensions (3D) with two-dimensional (2D), first-order quadrilateral shell elements. Since this deck requires welding between extrusions to form panels, the heat affected zone (1" or 25.4 mm on each side of the weld [17]) was made weaker than the base metal. Okura et al. [23], Vigh [33], Maljaars, Soetens and Straalen [16], Siwowski [29], and Saleem et al. [26] used variations of 2D elements to model 3D extruded aluminum deck concepts. The variations included; type of shell element, 3D elements used to apply load, and elastic-plastic material properties versus linear-elastic.

The mesh used by Siwowski [29] is shown in Figure 2.7, where the blue areas indicate the base metal and the orange areas indicate the weaker heat affected zones. Additionally, Siwowski added elements to form the curved corner shown at the bottom of the triangle in Figure 2.7. He discusses his modelling approach in comparison to what was done previously. He states that aluminum deck extrusions mostly resist loads through plate-bending mechanisms and explains that 2D shell elements are formulated specifically for modelling bending. In contrast, first-order continuum 3D brick elements have difficulty modelling pure bending and can result in numerical difficulties. Higher-order brick elements resolve this problem but are computationally expensive.

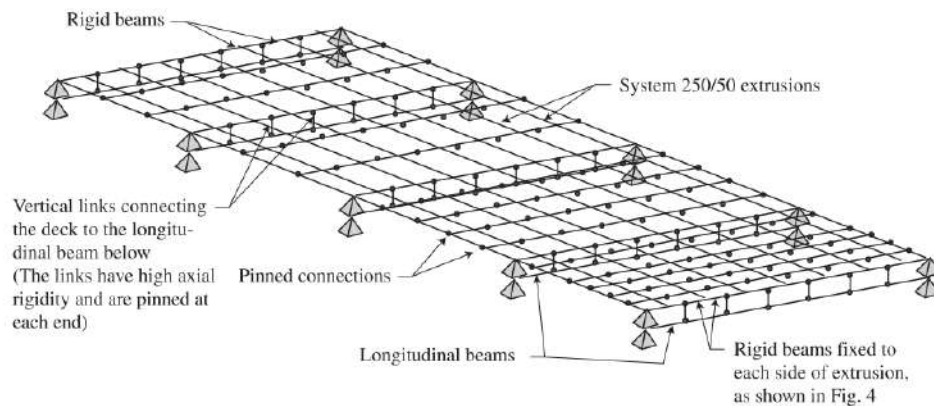


Figure 2.6: FE modelling of Swedish deck using grillage analogy [1].

More recently in 2018, Leclerc [15] used a 3D model with 3D, linear, hexahedral elements

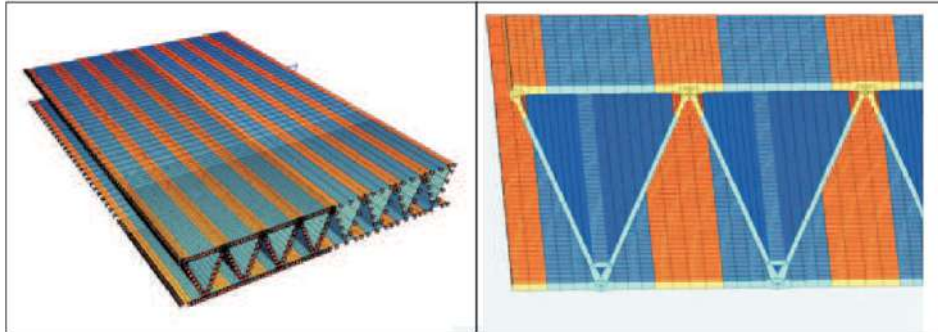


Figure 2.7: FE modelling of Polish deck using shell elements [29].

to model an aluminum deck on top of steel girders connected with bolts. His goal was to determine whether the composite bridge would be adequate to resist the induced loads due to thermal expansion. Part of the results included redesign of the bolts near the supports due to the high shear stresses predicted by the FE analysis. Example output from this analysis is shown in [Figure 2.8](#).

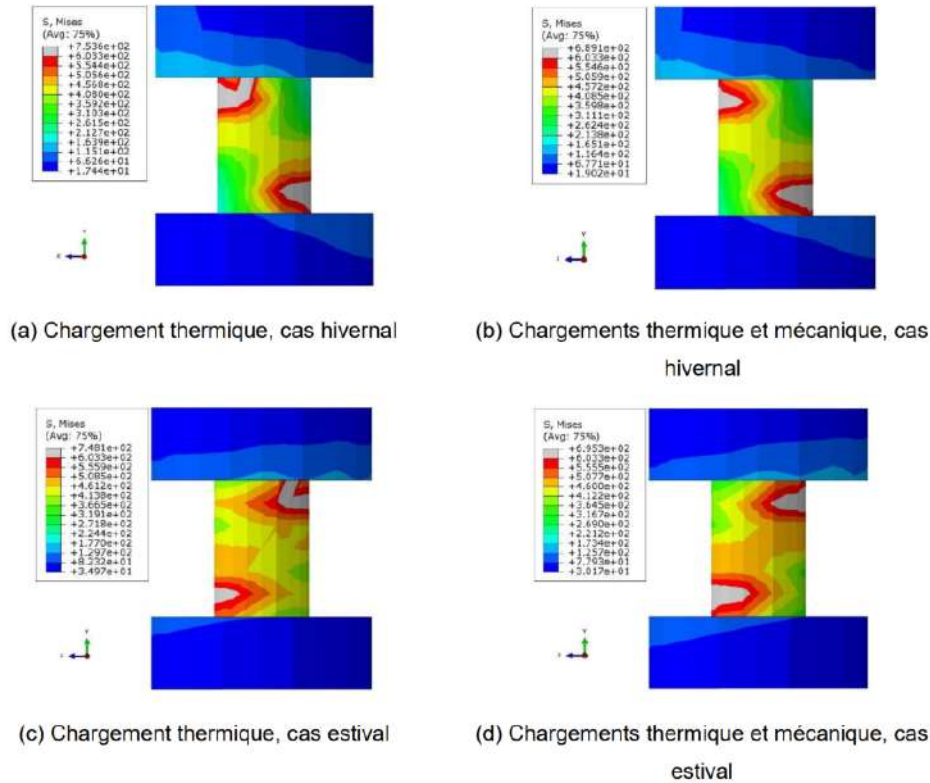


Figure 2.8: Bolts shearing due to thermal expansion from Leclerc’s analysis [15].

2.4.2 Experimental Testing of Bridge Deck Products

Experimental testing of a bridge deck system provides valuable insight concerning the structural behaviour. It is difficult to test a new aluminum bridge deck extrusion before it is ready to be produced at full-scale since extrusions require an expensive custom-made die, which is why theoretical analyses such as FE are often useful. Once a die is made and extrusions are produced, they are usually tested to ensure they perform as intended before being installed in a bridge expected to last 50 years or more. The following paragraphs discuss some of the experiments others have conducted to ensure new decks perform as intended for their purpose.

The SAPA deck was studied experimentally at full-scale [30] where the load was applied as a pair of truck tires in the most unfavourable position. The deck was tested statically to ultimate failure and dynamically to assess fatigue life. In addition to this testing, Høglund and Nilson [8] report an investigation of the SAPA deck in a -40°C cold chamber.

Saleem et al. [26] investigated the SAPA deck for use in movable bridges (i.e. bascule, swing, and lift). The key factor was weight in comparison to open grid steel decks. The weight of the new deck needed to be less than 1.2 kN/m^2 and the weight of the SAPA deck is 0.67 kN/m^2 . The Swedish deck was investigated in conjunction with a waffle shape reinforced ultra-high performance concrete (UHPC) deck and a fibre-reinforced polymer tube-UHPC composite deck. In a later study by the same authors [27], the aluminum deck was tested by itself for movable bridge applications. The test matrix consisted of:

1. Flexural test: simple-span
 - A simply supported beam with a point load in the middle of the span.
2. Flexural test: two span continuous
 - A beam with three supports tested with one point load in the middle of each span
3. Flexural test: simple-span inverted panel test
 - A simply supported bending test with a point load in the middle of the span, where the panel is upside-down (i.e. negative bending)
4. Shear test of connectors
 - A shear test where a short section of the deck is loaded from the side until the DG connections fail
5. Uplift test for connectors
 - A short section of the deck is lifted until the DG connections fail
6. Lip test (tongue and groove test)
 - A short section of the deck, placed between two simply-supported beams, is loaded until the tongue and groove connection between deck extrusions fail
7. Fatigue test
 - Three continuous beams with one point load in the middle of each span on the middle beam are loaded for 2 million cycles as per the American Association of State Highway Transportation Officials (AASHTO) requirements

8. Residual strength test

- The beams subjected to fatigue loading in the previous test were tested statically

Dobmeier et al. [3] tested nine welded ALUMADECK extrusions as a simply-supported panel, where the extrusions were parallel to the bridge girders, in contrast to the SAPA deck. The SAPA panels must be perpendicular to the girders. One and two tire loads were applied.

Siwowski [29] tested the cross-section shown in Figure 2.9a. Extrusions were welded to form a 2.1 m by 3.2 m panel where the long direction of the extrusions is aligned with the long direction of the panel. Similar to the ALUMADECK, this deck can be oriented to be parallel with the girders. The panel can provide 2-way bending or act compositely with the girders, and therefore, the panel was tested in both directions to consider both cases. Figure 2.9b shows the four test configurations that were tested at service load, ultimate load, and under dynamic loading.

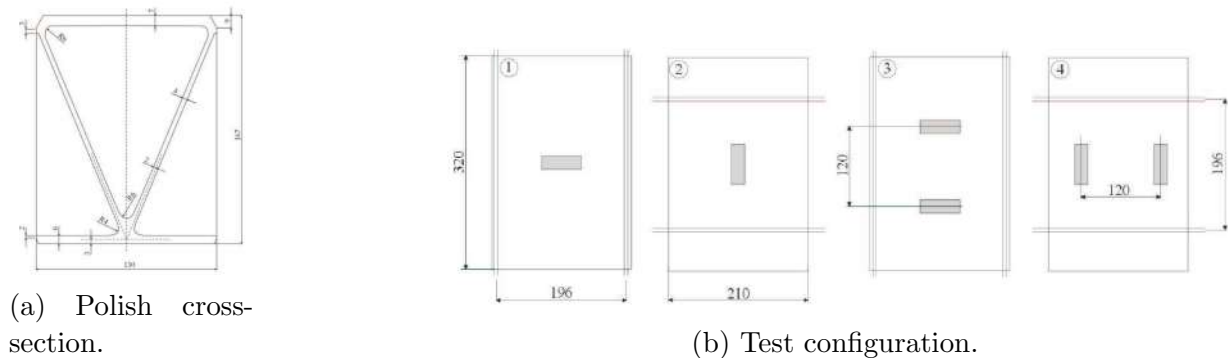


Figure 2.9: Polish bridge deck system. [29]

2.5 Relevant Applied Forces

This section focuses on determining loads of interest related to the structural analysis of GuarDeck®.

2.5.1 Maintenance Vehicle Load

Pedestrian bridges carry uniformly distributed loads caused by pedestrian traffic and the point loads caused by occasional vehicles (e.g. maintenance vehicles), but it is assumed these loads do not occur simultaneously. Vehicle loads tend to govern the design of bridges since the point loads caused by heavy vehicle wheels usually causes more stress in the bridge than the uniformly distributed load from pedestrian traffic.

Vehicle loads are typically specified by the bridge owner and can be taken as the maintenance vehicle load presented in CSA S6 [5] or the smallest truck model, CL3-W, also in CSA S6. The maintenance vehicle load is shown in Figure 2.10 and the CL3-W truck model is shown in Figure 2.11, where W is equal to 625 kN in Ontario.

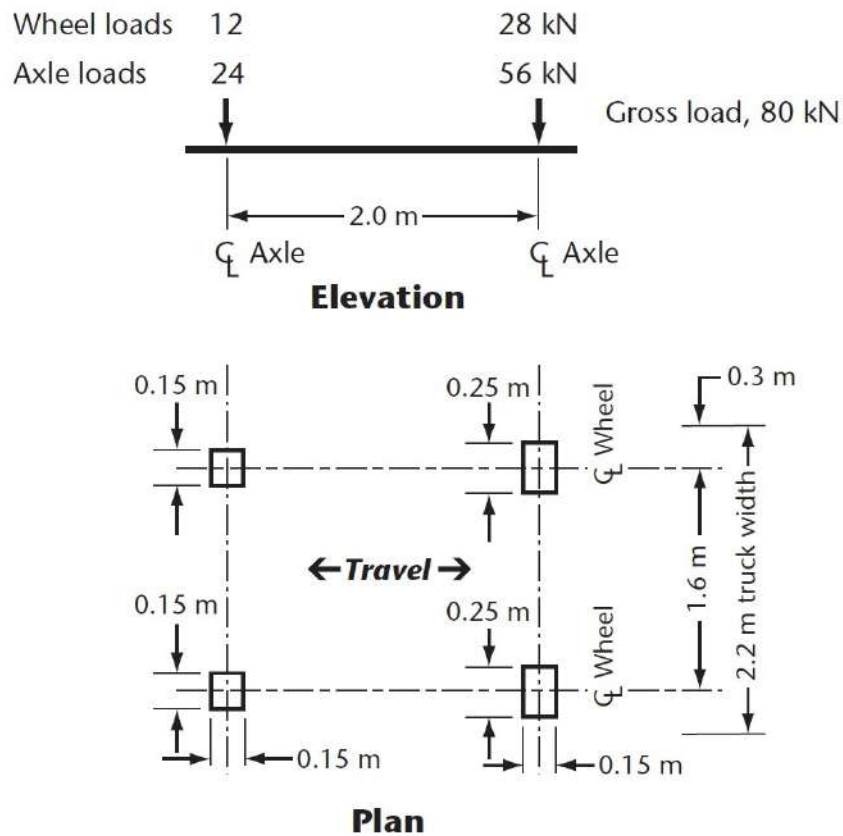
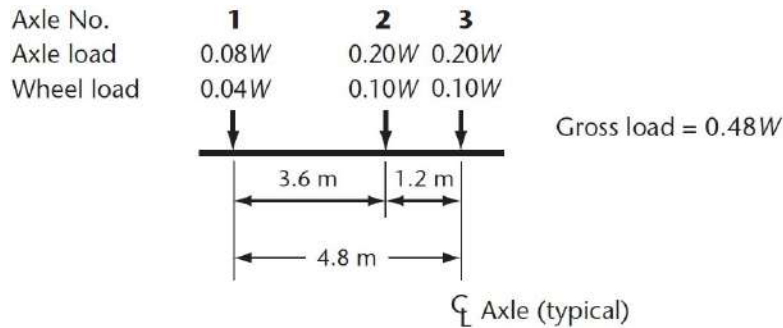
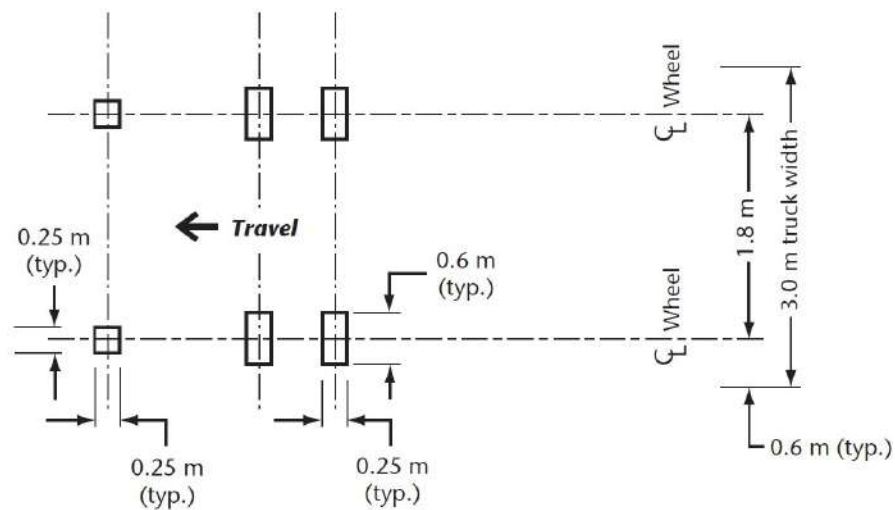


Figure 2.10: Maintenance vehicle load [5].



CL3-W Truck Load (elevation)



CL3-W Truck Load (plan)

Figure 2.11: CL3-W where $W = 625$ kN [5].

2.5.2 Thermal Expansion

In the case of composite structures made with more than one material, structural analysis of the thermal effects is more complicated. Steel and aluminum have different coefficients of thermal expansion where aluminum will expand nearly twice as much as steel. The problem is minimal in steel and concrete composite structures because the two materials have similar thermal expansion coefficients. This problem can be solved by deciding whether the structure acts compositely or not. If it is composite, the deck must resist the compression caused by restricted expansion plus other forces. Otherwise, the connections must transfer

load from the deck to the girders but not restrict expansion simultaneously, which can be a challenge with respect to connection design. Furthermore, aluminum should not be in direct contact with steel, otherwise, galvanic corrosion may occur. Contact is prevented in the GuarDeck® product by the gritty, blue coating shown in [Figure 2.5](#), but transferring load from the deck to the girders through this coating can be concerning.

One-dimensional linear thermal expansion can be calculated using [Equation 2.1](#). The coefficients for aluminum and steel are 24.0×10^{-6} mm/(mmK) and 12.7×10^{-6} mm/(mmK), respectively. Using linear-elastic relationships, the stress due to restricted expansion can be calculated. The calculation would be simple if not for other provisions in CSA S6 [5], which state that temperature is generally not uniform across a bridge’s cross-section. Applied thermal loads such as gradients are categorized into three groups where an aluminum deck on steel girders is most similar to a fully steel bridge, a Type A structure, as opposed to Type B or C, which contains concrete, a much less conductive material. Thermal expansion, as opposed to contraction, is associated with the maximum effective temperature and is determined using the maximum mean daily temperature from the annexes of CSA S6 [5] for a location of interest. The temperature is then modified using [Table 2.1](#) and further modified using [Figure 2.12a](#). The thermal gradient across the cross-section depth is determined using [Figure 2.12b](#) and is linear from the top to the bottom of the cross-section.

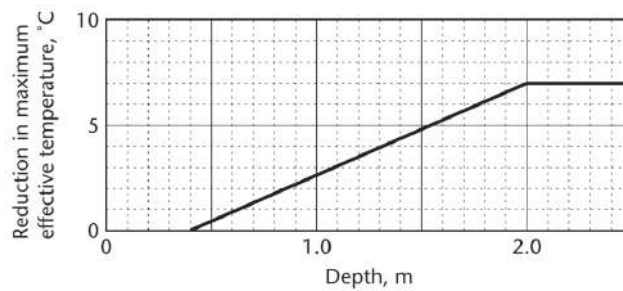
$$\Delta L = \alpha L_0 \Delta T \tag{2.1}$$

Where ΔL is the length of the expansion in mm, α is the linear thermal expansion coefficient specific to the material in mm/(mmK), L_0 is the original length in mm, and ΔT is the change in temperature in K.

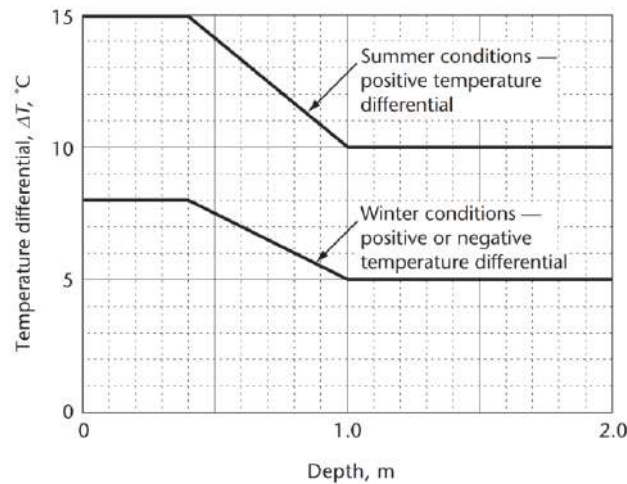
FE can be used to solve these problems where thermal expansion occurs in all directions and specified areas can have different temperatures. Leclerc [15] tackled the thermal expansion problem using FE where he looked at an aluminum deck on steel girders that was designed to act compositely.

Table 2.1: Maximum and minimum effective temperatures [5].

Superstructure type (see Clause 3.9.3.)	Maximum effective temperature	Minimum effective temperature
A	25 °C above maximum mean daily temperature	15 °C below minimum mean daily temperature
B	20 °C above maximum mean daily temperature	5 °C below minimum mean daily temperature
C	10 °C above maximum mean daily temperature	5 °C below minimum mean daily temperature



(a) Modifications to maximum effective temperature.



(b) Temperature differentials for Type A and C superstructures.

Figure 2.12: Parameters for thermal expansion of bridges [5].

2.5.3 Vehicle Braking

Recall that temperature loads can occur simultaneously with other loads such as traffic loads. Should a truck stop suddenly, this creates a horizontal force parallel to thermal expansion, traffic, and the girders. Analyzing this load case requires a braking force value. There is plenty of literature attempting to understand the dynamic effects of braking due to parameters such as surface roughness, damping, natural frequencies, vehicle weight, vehicle speed, suspension system, and more, but guidance in bridge codes will be discussed here because an equivalent static force is desired for the analysis in [Chapter 6](#). Additionally, only code provisions focusing on wheel or axle loads are discussed. The Ontario Highway Bridge Design Code (OHBDC) [\[22\]](#) provides an upper limit of 80% of the axle weight in extreme conditions. This is likely the absolute maximum horizontal force that can be transferred from the truck to the deck through friction. CSA S6 [\[5\]](#) provides an equivalent static force of 180 kN plus 10% of the uniformly distributed lane load but not more than 700 kN. Lastly, AASHTO [\[21\]](#) states that the braking force is 25% of the axle weight of the design truck. The percentage is derived from [Equation 2.2](#). The 25% in particular is based on the assumption of an initial velocity of 88.5 km/h and a corresponding stopping distance of 122 m. Braking force fractions as a function of stopping distances and speeds are plotted in [Figure 2.13](#). An upper limit of 80% or 0.8 is plotted as well. The CSA S6 provision is irrespective of speed or vehicle and is calibrated for large transport trucks on highway bridges; therefore, it is not applicable to a maintenance vehicle on a pedestrian bridge. As for the AASHTO provision, since no other speeds and stopping distances are provided and 88.5 km/h is excessive for the pedestrian bridge case, it can be assumed that a lower speed is reasonable but will result in a correspondingly smaller stopping distance resulting in a braking force fraction that is approximately 25%.

$$F_B = bW_T = \frac{v^2}{2ga}W_T \quad (2.2)$$

Where F_B is the braking force in kN, b is the braking force fraction, v is initial velocity in m/s, g is the gravitational constant in m/s², a is the stopping distance in m, and W_T is the weight of the truck in kN.

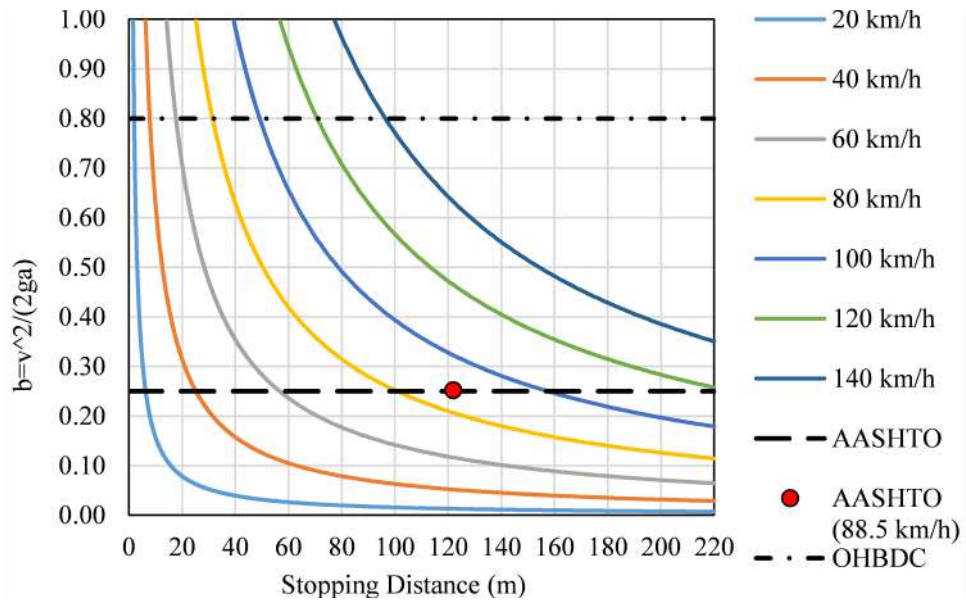


Figure 2.13: Braking force fraction as a function of stopping distance.

Chapter 3

Experimental Program

The experimental programs for the two types of tests conducted, beam tests and clamp tests, are described in this chapter. Experimental results and analyses are provided in [Chapter 4](#) and [Chapter 5](#), respectively.

3.1 Beam Tests

The goal of the beam tests is to determine the relevant failure mechanisms from a maintenance vehicle driving over the bridge deck product. No repetition of tests was done so that as many scenarios as possible could be tested. Therefore, the peak load of each test is not meant to be published as the precise strength of the GuarDeck® beams. The tests demonstrate the possible failure mechanisms that occur when the bridge deck product fails.

The beam tests consisted of a series of simply-supported GuarDeck® beams or panels that were tested under a single point load to simulate a maintenance vehicle driving over the bridge. [Section 2.4.2](#) discusses methods by other researchers to test various extruded aluminum decks, and the following experimental program is influenced primarily by the work conducted by Saleem et al. [\[27\]](#) on the SAPA deck. Some of the beam tests were presented in a conference paper for the 2020 Canadian Society for Civil Engineering (CSCE) annual conference [\[25\]](#).

3.1.1 Load Requirements

A case study bridge is used throughout this thesis for geometric properties and loading requirements. It is a 40 m simply-supported pedestrian bridge near Montreal, Quebec, and is the middle span of the bridge shown in [Figure 2.2](#). The bridge consists of the GuarDeck® system supported on three steel I-shape girders. The center-to-center spacing is approximately 1.4 m. In addition to pedestrians, the bridge can support a single maintenance vehicle. As mentioned in [Section 2.5.1](#), vehicle loads tend to govern bridge design in comparison to pedestrian loads. Therefore, a single vehicle is the primary load of interest in this study.

The minimum load requirements are calculated based on 50% of the CL3-W truck model (previously shown in [Figure 2.11](#)) as specified by the owner. The governing point load is a back tire with a force of 31.3 kN. A tire is used instead of an axle because the distance between girders is not wide enough for an axle. Including the live load factor of 1.7 from CSA S6 [5], the required force is 53.1 kN. The required load is further increased to 74.3 kN when a dynamic load allowance of 1.4 is used. The width and length of the CL3-W tire load are 250 mm by 600 mm, but these dimensions are for a tractor trailer and would cover nearly half or more of the beam span. Alternatively, the maintenance vehicle dimensions of 150 mm by 250 mm from [Figure 2.10](#) are used. Using the same load and smaller area results in higher pressure and is conservative with regards to safety. The loading rate used during testing was expected to be fast enough to prevent creep of the material. The load was displacement-controlled.

3.1.2 Beam Terminology

[Figure 3.1](#) shows the beam cross-section with its various details labelled. The underside of the trapezoids are occasionally referred to as feet, and both feet together form a rail or T-slot for the T-bolt. The middle cross-section of the beam is frequently referred to, and is shown in many figures. The cross-section at other locations, such as the supports, are reported occasionally. The span of a beam refers to the centre-to-centre distance between the supports. When two or more beams are adjacent, they are connected using the tongue and groove connections. The connections are referenced and the side of the connection of interest will be indicated by tongue side or groove side.

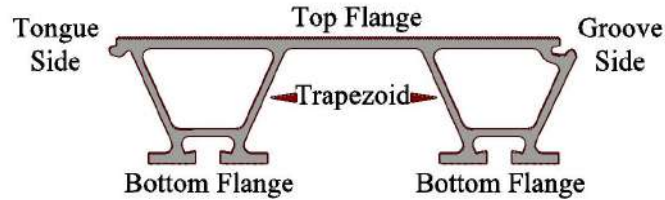


Figure 3.1: Beam cross-section terminology.

3.1.3 2 m Span

Several 2.1 m beams were tested under simply-supported conditions with a single tire load in the middle of the span. The width of the supports were 76 mm (3"), where one side represented a roller and the other side represented a pin. The pin prevented vertical and horizontal movement, while the roller prevented vertical movement. The tire load described in [Section 3.1.1](#) was applied using a steel plate on the middle cross-section of the span, where the long dimension (250 mm) was parallel to the long direction of the beam. 25 mm (1") of rubber was placed between the steel plate and the beams to prevent local crushing at the edges of the plate.

After the first two tests, support clamps were added to prevent uplift of the beam at the supports. Uplift is unusual for simply-supported beams, but the irregular shape and uneven loading caused this requirement. An installed support clamp is shown in [Figure 3.2](#).

String potentiometers (string pots or Pots) and the linear variable differential transformer (LVDT) within the actuator measured vertical displacement of the beam during testing. The actuator's internal LVDT, referred to as actuator from here on, measured displacement of the actuator and not necessarily the beam. Consequently, the actuator measured compression of the rubber pad as well as beam displacement. String pots were connected directly to the beams for accurate vertical displacement data. [Table 3.1](#) contains the number of beams, location of load, and location of string pots for each static test.

The tests used 2.1 m beams exclusively except for Test 2L1S-M. Test 2L1S-M consisted of two 2.1 m beams and a 368 mm (14.5") beam, referred to as the short beam. The middle cross-sections of all three beams were aligned beneath the load. The short beam did not touch the supports and was supported through the tongue and groove connections on both sides.



Figure 3.2: Support clamps for preventing uplift of the beam.

3.1.4 650 mm Span (1B-T-S)

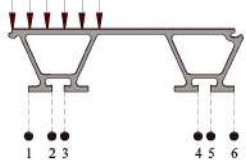
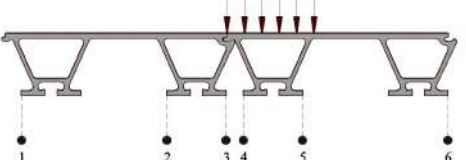
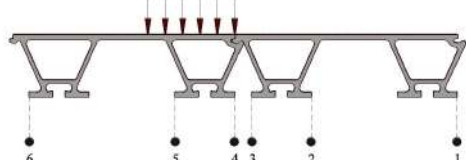
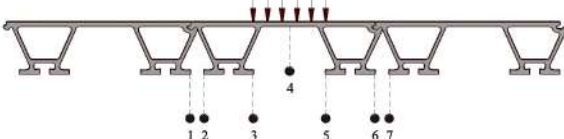
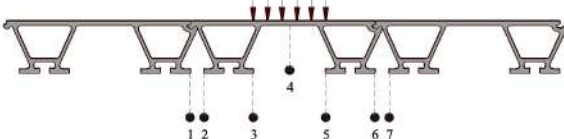

One 650 mm span test, called Test 1B-T-S, was conducted, and was much shorter than reasonable for a bridge deck (approximately half of the actual span). The width of the supports was greatly reduced from the 2 m span tests to induce a failure mode other than bending. The support width was reduced from 76 mm (3") in the 2 m span tests to 38 mm (1.5"). The support clamps were not used during this test.

The simply-supported beam was subjected to one tire load in the middle of the span and aligned with the tongue side edge. Five string pots and the actuator were used to collect vertical displacement. Four of the string pots were connected to the top flange at the intersection between the tongue side trapezoid webs and the supports, as shown in [Figure 3.3](#), because the expected failure mode was buckling of the webs under the applied load or at the supports. The fifth string pot measured displacement of the tongue, and is labelled Pot 1 in [Table 3.1](#).



Figure 3.3: 650 mm span test before loading.

Table 3.1: Static beam test matrix.

Name	Shortened Name	Load & String Pot Location at Middle Cross-section
One 2 m Span Beam with Load on Tongue Side	1B-T-L	
Two 2 m Span Beams with Load on Tongue Side	2B-T	
Two 2 m Span Beams with Load on Groove Side	2B-G	
Three 2 m Span Beams with Load in Middle	3B-M	
Two Long (2 m Span) Beams and One Short (368 mm) Beam with Load in Middle	2L1S-M	
One 650 mm Span Beam with Load on Tongue Side	1B-T-S	

3.2 Clamp Tests

The goal of the experiment is to determine peak strength of the GuarDeck® DG connection in the long direction of the bridge. The connection resists applied forces through friction in this direction, as opposed to using mechanical connections directly, which is more common. As described in Section 2.3, the DG connections consist of three components: the T-slot in the bottom flange of the beam, an extruded aluminum clamp, and a custom stainless steel T-bolt. The other required hardware includes stainless steel nuts, lock nuts, and washers. The layout of the clamping system is illustrated in Figure 3.4.



Figure 3.4: Layout of the GuarDeck® DG connection [12].

3.2.1 Experimental Layout

The experimental layout was designed to test the DG connections and minimize contributions from sources of error such as bending. The bottom flanges of a short beam section were connected to two steel plates. One steel plate was connected using bolts and the other was connected using the DG connections, as shown in Figure 3.5. Two steel angles were attached to the layout to facilitate lifting. The top flange of the beam section was reinforced with a plate of steel to prevent bending. The bolts were torqued to 190 Nm (140 lb-ft) as specified in the installation instructions, unless stated otherwise. The test consisted of the frame pulling the clamped, bottom plate out of the layout. This experimental layout remained consistent throughout the tests. The beam, fasteners, clamps, and bottom plate were replaced every test since the isolation layer and surface finish of the steel deteriorated during testing.



(a) Experiment before installation.



(b) Experiment installed in the test frame.

Figure 3.5: Experimental layout before testing.

The instrumentation consisted of two potentiometers (pots or Pots) and the actuator's LVDT, referred to as the actuator. The actuator measured displacement of the frame and not necessarily the test, which include sources of error such as grip and bolt slip. This was a problem at the beginning of the test until the DG connections engaged. The pots were used for this reason, but they could measure 10 mm of displacement at most, as shown in [Figure 3.6](#). The pots were placed to measure relative displacement between the top plate and the bottom plate. Two pots were used in case of uneven loading or displacement during testing. The reported actuator data was corrected using the pots, where the peak load of the actuator data was translated to approximately align with the peak loads of the pot data. The translation is necessary so the actuator data after the pots run out is usable.



(a) Pots before testing.



(b) Pots after 10 mm of displacement.

Figure 3.6: Pots were used for measuring relative displacement between top and bottom plates.

3.2.2 Surface Finishes and Test Matrix

Two surface finishes for the steel plates were tested: mill scale (MS) and sandblasted (SB). The bottom plate, representing the girder flange, had the surface finish being tested. The MS plates were CSA 300W structural steel. MS is not necessarily a good representation of steel girders in the field because exposed steel requires protection such as paint or galvanization. An MS finish was used because it is generally required in slip-critical connections. The MS finish was dark in colour, and smooth in texture, as is typical of this type of steel. Proceeding the MS tests, the used plates were sandblasted by the Engineering Machine Shop at the University of Waterloo for the SB specimens. The surfaces of the SB plates were inspected to ensure marks from the previous testing had been removed by sandblasting. The sides of the specimens were hardly sandblasted, but this was expected to have minimal effect since there was minimal damage during the MS tests. The surface finish

of the SB plates was light grey in colour, and rough in texture in comparison to the MS plates. Similar to the MS finish, SB finishes are not typical in bridge construction but was a contrast to the smooth texture of the MS specimens.

Each plate is named with the first letter referring to the type of testing (static (S)), the next two letters refer to the surface finish (MS or SB) and lastly, the number refers to the trial number of the test and surface finish. For example, Test S-SB-3 is the third trial of the sandblasted specimens tested under static loading. All six tests or trials are listed in [Table 3.2](#).

Table 3.2: Clamp test matrix.

Mill Scale	Sandblasted
S-MS-1	S-SB-1
S-MS-2	S-SB-2
S-MS-3	S-SB-3

Chapter 4

Experimental Results

The results of the experiments described in [Chapter 3](#) are presented in this chapter. Analysis and theoretical strength calculations are presented in [Chapter 5](#). All of the experimental results as well as larger versions of graphs in this chapter are provided in [Appendix A](#).

4.1 Beam Tests

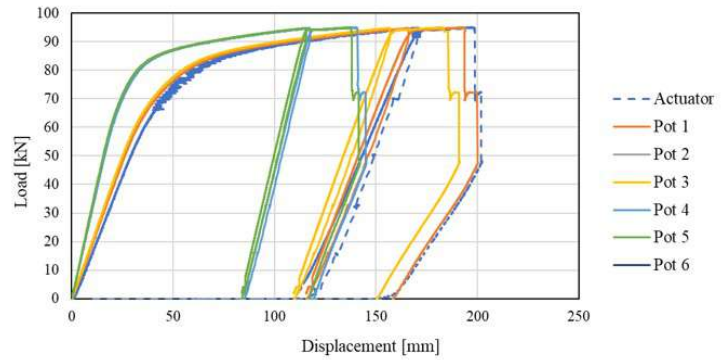
Test 1B-T-L was loaded until the peak load, where the bottom flange below the load ruptured. The tongue side foot ruptured before the adjacent foot. The peak load of the test is 95 kN with a corresponding vertical displacement of 197 mm at Pot 1. The groove side trapezoid lifted up from the supports during the test, which was prevented in the following tests by the support clamps. [Figure 4.9a](#) shows another test lifting from the supports. The ruptured bottom flange and load-displacement graph are shown in [Figure 4.1](#). Test 1B-T-L was unloaded and reloaded due to laboratory time constraints as shown in the load-displacement graph.

Similar to Test 1B-T-L, Test 2B-T failed in bending at 190 kN and a corresponding vertical displacement of 171 mm at Pot 5. The bottom flanges of the two middle trapezoids ruptured at the peak load. It is uncertain exactly which foot ruptured first since several cracks were heard before the test was stopped. Pots 3, 5, and 6 broke at the peak load. The failed beam and load-displacement graph are shown in [Figure 4.2](#).

Test 2B-G failed due to the failure of the tongue and groove connection. The connection dislocated at midspan at a peak load of 147 kN and a vertical displacement of 47 mm at Pot 5. Inspection of the connection showed minimal deformation other than to the surface



(a) Ruptured bottom flange.

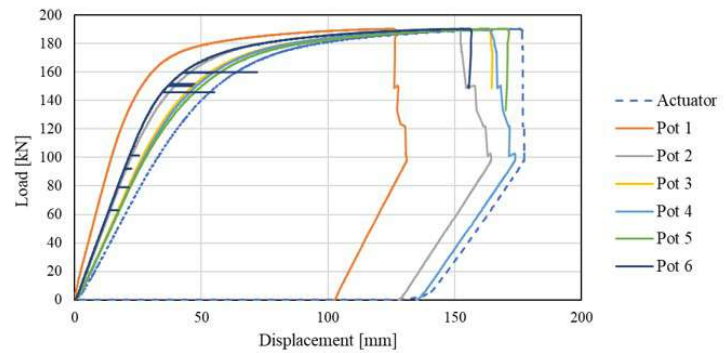


(b) Load-displacement graph.

Figure 4.1: Results of Test 1B-T-L.



(a) Failed beams.



(b) Load-displacement graph.

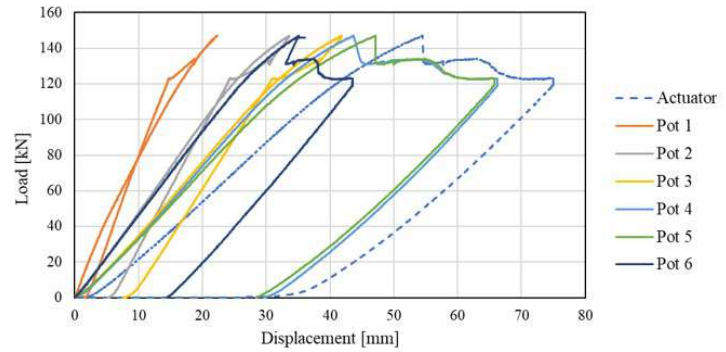
Figure 4.2: Results of Test 2B-T.

finish. Loading continued after the peak, but the actuator was caught on the tongue side of the connection, placing lateral force on the actuator and threatening to damage the frame. Unzipping of the connection towards the supports was observed before the test concluded. The failed connection and load-displacement graph are shown in [Figure 4.3](#).

In Test 3B-M, the load appeared to be evenly distributed to the adjacent beams from the symmetrical string pot data until the groove side connection of the middle beam failed. The failure is similar to Test 2B-G but at a higher peak load of 247 kN and a displacement of 69 mm at Pot 3. Pot 4 broke 6 mm into the test and Pot 7 broke prior to the peak load. The failed connection and load-displacement graph are shown in [Figure 4.4](#). The test was continued and the connection unzipped towards the supports. The tongue of the failed



(a) Failed connection.



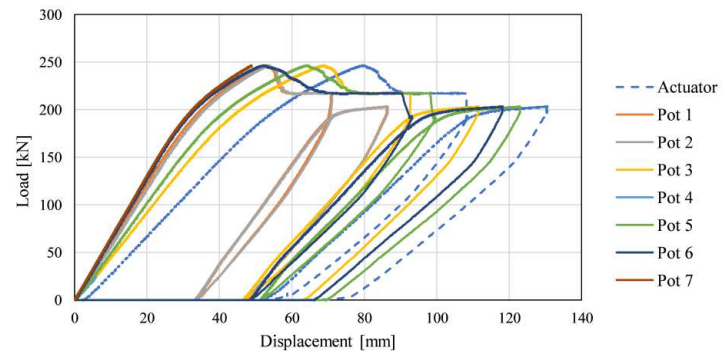
(b) Load-displacement graph.

Figure 4.3: Results of Test 2B-G.

connection cracked above the supports, shown in [Figure 4.5](#). The test was stopped after cracking but reloaded to rupture the middle beam. The reloading was stopped because the middle beam was no longer horizontal and was imposing lateral force on the actuator.



(a) Groove side connection failed.



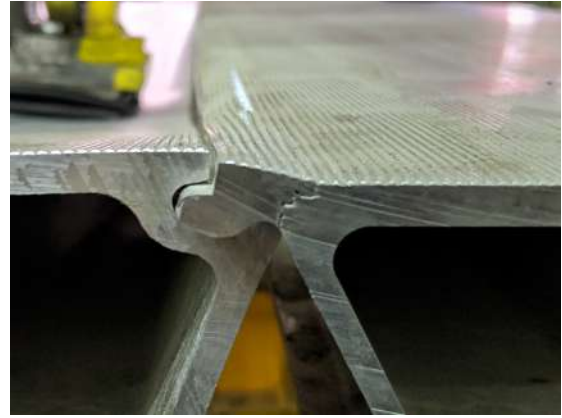
(b) Load-displacement graph.

Figure 4.4: Results of Test 3B-M.

Test 2L1S-M was attempted twice since the support clamps and pin/roller supports could not prevent uplift of the beams. Due to the load on the short beam, the short beam being unconnected to the supports, and the support clamps, the ends of the supports lifted away from the surface it was sitting on as shown in [Figure 4.7a](#). [Figure 4.6](#) shows the short beam bending and the load-displacement graph. The graph contains vertical displacement due to the beams and the supports bending. The situation was remedied by bolting stiff steel beams to the top flange of aluminum beams above the supports as shown



(a) Top view.



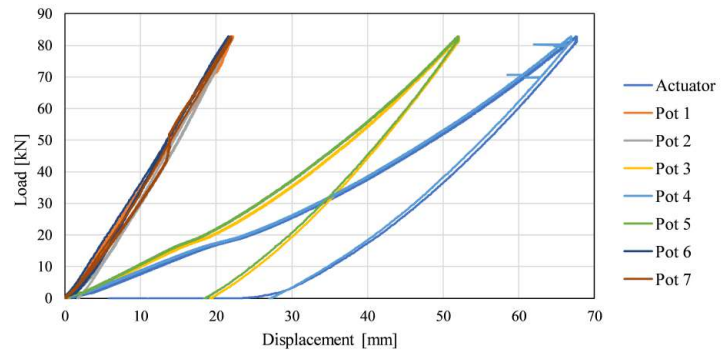
(b) Side view.

Figure 4.5: Cracked tongue in Test 3B-M.

in Figure 4.7b. Due to the bending resistance of the steel and bolts, the supports did not bend on the second attempt. Figure 4.8 shows the groove side connection failing, similar to the previous tests, and the corresponding load-displacement graph. Pot 4 broke before the peak and all of the other pots broke at the peak. The peak load is 122 kN with a displacement of 44 mm at Pot 3.



(a) Supports were bending.



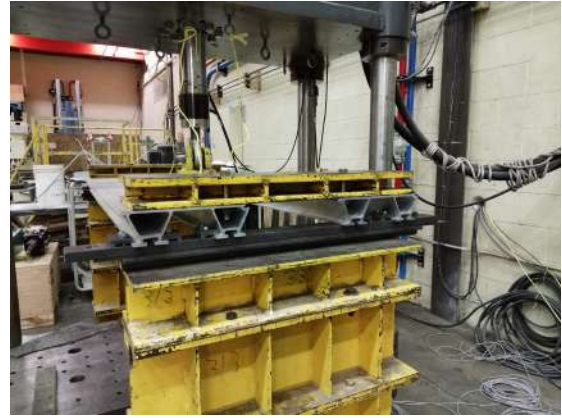
(b) Load-displacement graph.

Figure 4.6: Results of Test 2L1S-M Attempt 1.

Test 1B-T-S yielded due to bending with no signs of buckling, which would indicate longitudinal shear or bearing behaviour. The test stopped and restarted midway due to an inappropriate load limit. The groove side trapezoid lifted from the supports as shown in



(a) Supports lifting up.

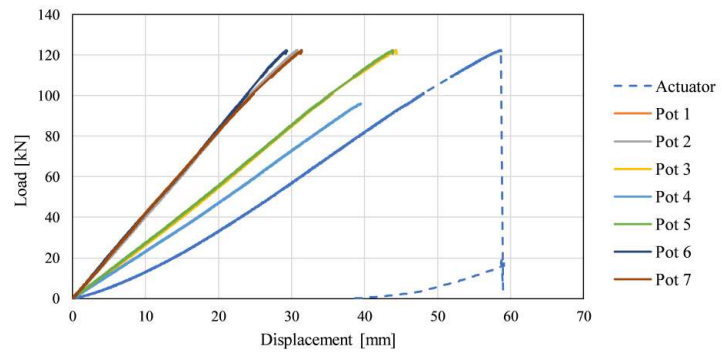


(b) Modification to prevent bending.

Figure 4.7: Problem and solution to supports lifting during Test 2L1S-M.



(a) Groove side connection failed.



(b) Load-displacement graph.

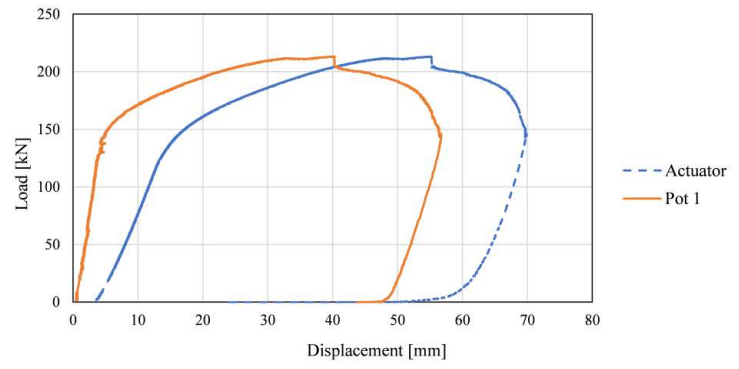
Figure 4.8: Results of Test 2L1S-M Attempt 2.

Figure 4.9a because the support clamps were not used. The edge of the top flange ruptured at a peak load of 212 kN and vertical displacement of 40 mm at Pot 1. The rupture is also shown in Figure 4.9a, and the load-displacement graph is shown in Figure 4.9b.

By the peak load, the metal plate representing the tire load had sheared through the rubber and introduced a concentrated load at an edge. The web under this point buckled and cracked as shown in Figure 4.10.



(a) Top flange ruptured.



(b) Load-displacement graph.

Figure 4.9: Results of Test 1B-T-S.



Figure 4.10: Buckled web under point load.

4.2 Clamp Tests

Test results are found in [Table 4.1](#). Test S-MS-1 was the “proof-of-concept” for the entire test matrix. A slow loading rate of 0.25 mm/min was chosen for the first test to ensure any slip was recorded. This loading rate was inappropriate since a large amount of slip was measured before the clamps engaged and may have caused the experiment to creep, resulting in a lower peak load. Test S-MS-2 used a faster loading rate of 3 mm/min and this was used for the remainder of the tests.

The bolts in Test S-MS-3 were tensioned to 217 Nm (160 lb-ft) instead of 190 Nm (140 lb-ft) to study tensioning the bolts more than specified. From some in-house bolt tensioning tests using turn-of-nut, torque-wrenching, and DTI Squirters [9], the difference between 140 lb-ft and 160 lb-ft is marginal. The extra tensioning did not appear to affect the results.

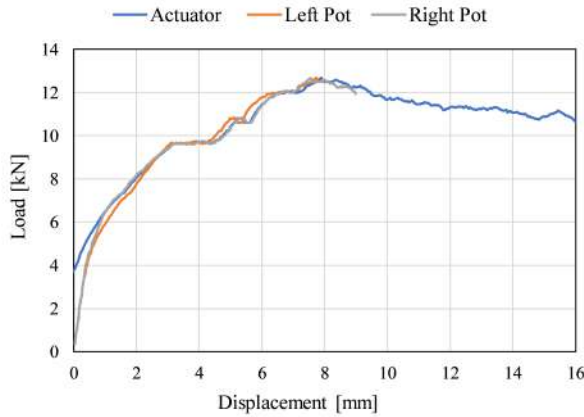
Tests S-SB-1 and S-SB-2 were tensioned properly and their load-displacement graphs are shown in [Figure 4.12](#). The results of Test S-SB-3 were unintended but revealed information regarding torquing the bolts multiple times. The trial was expected to mirror the previous SB tests, but the lock nuts were not installed. The peak load was half of the previous trials at 13.7 kN. The bolts were torqued a second time and the lock nuts were installed. The test was run and exceeded the previous trials at 28.0 kN. The test stopped accidentally due to a displacement limit. The bolts were torqued for the third time, and the test exceeded the previous peak load again at 33.2 kN. The unedited actuator data is graphed in [Figure 4.13](#).

Table 4.1: Clamp test results.

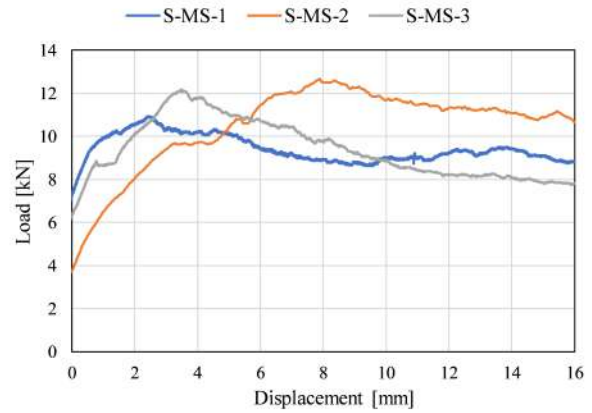
	Mill Scale		Sandblasted
S-MS-1	10.9 kN	S-SB-1	19.2 kN
S-MS-2	12.7 kN	S-SB-2	23.8 kN
S-MS-3	12.2 kN	S-SB-3	Figure 4.13

In general, the rougher texture of the SB plates resulted in higher peak loads than the MS plates. During testing, breaking sand could be heard, and blue and grey dust accumulated on the bottom grip of the frame (see [Figure 4.14](#)). The results of Test S-SB-3 show that torquing the bolts after loading the clamps results in higher peak loads.

Examination of the clamping system after testing consisted of looking at the scratch marks caused by the isolation layers in contact with the steel plate and the deteriorated isolation layers. The marks were not deep and marks in the MS plates were removed by

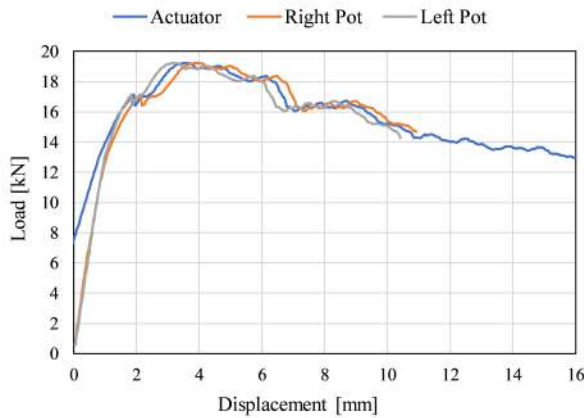


(a) Test S-MS-2

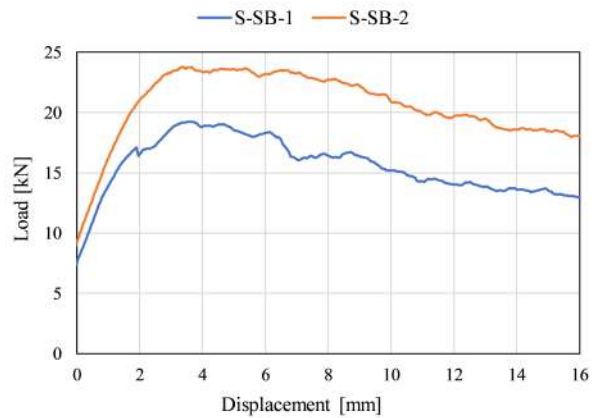


(b) Edited actuator data for MS tests.

Figure 4.11: Results of MS clamp tests.



(a) Test S-SB-1



(b) Edited actuator data for normal SB tests.

Figure 4.12: Results of SB clamp tests.

sandblasting. There was much more scratches on the back side (i.e. against the beam) than on the front side (i.e. against the clamps), since the clamps only held on to a couple of inches on the left and right side of the front, whereas the beam was across the entire back of the plate. The S-SB-3 plate was particularly interesting since the density of scratches increased as the test progressed. Minimal scratches were noted on the edges of the plates, but small gouges and blue stains were sometimes observed.

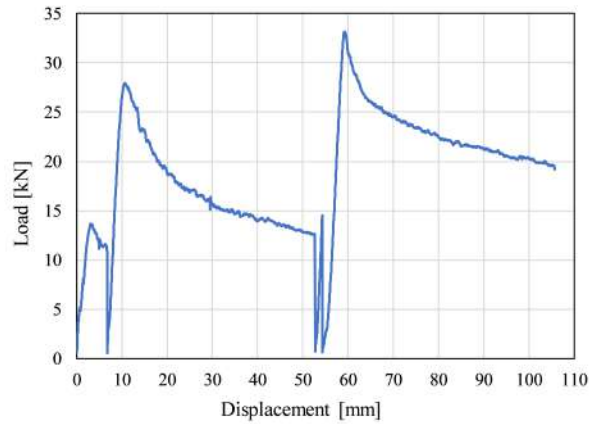


Figure 4.13: Unedited actuator data for Test S-SB-3.



Figure 4.14: Blue and grey dust accumulated under the experiment.

The isolation layer on the clamps and beams contained fine grit that was easily removed. Dark coloured mill scale in particular, was observed on the isolation layers of the MS tests. Material from the SB plates was indistinguishable from the grit from the isolation layer since both are grey. The blue part of the isolation layer was largely undamaged during testing, with the exception of the isolation layer on the clamp that was in contact with the plate edge. The layer sometimes delaminated at this location.



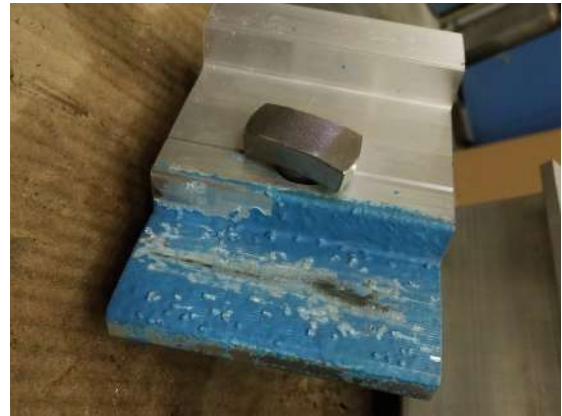
(a) S-MS-2 plate scratched by clamp.



(b) S-SB-2 plate scratched by beam.



(c) MS left on beam from S-MS-2 plate.



(d) Delaminated isolation layer from Test S-SB-1.

Figure 4.15: Results of visual inspection preceding the clamp tests.

Chapter 5

Analysis of Results

This section contains analyses of the experimental results and theoretical methods for determining the strength of the tested systems. The theoretical methods consist of mechanics-based calculations and FE models for beam and clamp test results.

5.1 Beam Tests

5.1.1 Comparison of Beam Test Results

Tests 1B-T-S (650 mm span) and 1B-T-L (2 m span) were the first tests completed and the “proof-of-concept” for the entire test procedure. Both tests did not use support clamps, which resulted in uplift from the supports. This was remedied in the following tests since all of the tests were loaded somewhat unevenly and asymmetrically. Test 1B-T-S in particular was not well instrumented since the predicted failure mode was incorrect. All of the test results are compared in [Figure 5.1](#). Only the string pot with the greatest displacement is shown. The two parts of Test 2L1S-M were added together for overall deflection. Some comparisons are noted in the following list:

- Tests 1B-T-L and 1B-T-S both used one beam but had different failure mechanisms. Test 1B-T-L failed due to bending and Test 1B-T-S appeared to be a shear failure (discussed in [Section 5.1.3](#)).
- Tests 1B-T-L and 2B-T demonstrate that two beams increase the initial stiffness drastically and double the peak load, but ductility is slightly reduced. The initial

elastic stiffnesses of Tests 1B-T-L, 2B-T, 2B-G, and 3B-M are compared to a linear-elastic beam calculation with CSA S157 properties [6] in Table 5.1.

- Test 2B-G followed the same curve as Test 2B-T until the connection failed. The test showed minimal ductility prior to connection failure.
- The Test 3B-M results and the Test 2L1S-M results differ since the short beam tended to bend in the perpendicular direction from the other beam tests, but both tests failed at similar vertical displacements.
- Test 3B-M had less of a stiffness increase from Test 2B-T in comparison to the change in stiffness from Test 1B-T-L to Test 2B-T. Test 3B-M appears to be a scaled version of Test 2B-G.

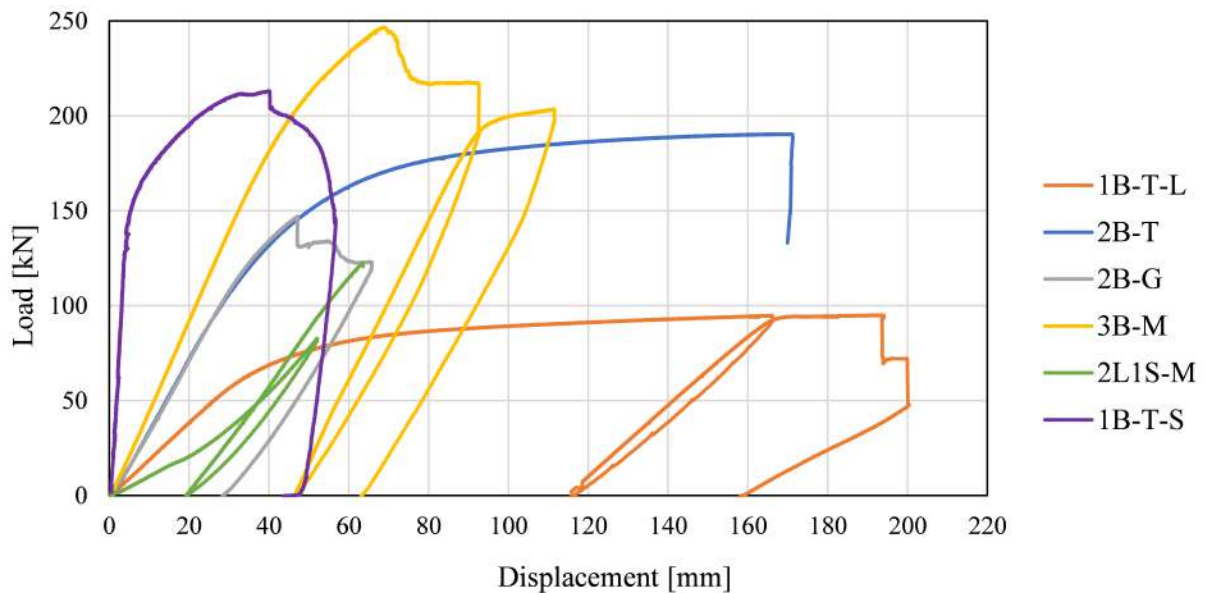


Figure 5.1: Comparison of all beam tests from Section 4.1.

Table 5.1 presents the elastic stiffness of the 2 m span tests in comparison to the elastic stiffness of a single beam calculated with $E = 70$ GPa assumed [6]. Test 1B-T-L is less stiff than the CSA S157 beam because the load is concentrated on one side of the beam. Interestingly, the Test/Predicted Ratio for Test 1B-T-L is greater than 0.5, indicating the unloaded trapezoid carries some load.

Table 5.1: Initial elastic stiffness.

Test	P/Δ	Stiffness (EI)	$\frac{\text{Test}}{\text{Single Panel}}$	Ratio
Simply-supported beam calculation (single panel)	2594 kN/m	432 kNm ²	-	-
1B-T-L	1860 kN/m	310 kNm ²	0.7	0.7
2B-T & 2B-G	3540 kN/m	590 kNm ²	1.4	1.4
3B-M	4560 kN/m	760 kNm ²	1.8	1.8

5.1.2 Aluminum Properties

Section 5.1.3 requires material properties for theoretically calculating the capacity or resistance of the beam tests. The material properties are determined from CSA S157 [6] and the mill certificates provided by MAADI Group Inc. The mill certificates state the yield stress, ultimate stress, and ultimate elongation for the aluminum used in the construction of three pedestrian bridges as well as the test specimens. Therefore, it is uncertain which mill certificate corresponds to the beams in the laboratory, and an average was used. There are nine mill certificates for the beam test specimens, as shown in Figure 5.2. The first mill test is significantly stronger than the others, and was omitted from the stress and strain averages.

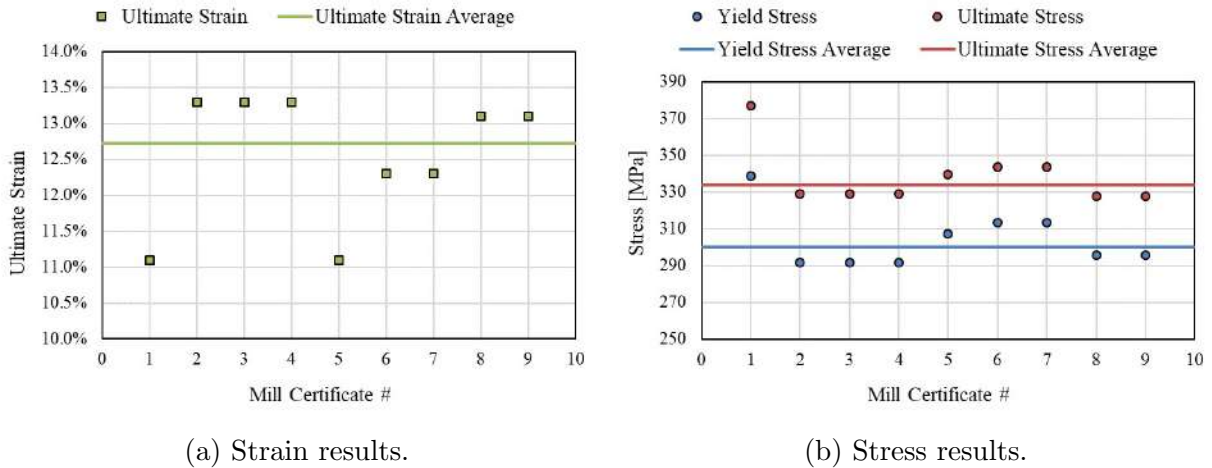


Figure 5.2: Ultimate strain, ultimate stress, and yield stress for the beam test specimens.

Two sets of aluminum properties are presented in Table 5.2. The first column shows the properties from CSA S157 [6] for design purposes and the second column shows the

theoretical properties used for a more accurate representation of material strength based on the mill certificates. Yield and ultimate strain are not shown for CSA S157, because this standard does not prescribe values for these parameters. Details regarding strain at the yield stress are not provided in the mill certificates and this parameter was calculated from the elastic modulus and yield stress. Figure 5.3 shows a stress-strain curve created from the second column of Table 5.2, and is highly simplified. The mill certificates do not report stress and strain at fracture so no softening is considered in the simplified stress-strain curve. The properties and curve can only be used to find peak load not the fracture load or displacement.

Table 5.2: Aluminum properties for theoretical analysis.

Property	CSA S157 [6]	Mill Certificates (MC)
Elastic Modulus	70,000 MPa	70,000 MPa
Poisson's Ratio	0.33	0.33
Yield Stress	240 MPa	266.2 MPa
Yield Strain	-	0.004
Ultimate Stress	260 MPa	296.1 MPa
Ultimate Strain	-	0.127

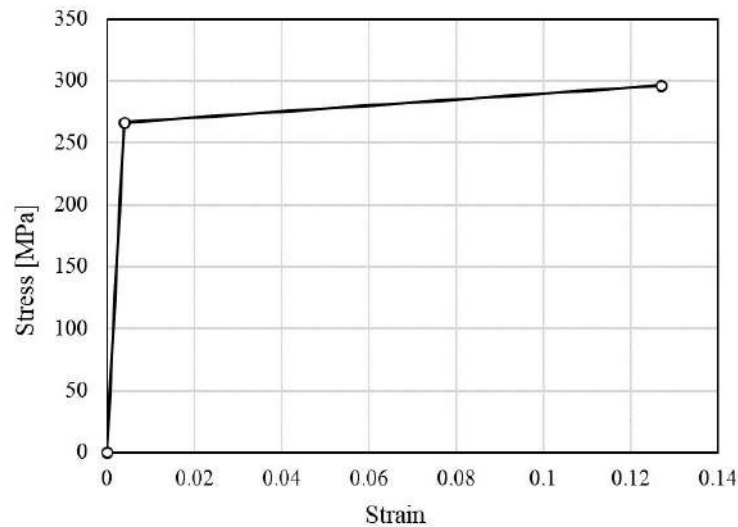


Figure 5.3: Stress-strain curve used for theoretical analysis.

5.1.3 Theoretical Analysis Results

This section compares the experimental results (Section 4.1) to CSA S157 beam calculations [6] and FE analysis. The CSA S157 beam calculations are based on typical beam theory and consist of calculations for bending or moment, longitudinal shear, and bearing. A brief description of the three types of resistance calculations is provided in this chapter, sample calculations and results are in Appendix B, and the governing load is recorded in Table 5.4.

Since GuarDeck® does not contain welds or drilled holes, bending resistance calculations are relatively straightforward. The cross-section is considered a Class 2 section according to CSA S157, meaning it is “capable of carrying moment up to the onset of yielding in compression without local buckling”. This means that straight-forward linear-elastic moment resistance calculations are applicable. Equation 5.1 is for the compression fibres and Equation 5.2 is for the tension fibres. ϕ_y and ϕ_u are equal to 0.9 and 0.75 for design but are taken as unity (i.e. 1.0) for comparison to experimental results.

$$M_r = \phi_y M_y = \phi_y S F_y \quad (5.1)$$

Where M_r is the bending or moment resistance in Nmm, ϕ_y is the resistance factor on the yield strength, M_y is the moment at first yield in Nmm, S is the elastic section modulus in mm³, and F_y is the yield strength in MPa.

$$M_r = \phi_u S_n F_u \quad (5.2)$$

Where M_r is the bending or moment resistance in Nmm, ϕ_u is the ultimate strength factor, S_n is the net elastic modulus to account for drilled holes in mm³, and F_u is the ultimate strength in MPa.

GuarDeck® has no web stiffeners and the longitudinal shear resistance is dependent on the vertical parts of the trapezoids (the webs). The shear resistance of aluminum is taken as $0.6F_y$. Subsequently, calculations are done to determine whether the strength of the webs is further decreased due to local buckling. GuarDeck® is not subject to local buckling and was likely designed this way to simplify calculations. The shear resistance calculation is shown in Equation 5.3.

$$V_r = \phi_y h w F_{sc} \quad (5.3)$$

Where V_r is the shear resistance in N, ϕ_y is the resistance factor on the yield strength, h is the web depth in mm, w is the web thickness in mm, and F_{sc} is the initial buckling stress in MPa.

Bearing resistance refers to web crippling in CSA S157 where the webs above the support may buckle or crush. The first part of the [Equation 5.4](#) represents the buckling resistance and the second part of [Equation 5.4](#) determines the crushing resistance.

$$C_r = \phi_y k(n + h)wF'_c \leq \phi_y n w F_y \quad (5.4)$$

Where C_r is the bearing or compression resistance in N, ϕ_y is the resistance factor on the yield strength, k is a constant equal to [Equation 5.5](#), n is bearing length in mm, h is the web depth in mm, w is the web thickness in mm, F'_c is modified compressive strength calculated using [Equation 5.6](#) in MPa, and F_y is the yield strength in MPa.

$$k = 0.5 \left[1 + \frac{e}{\frac{n}{2 + h}} \right] \leq 1 \quad (5.5)$$

Where k is a constant, e is the distance from the centre of bearing to the end of the beam in mm, n is bearing length in mm, and h is the web depth in mm.

$$F'_c = \frac{\pi^2 E w^2}{4h^2} \left[1 - \left(\frac{f_{bf}}{F_{bc}} \right)^2 \right] \quad (5.6)$$

Where F'_c is modified compressive strength in MPa, E is the the elastic modulus in MPa, w is the web thickness in mm, h is the web depth in mm, f_{bf} is the factored longitudinal compressive stress due to overall bending moment in MPa, and F_{bc} is the web buckling stress for bending in MPa.

With the exception of Test 2L1S-M, the beam calculations were completed as if the experimental testing was not performed and all tests are treated as slender beams. Bending failure (i.e. tension flange rupture) was expected to govern all the beam tests except for Test 2L1S-M. Test 2L1S-M was expected to fail at the tongue and groove connection so no beam calculations were performed. The beam calculation results for Tests 1B-T-L and 1B-T-S are in [Table 5.3](#). These values are calculated using the CSA S157 properties and mill certificate (MC) properties from [Table 5.2](#). The governing load and corresponding

Table 5.3: Simply-supported beam calculations for Tests 1B-T-L and 1B-T-S.

Failure Mode	Test 1B-T-L		Test 1B-T-S	
	CSA S157	MC	CSA S157	MC
Bending	46 kN	69 kN	140 kN	213 kN
Longitudinal Shear	343 kN	421 kN	343 kN	421 kN
Bearing	583 kN	719 kN	292 kN	360 kN

vertical displacement for all tests are reported in [Table 5.4](#) and [Table 5.5](#), respectively. The corresponding vertical displacement is calculated using linear-elastic calculations.

There is discrepancy between the beam calculations and the beam tests since the calculation assumes the load covers the entire middle cross-section unlike the tire load in the beam tests. The calculations are done to provide insight into how strong the beams are in comparison to typical design calculations.

In terms of the FE analysis, two FE models were made for each beam test. The first model is composed of 2D plate elements, which form a 3D representation of the beam. This method of modelling is recommended by Siwowski [29] as discussed in [Section 2.4.1](#) because extruded bridge decks are generally composed of thin plates and resist force primarily through plate-bending mechanisms. This model is referred to as the shell model.

The second FE model is composed of 3D elements that form a more accurate representation of the beam cross-section. The ridges on the top and bottom flanges are omitted. This model is referred to as the brick model. First-order elements are used even though they are not recommended by Siwowski [29], because the elements have difficulty modelling pure bending. He stated that higher-order elements can overcome this problem but computation time is a problem. The models in this research are relatively large and intricate, therefore, a large number of elements are required for each analysis. Higher-order elements were tested briefly but the computation time was excessive.

The shell and brick models for Test 1B-T-S are shown in [Figure 5.4](#) to illustrate the difference between the two types of models. Although the brick models are not recommended for this type of analysis, the information the model provides regarding the tongue and groove connections made their use necessary. The tongue and groove connections are an essential part of the deck system and are not represented in the shell models. In the shell models, the edges of beams in contact are tied together to create a perfect and symmetrical joint. The shell models for Tests 2B-T and 2B-G are identical since it does not matter which side of the connection the load is on. It was known from the beginning that no buckling of any kind would occur and no provisions in the FE model are made to account

for potential buckling.

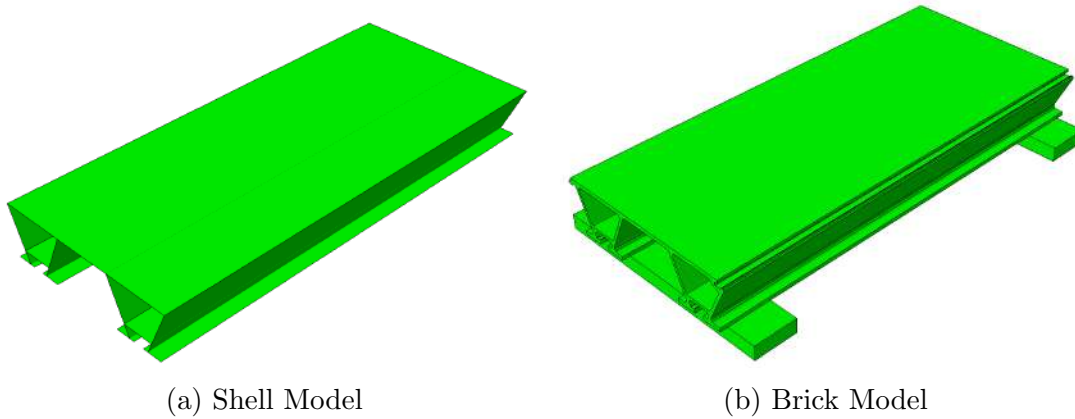


Figure 5.4: Two types of FE models.

Tests 1B-T-L and 1B-T-S did not use support clamps and without them, the beam can lift away from the supports but not move through the supports. Typical boundary conditions can not represent this as they prevent displacement in both directions. To model the support conditions in the brick model, steel supports and friction are added. Typical pin and roller boundary conditions are applied directly to the beams for all the other models. Other than Tests 1B-T-L and 1B-T-S, contact is frictionless to improve computation time. In addition, linear springs with almost no stiffness are used to prevent rigid body motion and maintain contact between unattached parts.

The load is applied as a pressure directly to the beam in an area equivalent to the tire load. The material properties displayed in [Figure 5.3](#) are input as shown. The software incrementally adds load to both models and decreases the increment if needed to achieve a converged solution. The load increases until the increment is smaller than the minimum specified (many times smaller than a newton) or a converged solution is not calculated within several attempts. The beam geometry is highly distorted close to the peak load and the residuals are not within tolerance causing convergence problems. Deformation beyond the failure of the tongue and groove is beyond the capabilities of the static models used. The stress and strain beyond the peak are not included in the stress-strain curve and therefore softening and rupture of the beams are not modelled.

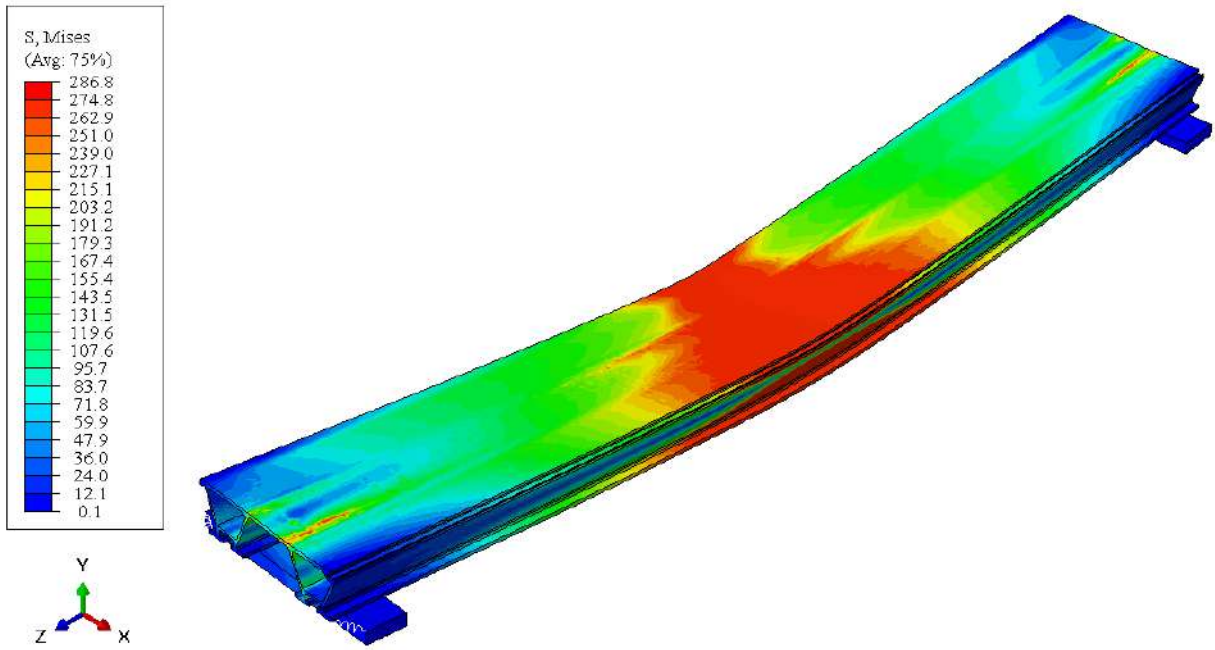
The results of the shell and brick models are located in [Table 5.4](#) and [Table 5.5](#) where the first table contains the peak loads and the second table contains the corresponding displacements. [Figure 5.5](#) to [Figure 5.10](#) shows the brick models and the graphical results presented in the tables.

Table 5.4: Peak load reported for each analysis method.

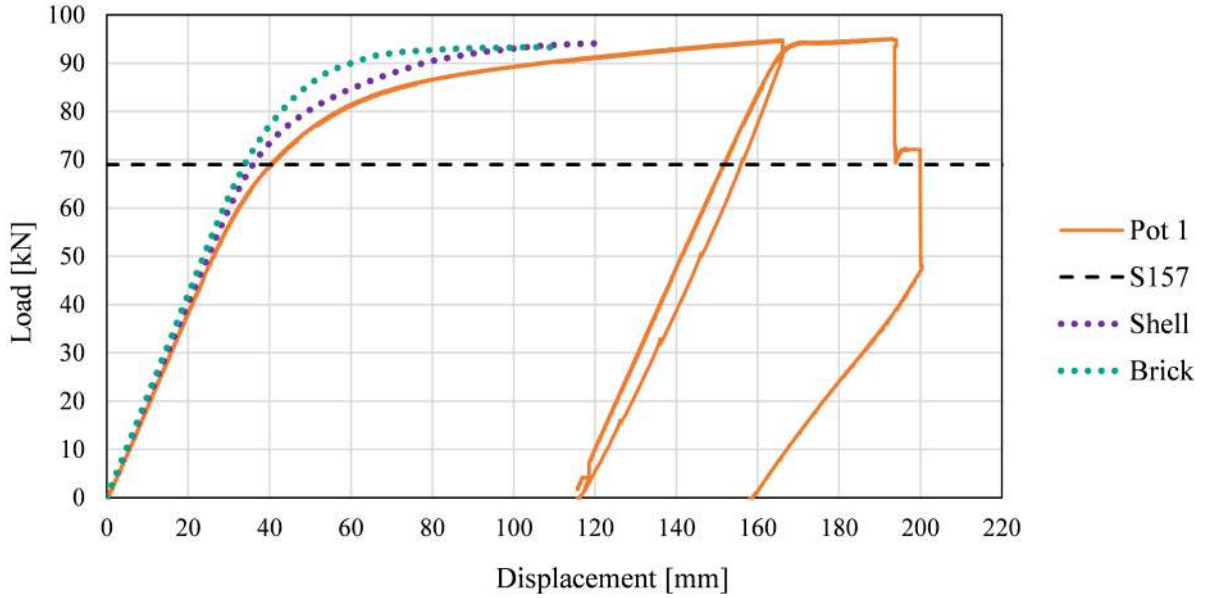
Test	Experimental (Section 4.1)	Beam Calculation	Shell Model	Brick Model
1B-T-L	95 kN	69 kN	94 kN	93 kN
2B-T	190 kN	138 kN	186 kN	189 kN
2B-G	147 kN	138 kN	186 kN	151 kN
3B-M	247 kN	208 kN	282 kN	228 kN
2L1S-M	122 kN	-	206 kN	72 kN
1B-T-S	212 kN	213 kN	197 kN	247 kN

Table 5.5: Corresponding vertical displacement reported for each analysis method.

Test	Experimental (Section 4.1)	Beam Calculation	Shell Model	Brick Model
1B-T-L	197 mm	27 mm	122 mm	110 mm
2B-T	171 mm	27 mm	91 mm	128 mm
2B-G	47 mm	27 mm	91 mm	41 mm
3B-M	69 mm	27 mm	109 mm	47 mm
2L1S-M	44 mm	-	133 mm	37 mm
1B-T-S	55 mm	3 mm	39 mm	46 mm

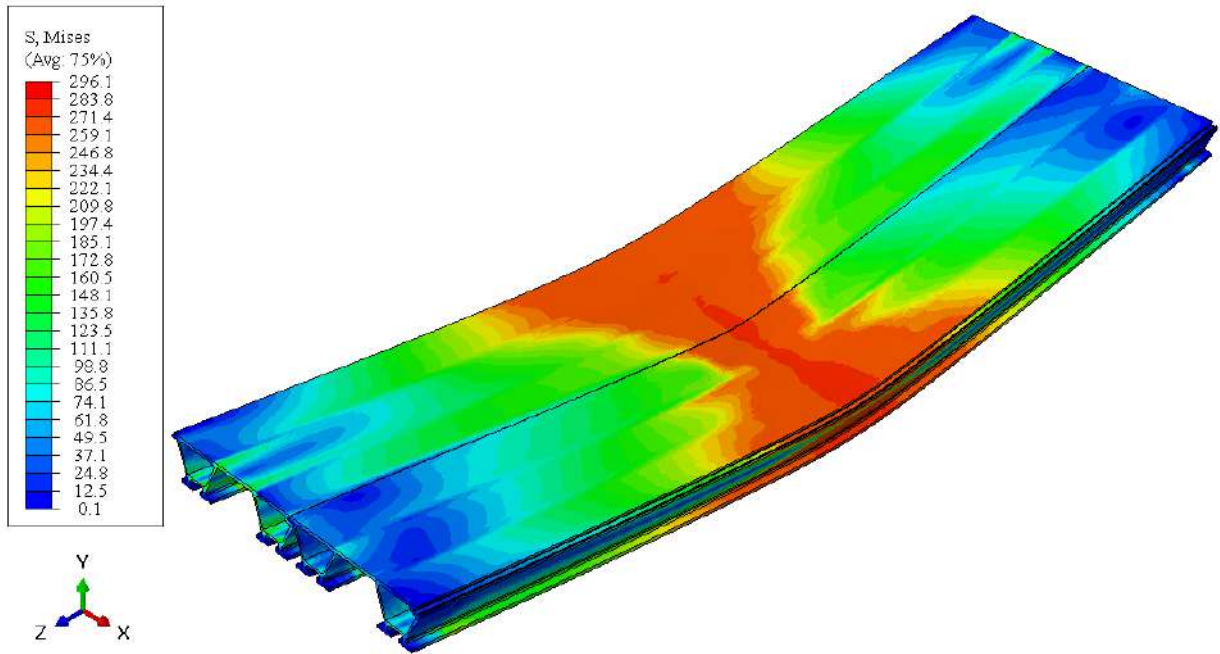


(a) FE model showing Von Mises stress with units of MPa.

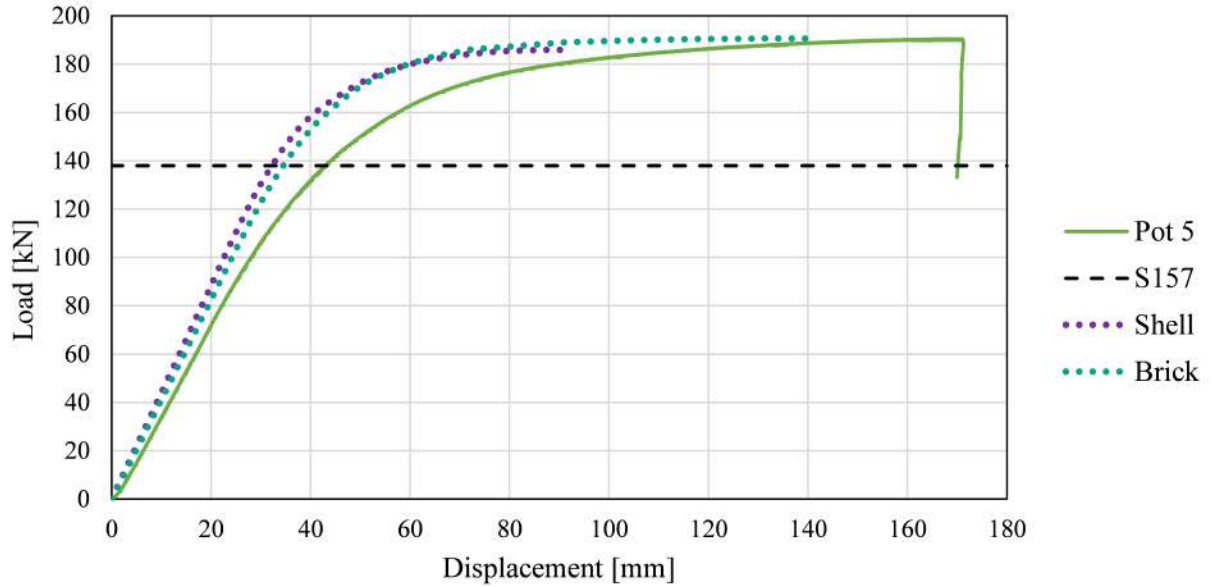


(b) Load-displacement graph.

Figure 5.5: Results of Test 1B-T-L theoretical analyses.

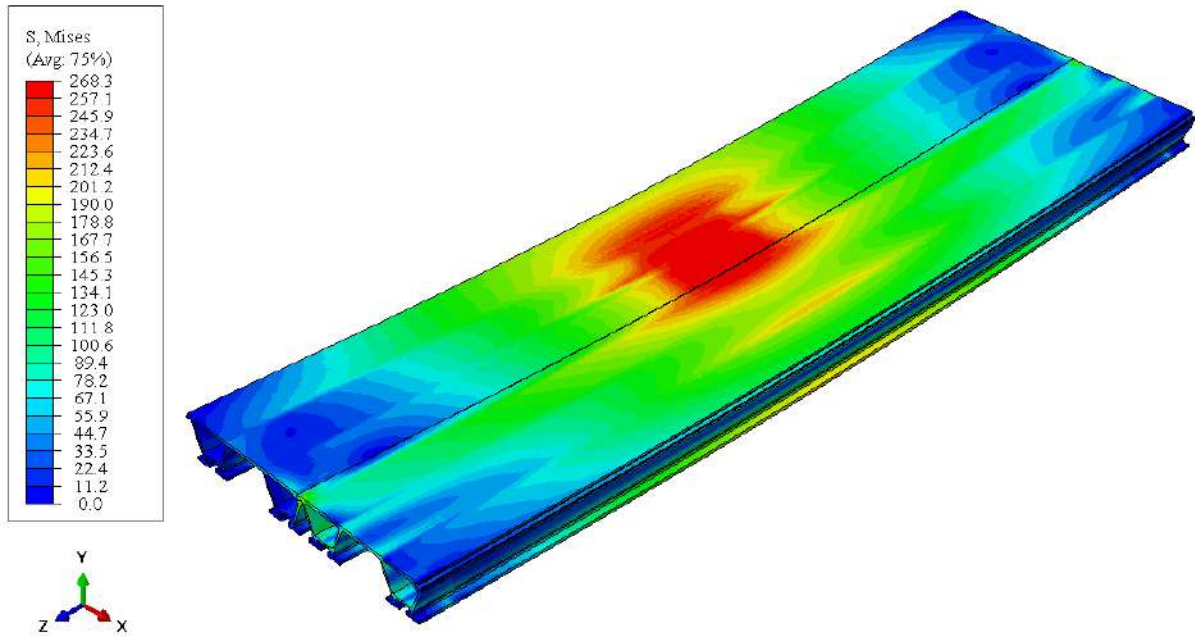


(a) FE model showing Von Mises stress with units of MPa.

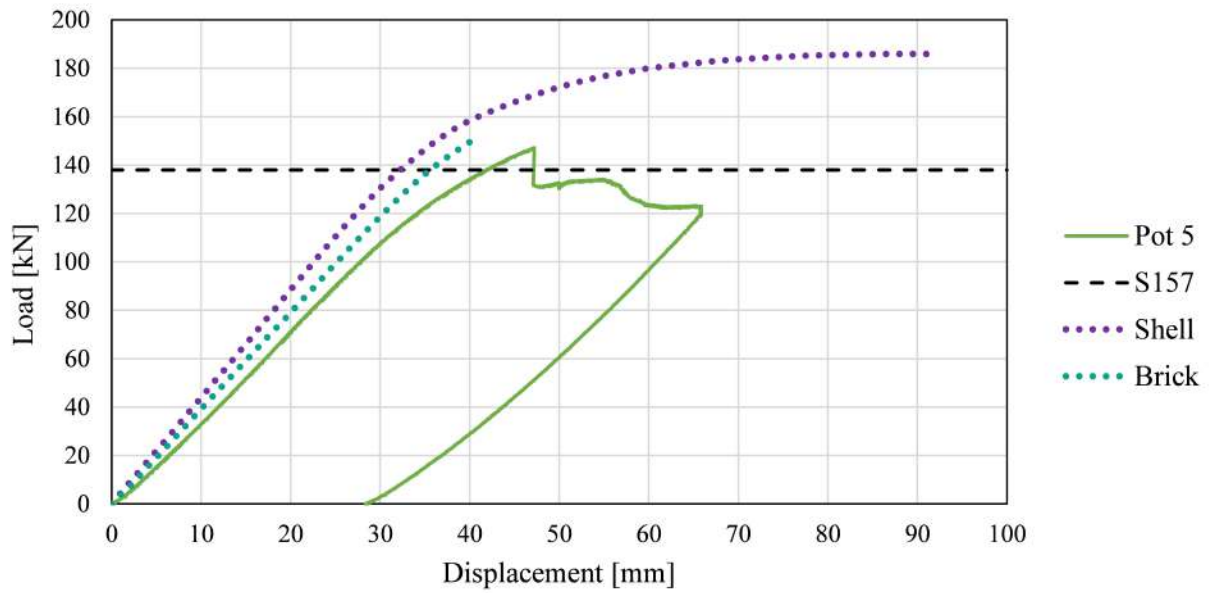


(b) Load-displacement graph.

Figure 5.6: Results of Test 2B-T theoretical analyses.

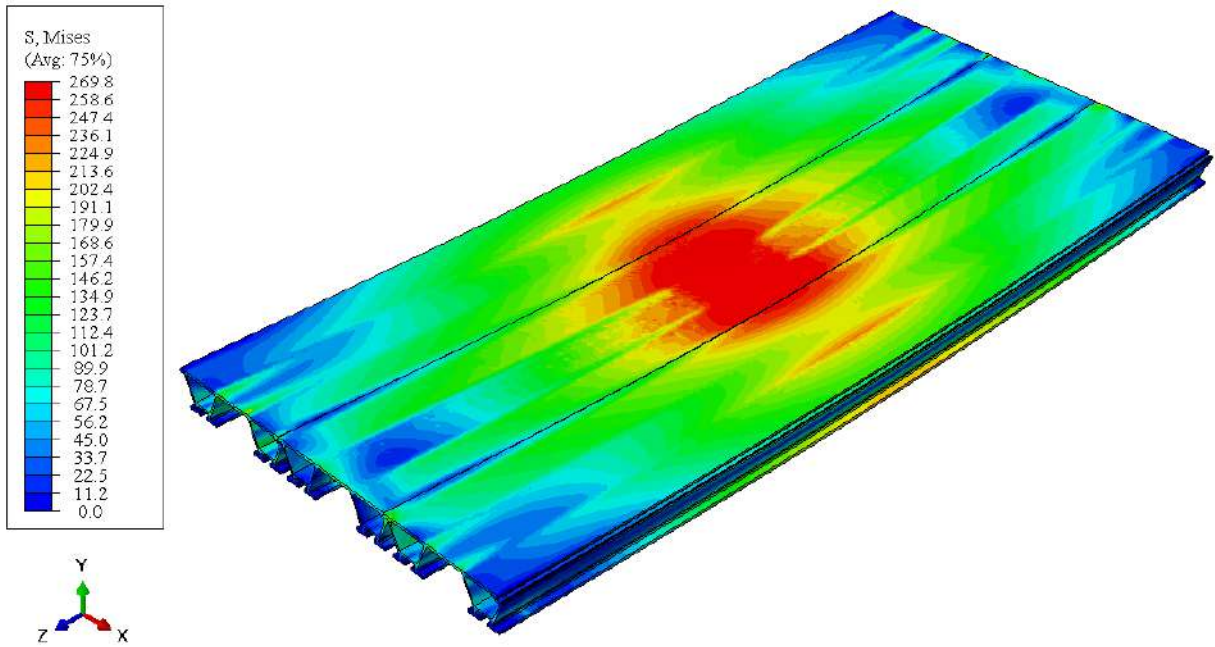


(a) FE model showing Von Mises stress with units of MPa.

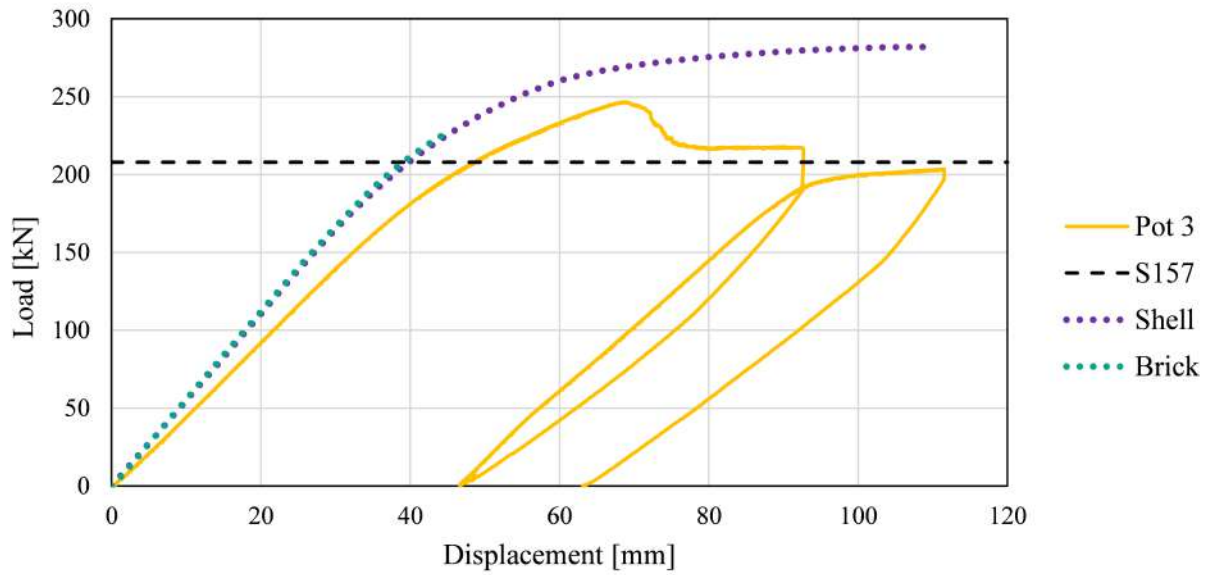


(b) Load-displacement graph.

Figure 5.7: Results of Test 2B-G theoretical analyses.

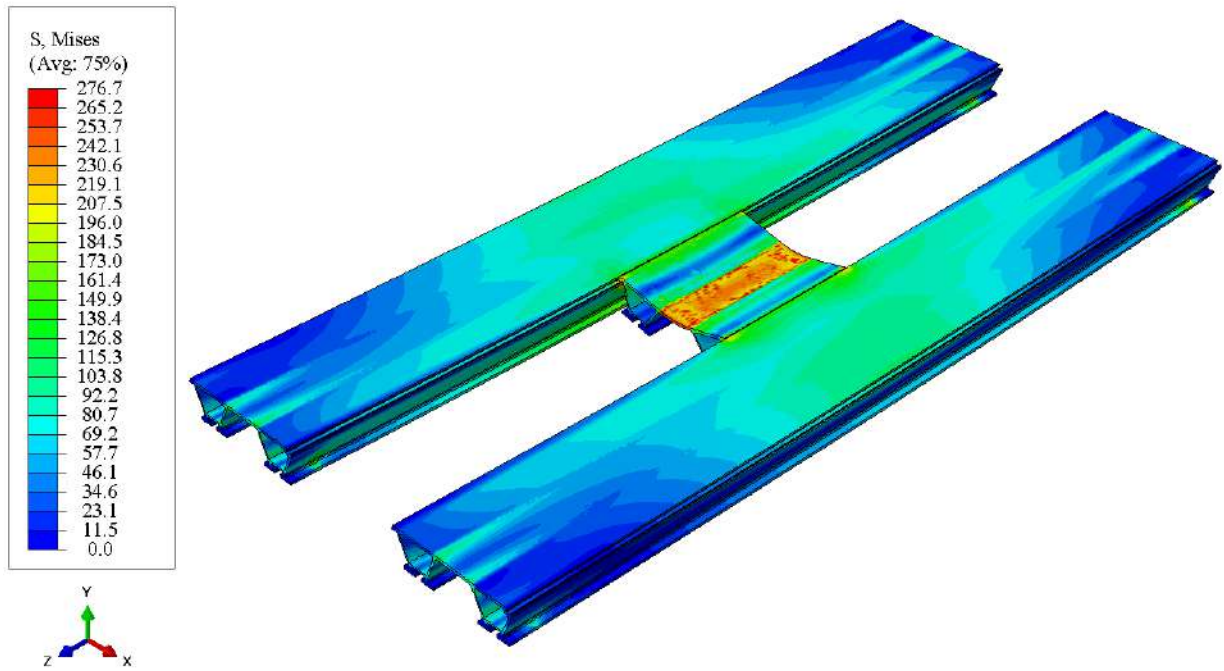


(a) FE model showing Von Mises stress with units of MPa.

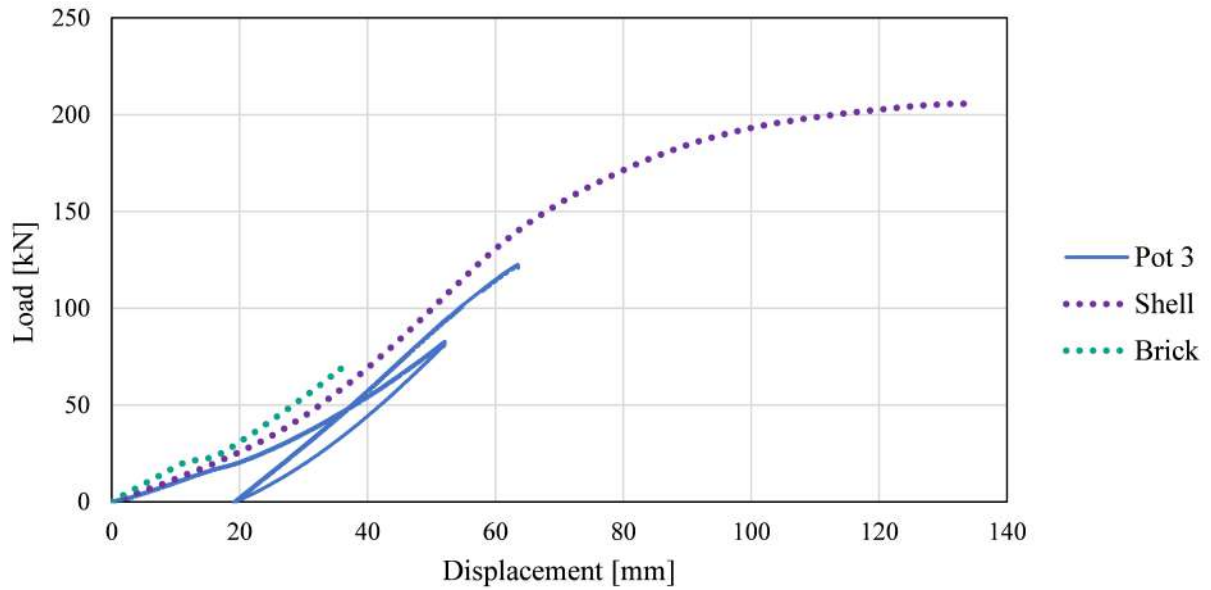


(b) Load-displacement graph.

Figure 5.8: Results of Test 3B-M theoretical analyses.

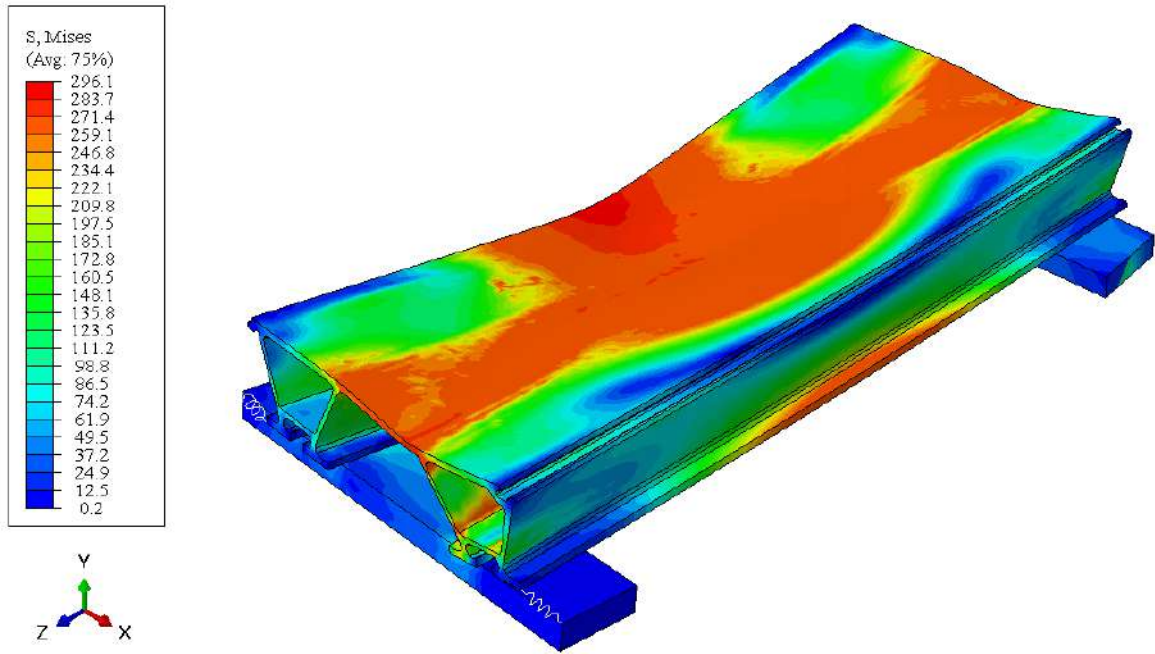


(a) FE model showing Von Mises stress with units of MPa.

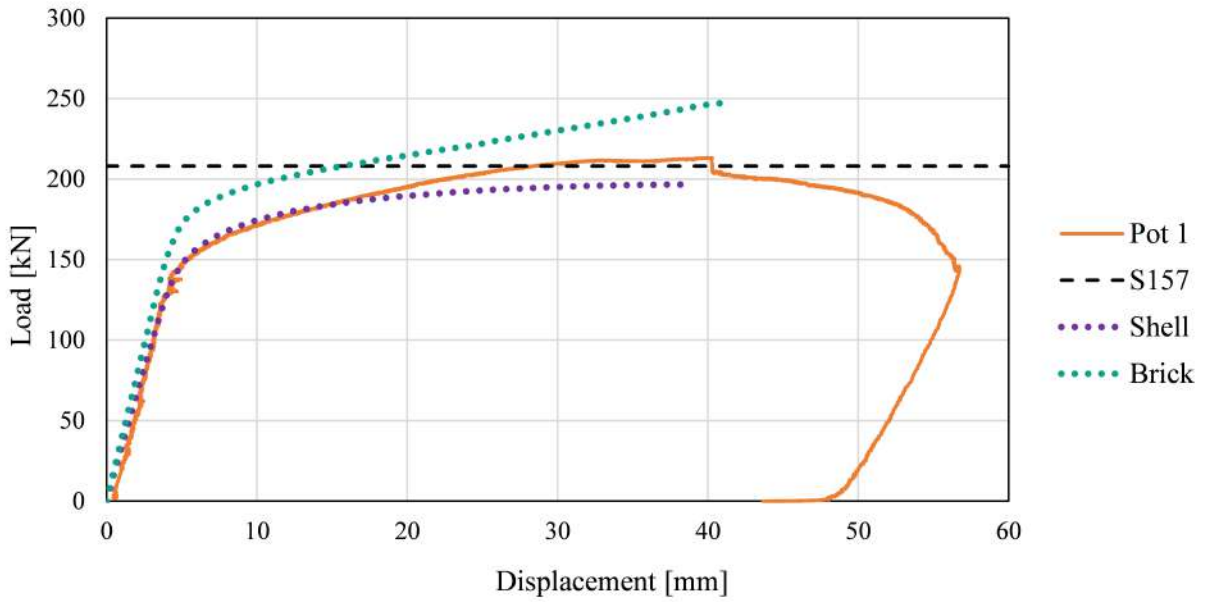


(b) Load-displacement graph.

Figure 5.9: Results of Test 2L1S-M theoretical analyses.



(a) FE model showing Von Mises stress with units of MPa.



(b) Load-displacement graph.

Figure 5.10: Results of Test 1B-T-S theoretical analyses.

5.1.4 Discussion of Theoretical Results

In general, the CSA S157 beam calculations conservatively underpredict the ultimate load of the beam tests except for Test 1B-T-S. From the graphs, the beam calculations estimate the load at the transition between the elastic and plastic regions. This is because the calculation is based on linear-elastic strain and plastic behaviour. The calculations are conservative since there is still ductility and strength available. The bending calculations for Tests 2B-G and 3B-M are adequate only because the tongue and groove connection can carry load until the plastic region. Surprisingly, Test 1B-T-S is well predicted by the beam calculations even though the beam did not purely fail by bending. Test 1B-T-S span is discussed further at the end of this section. The linear-elastic deflection calculations does not reflect the actual deflections. The calculations can be improved by including the plastic portion of the stress-strain curve and calculating the plastic strain at the peak bending moment, but this is significantly more complicated and easier to do in FE software.

The shell models are generally sufficient at predicting the peak load of the beam tests that failed due to bending, such as Tests 1B-T-L and 2B-T. The FE analysis predicted much higher loads for Tests 2B-G, 3B-M, and 2L1S-M, where the tongue and groove connection failed before rupture of the tension flange. The shell analysis demonstrates the behaviour of the connection if were to not fail, but the predicted strength is much greater than the actual strength. Test 1B-T-S is under-predicted by the analysis but follows the experimental load-displacement better than any other analysis. The under-prediction may be a result of the simplified stress-strain curve. Except for Test 1B-T-S, the shell models has higher initial linear-elastic stiffness than the experiments. This may be because of the assumption made when developing the stress-strain curve. An elastic modulus of 70 GPa is used because this is the value provided by CSA S157 [6] for aluminum structures and the mill certificates do not provide a value. Other sources (e.g. ASTM [14]) report the elastic modulus at approximately 69 GPa.

The brick models are closer to predicting the experimental peak loads of the tests that had tongue and groove connection failure. The analysis of Test 2B-G stops at the same time as the failure in the experiment. Test 3B-M being less accurate may be a result of modelling difficulty due to the presence of many contact planes. Test 2L1S-M similarly has the problem of many contacts planes and is particularly difficult to model since the short section is supported by contact planes only. The discrepancy between the brick model and the other curves in Figure 5.9 is evidence of this. A comparison of brick models at peak load is shown in Figure 5.11 where Test 2B-T is yielding and the groove side connections of Tests 2B-G and 3B-M are failing. A closer look at the tongue and groove connections is provided in Figure 5.12. The figure shows Test 3B-M where the tongue side is well connected and

the groove side is slipping. Lastly, [Figure 5.13](#) shows the difference between the shell and brick models for Test 3B-M. The shell model continue past the connection failure resulting in yielding of the middle cross-section as opposed to the brick model, where the groove side is slipping. Note that the displacement of the FE models is unscaled.

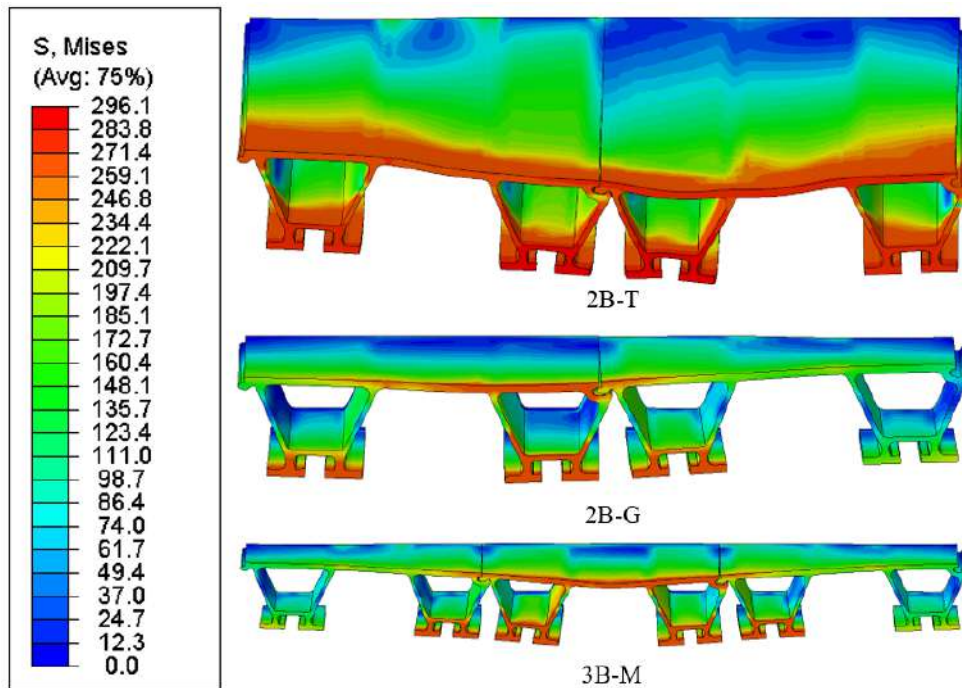


Figure 5.11: Middle cross-section of brick models for Tests 2B-T, 2B-G, and 3B-M at the peak load. Von Mises stress with units of MPa is shown.

The peak load of Test 1B-T-S is adequately predicted by the bending calculations but it did not fail due to the rupture of the tension flange. It is possible that the tension flange was near rupture but shear across the top flange reached the peak shear stress first. The peak shear stress for structural aluminum is $0.6\phi_y F_y$ according to CSA S157 [6]. The resistance factor is taken as unity for direct comparison and therefore, $0.6F_y$ or 159.7 MPa is the peak shear resistance of the material. Unlike yielding, the peak shear stress is associated with immediate rupture of the material not ductility. From [Figure 5.10](#), the top flange above the supports and the bottom flange of the middle cross-section are high stress regions. Shear stress across the beam's cross-section above the supports is shown in [Figure 5.14](#) where a change in direction of shear stress is visible at the rupture location. The stress in [Figure 5.14b](#) is approximately 155 MPa, which is close to the peak shear stress from CSA

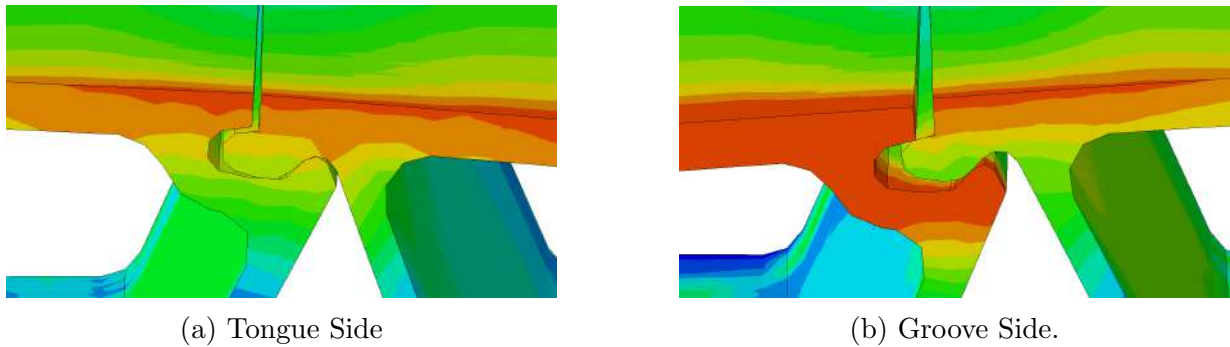


Figure 5.12: Close-up of tongue and groove connection for Test 3B-M at peak load. Von Mises stress with units of MPa is shown.

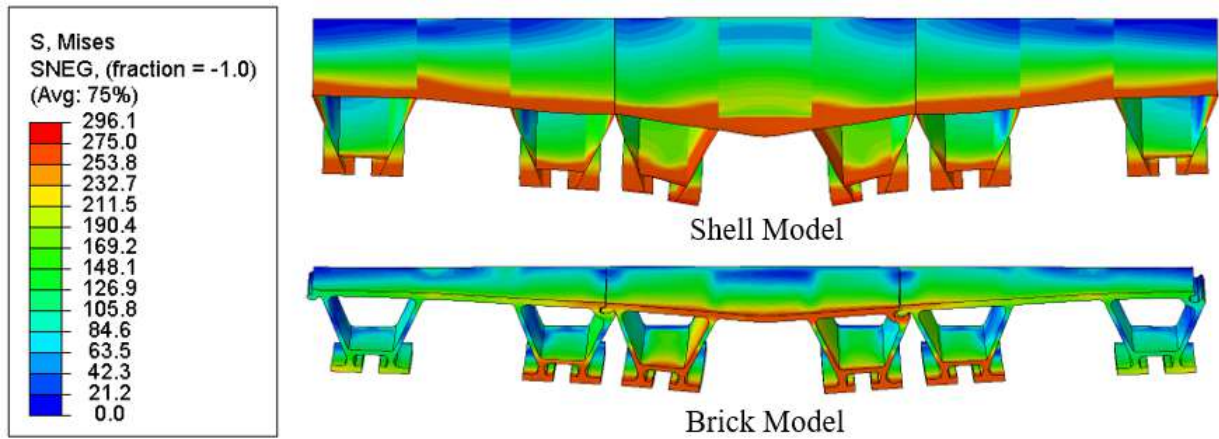
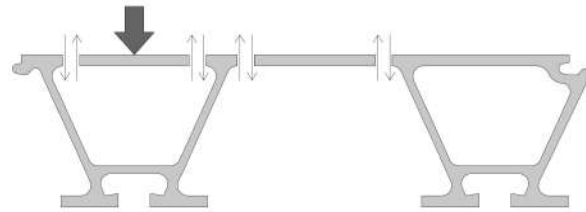


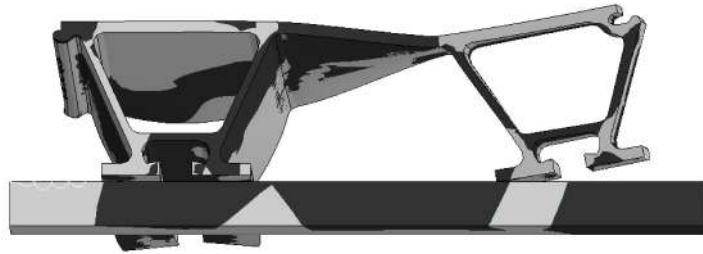
Figure 5.13: Middle cross-section of shell and brick models for Test 3B-M at the peak load. Von Mises stress with units of MPa is shown.

S157. In addition to stress across the cross-section, there is shear stress due to bending which may have contributed to the rupture.

In summary of this discussion, each theoretical analysis method is useful for the validation of the bridge deck design. The beam calculations are conservative for nearly all tests despite some tests having different failure modes from those calculated. The shell models are sufficient for beams that fail due to bending, but can not model intricate connections. Finally, the brick models are able to model some of the behaviour of the tongue and groove connections. The brick models are the most difficult to implement but the results are reflective of the more complicated failure mechanism. Without knowing the failure mechanism



(a) 2D shear force diagram.



(b) Side view of FE beam showing X-Y shear stress. Gray and black represent positive and negative shear stress, respectively.



(c) Side view of the failed experiment beam.

Figure 5.14: Comparison of shear force and deformed shape.

before modelling, interpretation of the brick model results can be difficult since the analysis simply stops when the model fails to converge. There is value in having all three analyses since they can validate each other. In particular, the brick models require validation since the model could fail to converge but the cause may not be obvious. If the behaviour is similar to the predictions made by calculations and the shell models prior to stopping, it indicates that another failure mechanism may be involved such as the tongue and groove failure in this case.

5.2 Clamp Tests

The experimental results of the static clamp tests demonstrate the well-known phenomenon that rougher surfaces result in higher friction forces than smoother surfaces. The MS specimens had lower peak loads and less variability than the SB specimens. The MS surface finish is a result of producing steel, which likely has less variability than the SB specimens, which were sandblasted individually by a machine shop.

The last SB specimen (i.e. S-SB-3) is unlike the other SB tests because it was torqued multiple times. The peak load increased with every time the bolts were torqued. When inspecting unused clamps, it is obvious that the sand is not evenly distributed across the surface. The higher peak loads may be caused by the first use of the clamps wearing down the grit touching the steel and loosening the bolt. When the bolts are re-torqued, more of the isolation layer is in contact since the taller grains are worn down and the pressure is more evenly distributed across the surface. This results in slower wearing of the isolation layer and bolt loosening, therefore, higher peak loads are achieved.

GuarDeck® DG connections resist load in the direction parallel to the girders through friction. The Coulomb model of friction for calculating friction force is shown in [Equation 5.7](#). CSA S6 states that aluminum and steel have a friction coefficient of 0.3 in slip-critical connections, which also rely on friction. This value was used for all calculations and models. Force is provided to the DG connection by the tensioned bolt. The bolt is tensioned using the widely used torque method to 190 Nm (140 lb-ft) and the corresponding bolt force, F , is calculated using [Equation 5.8](#) [31]. The friction factor determined by MAADI Group Inc. is 0.5 for the stainless steel T-bolts [10]. The resulting bolt force from 140 lb-ft of torque on a 12.7 mm (1/2") diameter bolt is 23.9 kN.

$$F_f = \mu F_N \tag{5.7}$$

Where F_f is friction force in N, μ is friction coefficient, and F_N is normal force in N.

$$T = kFd \tag{5.8}$$

Where T is torque in Nm, k is friction factor, F is bolt force in N, and d is bolt diameter in mm.

The bolt force, F , is not equal to the normal force, F_N , since the point of contact between the steel and clamp is away from the bolt. Using equilibrium and the approximate distances between the point of contact, the bolt, and the fulcrum at the other end of the clamp, a normal force of 14.4 kN is calculated. The system is assumed to have two slip planes which are: the plane between the clamps and the steel, and the plane between the steel and the beam. An argument can be made that there are three slip planes since there are two clamps (there is another clamp on the non-visible side of the girder in [Figure 2.4](#)), but the clamps react simultaneously on the same plane. Therefore, the predicted strength of the clamping system is 8.6 kN.

Using the discussed equations, [Equation 5.9](#) was used to back-calculate friction coefficients for each test, as reported in [Table 5.6](#). Specimen S-MS-3 was torqued multiple times resulting in the highest peak load and a corresponding high friction coefficient. All of the clamp tests exceeded the predicted strength of 8.6 kN.

$$\mu = \frac{P}{2F_N} \tag{5.9}$$

Where μ is friction coefficient, P is the peak load from testing in N, and F_N is normal force in N.

Table 5.6: Friction coefficient for static clamp tests from design calculations.

Specimen	Mill Scale		Specimen	Sandblasted	
	Peak Load	Friction Coefficient		Peak Load	Friction Coefficient
S-MS-1	10.9 kN	0.38	S-SB-1	19.2 kN	0.67
S-MS-2	12.7 kN	0.44	S-SB-2	23.8 kN	0.83
S-MS-3	12.2 kN	0.42	S-SB-3	33.2 kN	1.15

The clamp test is modelled using FE similar to the brick models from the previous section. All of the assumptions previously stated are used and the geometry is simplified. Initially, the clamp test was modelled in its entirety including the GuarDeck® beam but the model would not converge due to the rigid body motion of the various parts. Namely, the custom T-Bolts do not fit perfectly in the T-slot. In reality, this does not matter as

the bolts will fall into position, but static analyses in FE are generally unable to account for sliding motions as it violates static equilibrium. The next problem was meshing the T-bolt. The ridges in the extruded clamp and beam cross-sections were removed from the beginning but the complex geometry of the bolt head is required to fit in the T-slot. Eventually, the T-bolts and beam were discarded in favour of a flat aluminum backplate, and a cylindrical I-shape representing the bolt and nut. The rigid body motion was still a concern as the clamp would generally need to rotate slightly to be in contact with the steel. This was remedied by making the steel slightly thicker than specified. All parts in contact were overlapped slightly (less than 1 mm) and surface-to-surface contact interactions were set to “remove overclosure”, which removed the overlap but kept the parts in contact. The last change was the geometry of the steel. It was a rectangular prism initially since this shape meshes well but one edge intersected the clamp in an unrealistic way. This edge was filleted to remove this intersection.

The final model is shown in [Figure 5.15](#), which shows the meshed model where a symmetry boundary condition is used on the hidden side. The backplate has a fixed boundary condition and the steel plate is pulled. The backplate and clamps are aluminum with the mill certificate elastic-plastic properties from [Table 5.2](#). The plate and the bolt are steel with linear-elastic properties. The friction coefficient throughout the model is 0.3.

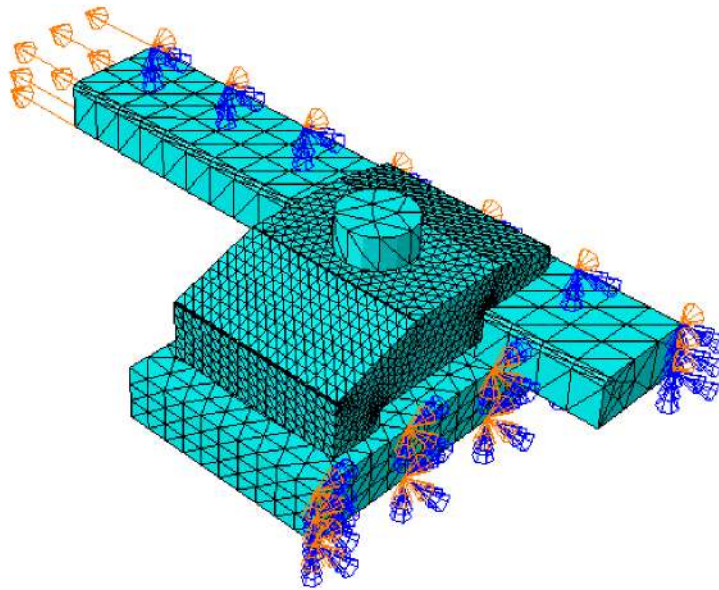


Figure 5.15: FE model for simulating clamp tests.

The bolts are pre-tensioned to the calculated force of 23.9 kN (from [Equation 5.8](#)) using the “Bolt Load” option in ABAQUS. This option shortens the shaft of the bolt until the specified force is achieved. After pre-tensioning, the steel plate is moved upwards either in displacement-control or force-control. This is similar to adjusting a test frame to either be displacement-controlled or load-controlled where all the experimental testing in this research was displacement-controlled. The steel is set to displace 1 mm upwards or to have a concentrated point load pull upwards until the maximum load. At the maximum load, the simulation aborts due to the connection being unable to carry more load; the steel moves and therefore, violates equilibrium.

Both the displacement-control and load-control cases can carry a maximum load of 10.0 kN, which is higher than the calculated value of 8.6 kN from the mechanics-based calculation. [Figure 5.16](#) shows the model under a concentrated load of 10 kN. The highest stresses in [Figure 5.16a](#) are located at the bolts due to the pre-tension load and the top of the steel due to the concentrated load pulling on the steel. This is ignored since the pre-tension and concentrated load are applied forces that cause stress concentrations. [Figure 5.16b](#) shows an exaggerated deformed shape where the clamp is rotated in the direction of the steel movement. The high stress location of interest is the edge of the clamp shown in [Figure 5.17](#) where the edge of the clamp presses into the edge of the steel as it rotates.

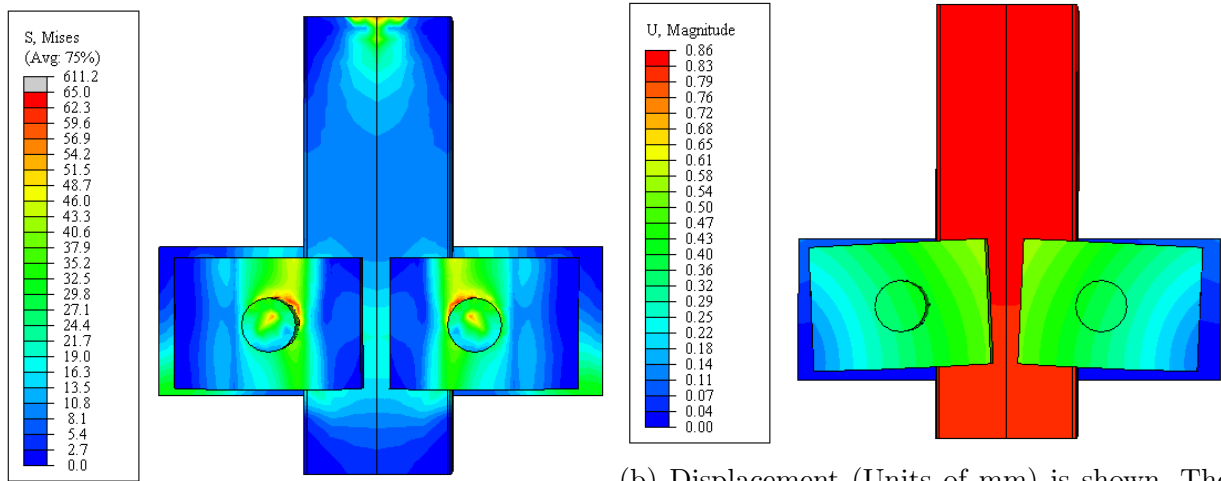
Although the calculations and FE are based on the same principals, the calculations are based on two slip planes, backplate & steel and clamp & steel. In reality, there are three slip planes. The third being the vertical face or edge of the clamp in contact with the edge of the steel, shown in [Figure 5.17](#). This was not accounted for in the calculation as there is zero normal force before loading. The normal force develops as the clamp rotates and the edge digs into the steel as was shown in [Figure 5.17](#). This is the location where delamination occasionally occurred ([Figure 4.15d](#)).

The applied, normal, and friction forces as the steel displaces upward are shown in [Figure 5.18](#). Note that the normal force for backplate & steel is plotted underneath the normal force for clamp face & steel. Additionally, the friction forces from the clamp face & steel and the clamp edge & steel are added together since they are in the same direction in the FE model. The displacement-controlled case is able to extend past the maximum load and remain constant, unlike the experiments, which had degradation of the slip planes. If the maximum values of the normal forces from backplate & steel and clamp face & steel are added together and multiplied by the friction coefficient such as in [Equation 5.10](#), the result is approximately equal to the calculated value of 8.6 kN. If the normal force from the clamp edge & steel is also added, as in [Equation 5.11](#), it is approximately equal to the friction force calculated by the FE model.

$$P = \mu(F_{(\text{backplate \& steel})} + F_{(\text{clamp face \& steel})}) \quad (5.10)$$

$$P = \mu(F_{(\text{backplate \& steel})} + F_{(\text{clamp face \& steel})} + F_{(\text{clamp edge \& steel})}) \quad (5.11)$$

Where P is the capacity of the clamp test in N, μ is friction coefficient, and F is normal force in N.



(a) Von Mises stress (Units of MPa) is shown. (b) Displacement (Units of mm) is shown. The deformation is scaled 15 times.

Figure 5.16: Stress and deformation of the model under 10 kN of load.

In comparison to the clamp tests, the FE result of 10 kN is closest to the S-MS-1 result of 10.9 kN (Table 4.1). This is sensible since the friction coefficient of 0.3 is a conservative value for mill scale surfaces as well as the minimum requirement for aluminum bridges from CSA S6, not the isolation layer and steel. If the friction force is calculated from the maximum total normal force, the capacity is 10.3 kN, which is closer to the lowest experimental result. The calculations in Table 5.6 are redone with a normal force of 34.3 kN, which is calculated from the sum of the maximum normal forces in Figure 5.18. The results in Table 5.7 are more accurate than the previous version of the table but less conservative.

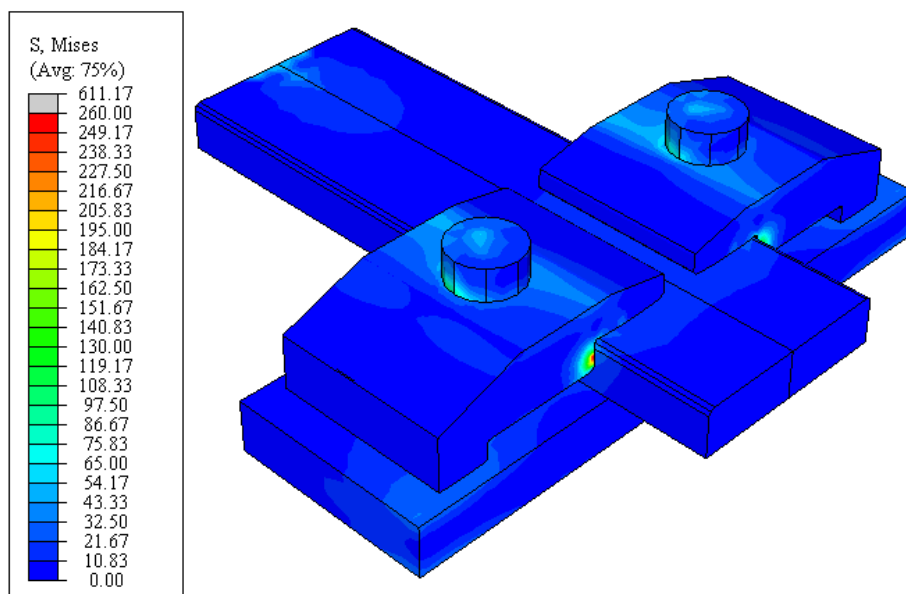


Figure 5.17: The high Von Mises stress (Units of MPa) between the clamp edge & steel is shown as a spot of red.

Table 5.7: Friction coefficient for static clamp tests from FE analysis.

Specimen	Mill Scale		Specimen	Sandblasted	
	Peak Load	Friction Coefficient		Peak Load	Friction Coefficient
S-MS-1	10.9 kN	0.32	S-SB-1	19.2 kN	0.56
S-MS-2	12.7 kN	0.37	S-SB-2	23.8 kN	0.69
S-MS-3	12.2 kN	0.36	S-SB-3	33.2 kN	0.97

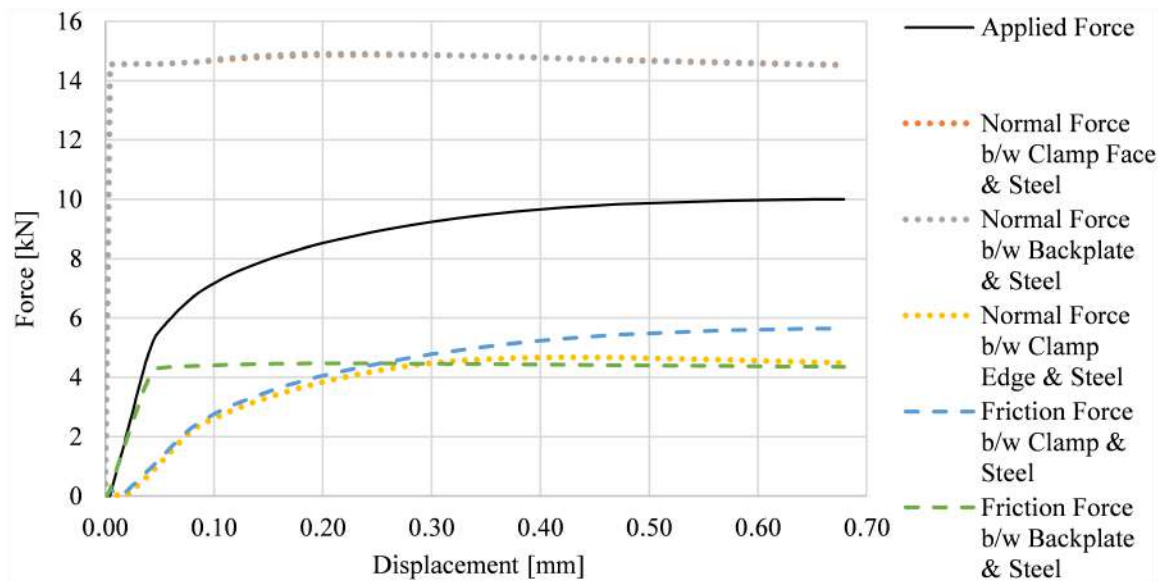


Figure 5.18: Comparison of the applied, normal, and friction forces plotted against the displacement of the steel.

Chapter 6

Deck-to-Girder Connections

The case study bridge is designed to carry live loads due to occasional maintenance vehicles and pedestrians. The deck-to-girder (DG) connections are responsible for transferring forces from the deck to the girders. The connections both hold the bridge components together vertically and resist horizontal forces such as vehicle braking. In the case of a bridge with dissimilar materials (e.g. an aluminum deck on steel girders), the DG connections must also resist or accommodate the thermal expansion of the different materials. These forces are discussed in [Section 2.5.2](#) and [Section 2.5.3](#). To study the effect of these forces on the DG connections, a parametric study was performed.

The study consists of varying parameters such as geometry, temperature, and vehicle location in an FE model and recording the absolute maximum force of all the DG connections also referred to as the DG reactions. The parameters are varied one at a time in an attempt to develop relationships between the applied loads and the DG reactions. The overall goal of the study is to begin development of a design tool for calculating DG reactions for an arbitrary bridge with arbitrary DG connections. The DG connections in the GuarDeck® system and the case study bridge are used as the base case of the parametric study and as an example later in this chapter. It is important to note that the parametric study presented is preliminary with only a few parameters varied.

6.1 FE Model

The following model is an extension of the work presented at the International Aluminium Conference (INALCO) in 2019 [\[24\]](#). One girder and a section of deck from the case study

bridge are modelled in 3D using 2D shell elements. The deck has the tributary width of the middle girder ($w = 1372$ mm). The I-shape of the girder is modelled, but the deck is composed of a single aluminum plate on top of the steel, and has a thickness equal to the top flange of a GuarDeck® beam ($t = 6$ mm). Contact between the deck and the girder is modelled but friction is omitted to reduce run time. As a design tool, it can be assumed that the connections carry the entire load instead of dividing the load between friction and the DG connection force. The shell elements are offset (i.e. the location of the nodes is not necessarily at the center of the plate) to ensure the pin and roller boundary conditions are at the bottom of the section and not in the middle of the bottom flange. The FE model is shown in [Figure 6.1](#).

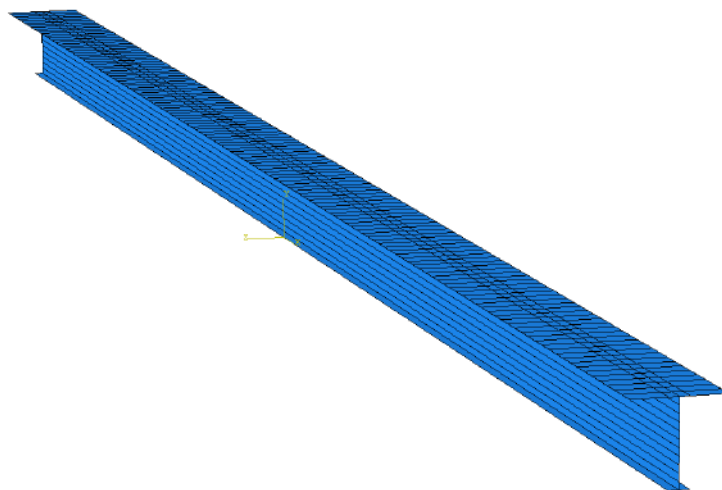


Figure 6.1: FE model used to study DG reactions under applied loads.

The deck and girder are connected using 1D, linear, spring elements representing the DG connections. Three sets of springs for X, Y, and Z are used where the spring stiffness in the long direction of the bridge is variable and the other two directions have nearly infinite spring stiffness ($k \rightarrow \infty$) to prevent rigid body motion of the deck. A value of 10^{10} N/mm is used for infinite spring stiffness since the spring forces or DG reactions do not change significantly at higher stiffnesses. The variable spring stiffness ranged from 10^0 N/mm to 10^{10} N/mm. At 10^0 N/mm, the deck may slide off the girders if a horizontal force is applied, and at 10^{10} N/mm, the bridge will exhibit “full” composite action. The spring spacing is constant and based on the case study bridge. If the length of the bridge is changed from the case study, the new length is a multiple of the spring spacing. The unstretched spring length is zero and the stretched length is calculated by dividing the spring force by the stiffness. The first step of the study is develop a relationship between spring force with

infinite stiffness and a parameter. The second step is to form a relationship between the spring force with infinite stiffness and other spring stiffnesses for the particular parameter. The numerical results of the analytical parametric study are located in [Appendix C](#).

6.2 Thermal and Braking Parameters

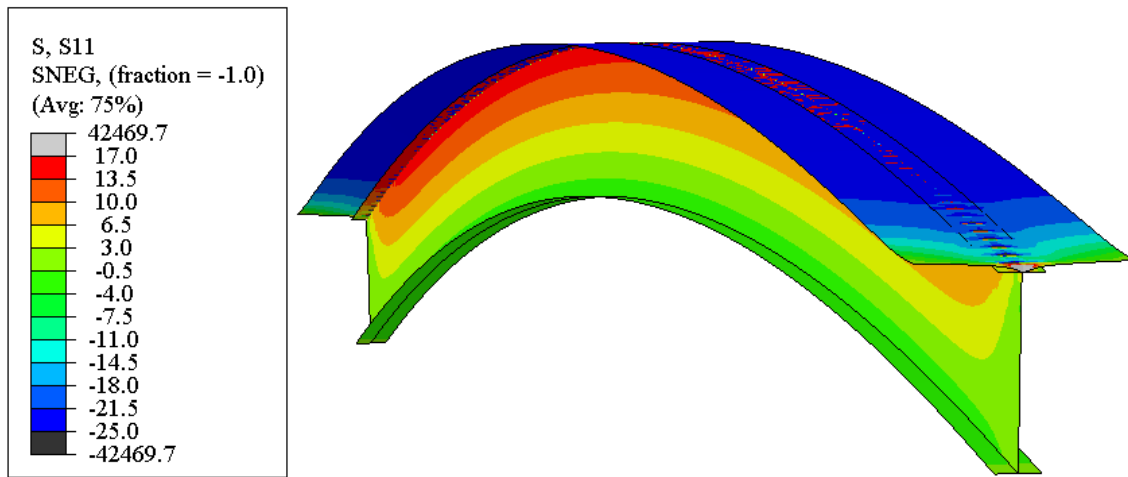
As discussed in [Section 2.5.2](#), the thermal parameters are dependent on the bridge type and cross-section depth, where an aluminum deck on steel girders was assumed to be Type A (i.e. thermally conductive). The depth of the case study bridge is over 1 m and therefore the bottom of the cross-section is 10°C cooler than the top according to [Figure 2.12b](#). The case study bridge is located in the Montreal region where the maximum effective temperature of the bridge is 51°C and was calculated using the maximum mean daily temperature (i.e. 30°C for Montreal), [Table 2.1](#), and [Figure 2.12a](#). The initial temperature or construction temperature specified by CSA S6 is 15°C [5]. In summary, the thermal expansion base case begins at 15°C then the top and bottom of cross-section increase to 51°C and 41°C, respectively, with a linear gradient in between. Only the extreme high temperature case is considered.

From the vehicle braking discussion in [Section 2.5.3](#) and the tire loads described in [Section 3.1.1](#), the static braking force is 13.3 kN for the wheel load.

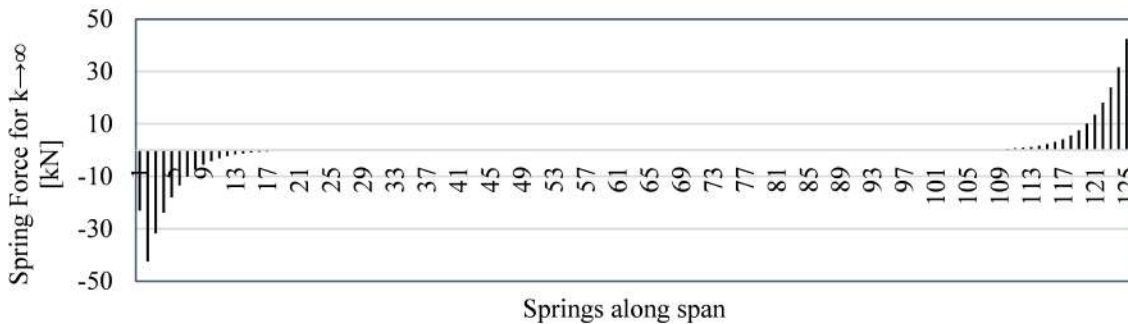
6.3 Thermal Analysis

The thermal expansion base case (i.e. Montreal conditions and case study bridge geometry) with infinite spring stiffness ($k \rightarrow \infty$) is shown in [Figure 6.2](#). [Figure 6.2a](#) shows the stress distribution in the long direction of the bridge, where the steel girder is in tension (i.e. positive stress) and the aluminum deck is in compression (i.e. negative stress) because the aluminum expands more than steel but the steel restricts the expansion. [Figure 6.2b](#) shows the spring force or DG reaction at every spring along the span. The highest spring force due to thermal expansion always occurs near the supports in the case study.

The second variable bridge parameter is deck width, where it is 1372 mm in the base case. [Figure 6.3a](#) shows the spring stiffness curves, which all begin at approximately zero force for zero spring stiffness and plateau at infinite spring stiffness. [Figure 6.3b](#) shows the results of the spring forces with infinite stiffness as a function of deck width and contains a fitted logarithmic equation for calculating spring forces for an arbitrary deck width.



(a) Stress (units of MPa) in the long direction of the bridge (deformation is scaled 50 times).

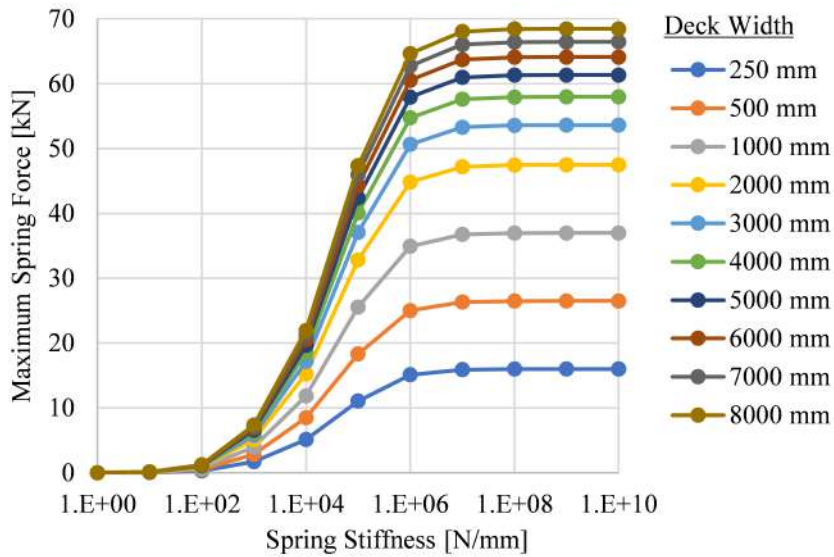


(b) Spring forces along the span.

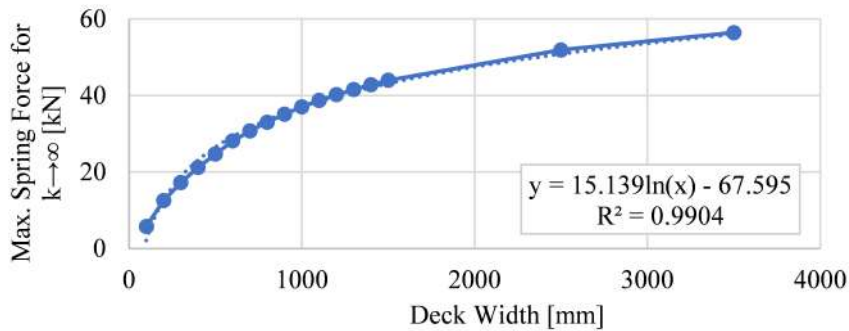
Figure 6.2: Results of the case study FE model under thermal expansion conditions for Montreal ($k \rightarrow \infty$, $w = 1372$ mm, $t = 6$ mm).

The next parameter is deck thickness. Similar spring stiffness curves are shown in [Figure 6.4a](#), whereas [Figure 6.4b](#) shows a curve that is less well represented by a logarithmic equation so a polynomial is used. The fitted equation appears to underestimate the spring force at higher loads, therefore more points or a different relationship may be warranted.

The deck width and thickness results are compared to a deck with constant area. The constant deck area is 1372 mm multiplied by 6 mm, where the width and thickness are decreased and increased proportionately to one another. For example, the deck width may be 686 mm and the proportional thickness is 12 mm. [Figure 6.5](#) shows the deck width and deck thickness results, as well as the constant area results, as a function of deck area.



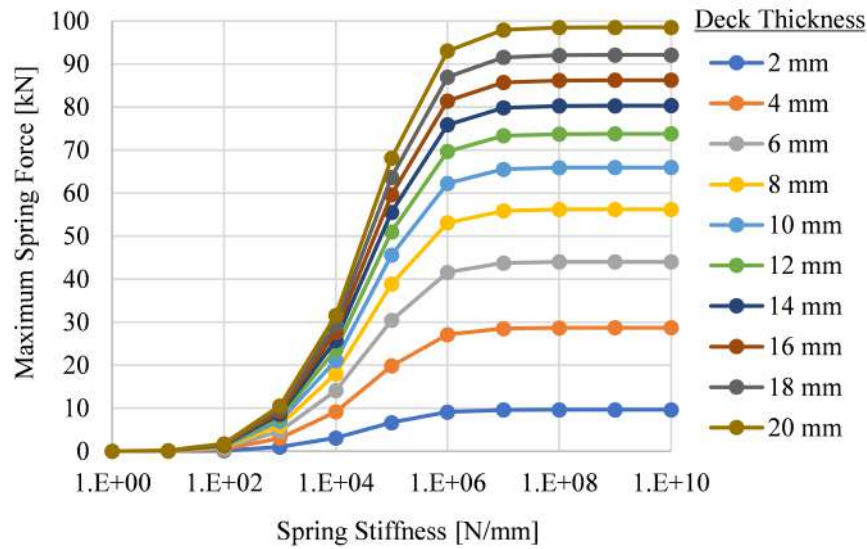
(a) Maximum spring force as a function of deck width and spring stiffness.



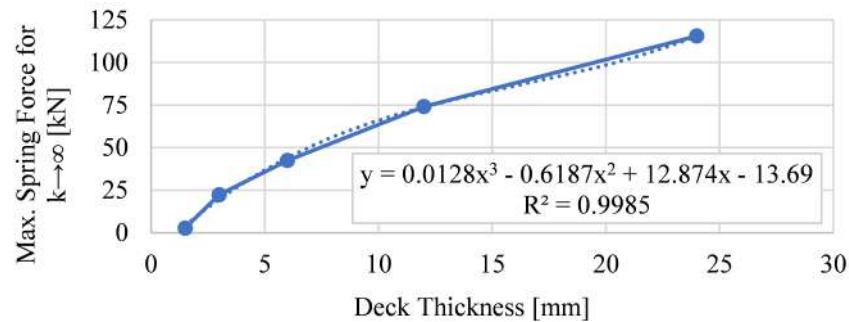
(b) Maximum spring force as a function of deck width with infinite spring stiffness ($k \rightarrow \infty$).

Figure 6.3: Maximum spring force as a function of deck width.

The Variable Width and Variable Thickness lines demonstrate that increasing thickness is more effective at increasing the maximum spring force. Simultaneously, keeping the area constant can result in any maximum spring force depending on the proportion of area allocated to width and thickness. Although not shown, increasing deck thickness increases the maximum spring force in the Constant Area line. The phenomenon may be caused by shear lag due to the wide cross-sections (e.g. the corners of the deck are unstressed) or



(a) Maximum spring force as a function of deck thickness and spring stiffness.



(b) Maximum spring force as a function of deck thickness with infinite spring stiffness ($k \rightarrow \infty$).

Figure 6.4: Maximum spring force as a function of deck thickness.

increased moment of inertia from increasing the thickness, resulting in a stiffer bridge.

Temperature parameters are varied as well. The case study has a maximum temperature difference of 36°C where the top of the deck starts at 15°C and increases to 51°C . The maximum temperature difference is made a variable in Figure 6.6. The relationship between the maximum spring force and temperature difference is simpler than the previous relationships and essentially forms a straight line. The stiffness curves are linearly-scaled

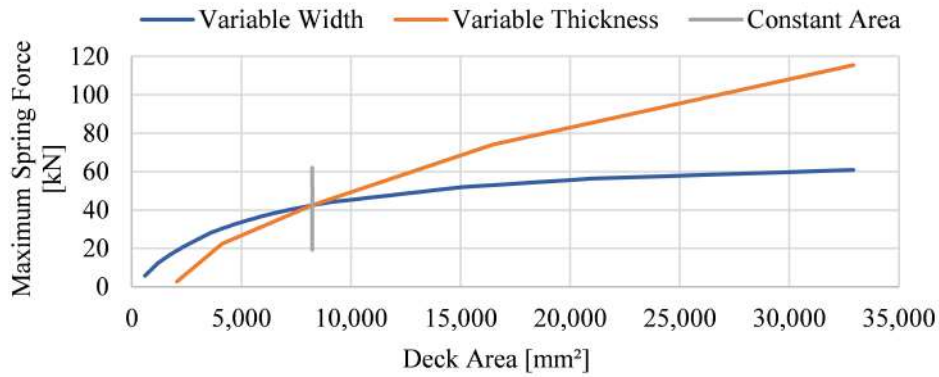
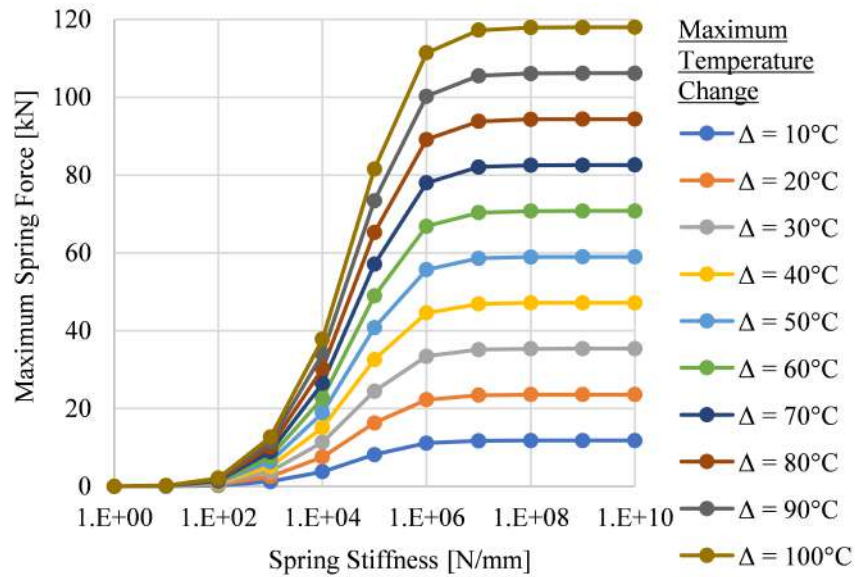


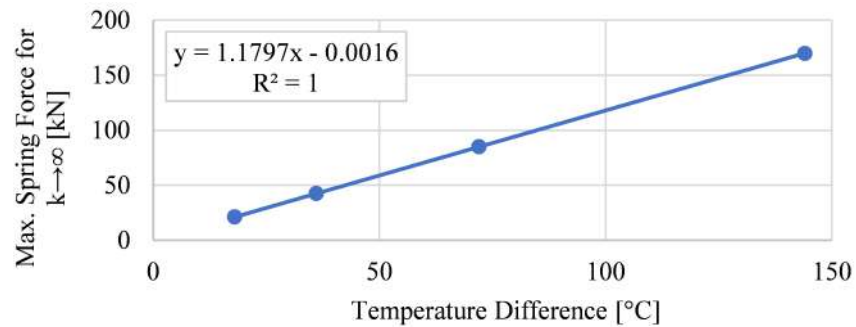
Figure 6.5: Maximum spring force as a function of deck cross-section area with infinite spring stiffness ($k \rightarrow \infty$).

versions of each other.

A second temperature parameter, the gradient, is made a variable. The case study value of 10°C of linearly decreasing temperature from the top of the deck to the bottom of the girders is varied in Figure 6.7. Figure 6.7b shows a linear relationship but is inconsequential since there is no practical difference when the gradient is changed as shown in Figure 6.7a where all of the curves are plotted on top of each other.

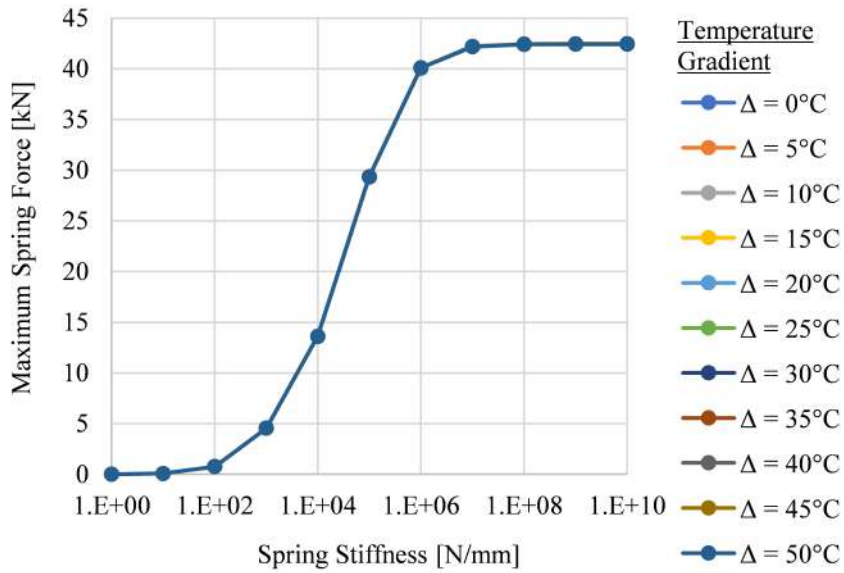


(a) Maximum spring force as a function of maximum temperature change and spring stiffness.

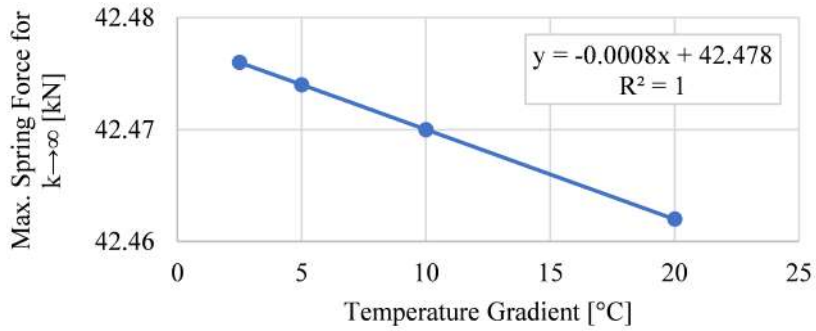


(b) Maximum spring force as a function of maximum temperature change with infinite spring stiffness ($k \rightarrow \infty$).

Figure 6.6: Maximum spring force as a function of maximum temperature difference.



(a) Maximum spring force as a function of temperature gradient and spring stiffness.



(b) Maximum spring force as a function of temperature gradient with infinite spring stiffness ($k \rightarrow \infty$).

Figure 6.7: Maximum spring force as a function of temperature gradient.

6.4 Braking Force

Relationships between the static braking force and spring forces are studied in this section. A force for the weight of the vehicle acting on a tire, labelled gravity, appears simultaneously with the braking force in most cases since braking does not occur alone in reality. The gravity force is 53.1 kN and the braking force is 13.3 kN as shown in [Figure 6.8](#). The dynamic load allowance is not used.

Since the tire is a point load in one discrete location on the span, results for only three locations are reported; the middle of the span and the two ends of the bridge above the supports. There is no difference between the two ends of the bridge when gravity is applied by itself but the results change when braking is applied. When the braking load is at the end of the span and points towards the middle of the bridge, it is labelled as arriving. This represents the vehicle driving onto the bridge and braking. When the braking point load is at the end of the span and points away from the bridge, it is labelled as exiting. This represents the vehicle driving off the bridge and braking. Whether the pin or roller is on the arriving or exiting side of the bridge made no difference to the results.

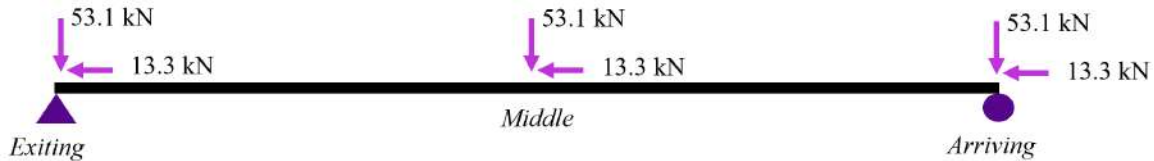
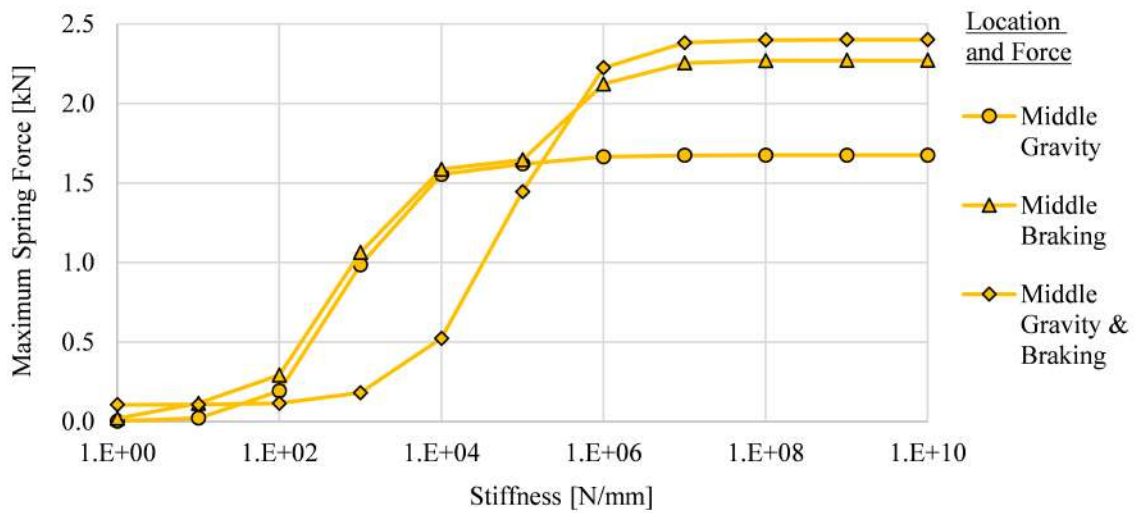
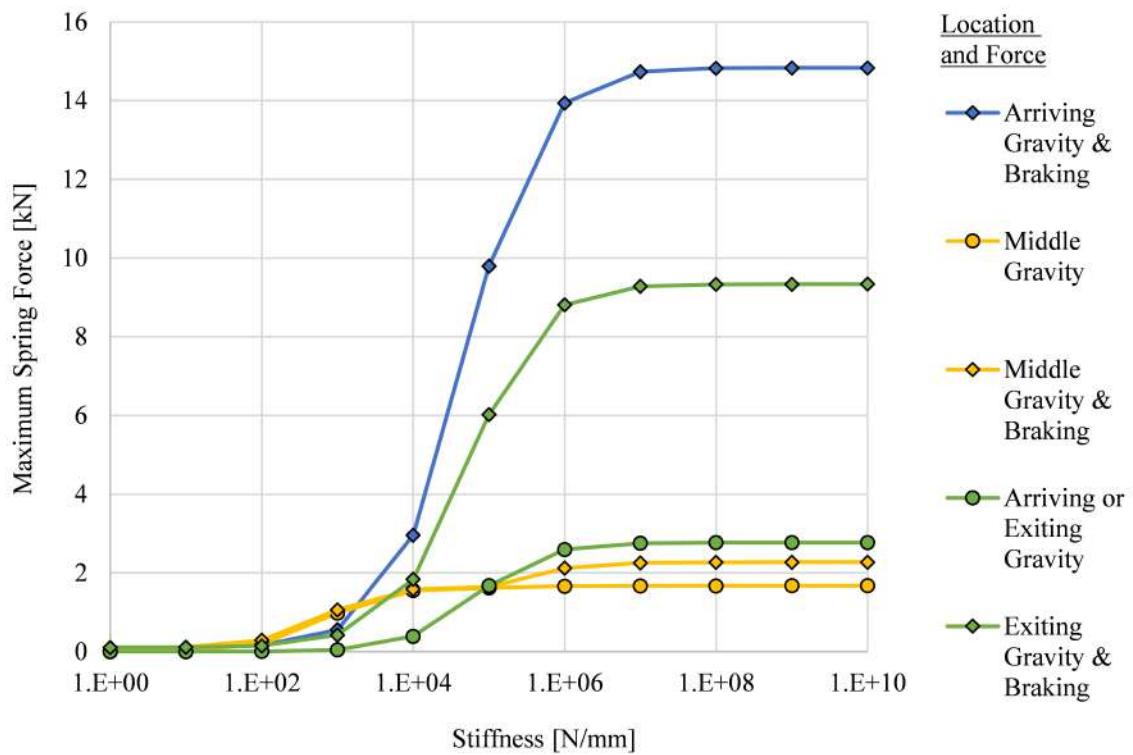


Figure 6.8: Gravity force (53.1 kN) and braking force (13.1 kN) at three locations on the case study bridge.

[Figure 6.9a](#) shows the results for gravity and braking in the middle of the bridge. The braking force is applied alone to demonstrate that the maximum spring forces are governed by gravity at lower spring stiffnesses and by braking at higher stiffnesses. This is different from the arriving and exiting cases where maximum spring force is approximately equal to the sum of gravity and braking. The maximum spring forces for all arriving, middle, and exiting cases are shown in [Figure 6.9b](#). The case with gravity and braking on the arriving side governs for nearly all spring stiffnesses, except for a short section around a stiffness of 10^3 N/mm, where the middle case governs. The difference is minimal and could likely be ignored in most bridge applications. The maximum value for the arriving case is 14.8 kN, which was found to not change with span. Note that this value is higher than the braking load of 13.3 kN because there is extra force on the connection due to gravity. The spring forces along the 5 m span are shown in [Figure 6.10](#), where one spring carries the majority of the load for both cases.



(a) Maximum spring force as a function of vehicle location and spring stiffness.



(b) Maximum spring force as a function of vehicle location with infinite spring stiffness ($k \rightarrow \infty$).

Figure 6.9: Maximum spring force as a function of vehicle location.

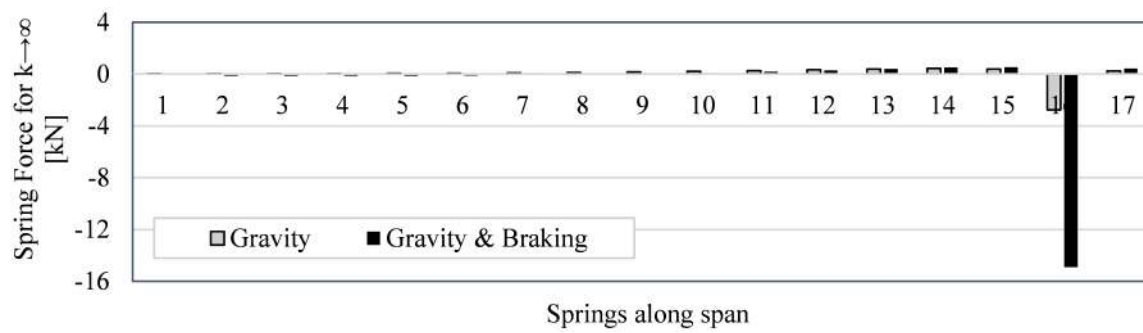


Figure 6.10: Spring forces due to gravity and braking along the length of a 5 m case study bridge.

6.5 GuarDeck® Example

This section is an extension of the previously mentioned CSCE paper [25]. The relationships presented in this chapter are incomplete and difficult to apply to any arbitrary bridge but the overall goal is to develop tools to design DG connections in a bridge efficiently. If an engineer knows the stiffness of a connection, theoretically or through experiments, an engineer can use the relationships shown in the previous figures to determine the DG reaction and compare it to the applied load.

The DG connections of the GuarDeck® system are used as an example, where the stiffness of the connection is determined by drawing a secant line between zero and the peak load on the load-displacement graph discussed in Section 4.2, where the slope of the secant is taken as the stiffness. Figure 6.11 shows the secant line of S-SB-2, which has a stiffness of 5.4 kN/mm or 5.4×10^3 N/mm. Other lines could be drawn, for example, the tangent between 0 mm and 1 mm, but it is convenient to use the secant from zero to the peak load so the force can be assumed to increase linearly until the peak load. The stiffnesses of the other clamp tests are found in Table 6.1. The stiffnesses across the clamp tests are not consistent and may be caused by the inconsistent distribution of grit in the isolation layer. In addition, more clamp tests should be performed for an accurate estimate of the DG connection strength.

Using the base case of the parametric study (i.e. the case study bridge) and Figure 6.6b, the maximum spring force is 42.5 kN if the connection stiffness is infinitely high. Figure 6.6a is used to find the spring force corresponding to a spring stiffness of 5.4×10^3 N/mm. One of the curves is linearly-scaled to correspond to a maximum value of 42.5 kN and a spring force of 9.0 kN is linearly interpolated. The Arriving Gravity & Braking curve from Figure 6.9b is used for determining the spring force due to braking. For a spring stiffness of 5.4×10^3 N/mm, the corresponding spring force is 1.8 kN. The resulting spring forces or DG reactions of 9.0 kN (thermal) and 1.8 kN (vehicle gravity and braking) added together are less than the peak DG resistance of 19.2 kN for S-SB-2. The corresponding spring extension for the thermal load is less than 2 mm. The DG reactions and the DG resistances are not factored. However, from this demonstration it can be seen how the method can simplify the tedious process of building models for every bridge.

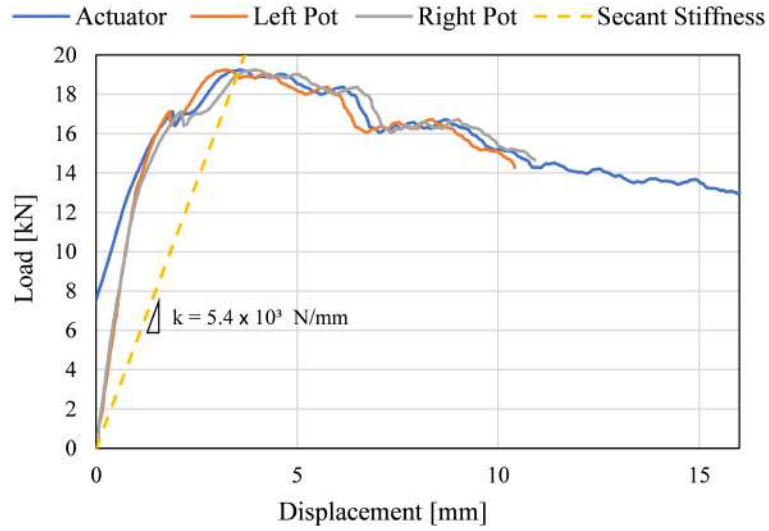


Figure 6.11: S-SB-2 secant stiffness.

Table 6.1: Secant stiffness for static clamp tests.

Specimen	Mill Scale		Specimen	Sandblasted	
	Resistance	Secant Stiffness		Resistance	Secant Stiffness
S-MS-1	10.9 kN	4400 N/mm	S-SB-1	19.2 kN	5400 N/mm
S-MS-2	12.7 kN	1600 N/mm	S-SB-2	23.8 kN	7100 N/mm
S-MS-3	12.2 kN	3500 N/mm	S-SB-3	33.2 kN	12300 N/mm

Chapter 7

Conclusions & Recommendations

This chapter contains conclusions based on the findings of this thesis and recommendations for future work.

7.1 Conclusions

The goal of this research is to investigate the structural behaviour of a new aluminum bridge deck product called GuarDeck®[®], the mechanical connections in particular, and to develop tools for future aluminum bridge design. Recalling the research objectives presented in [Section 1.1](#), the following sections present conclusions for each objective.

7.1.1 Experimental Testing of the Beams

Two experiments were designed to test the GuarDeck®[®] bridge deck product in a laboratory setting. The first experiment was designed to test the deck panels, also referred to as beams. The beams were tested as simply-supported elements with a single tire load. The following conclusions are made based on this work:

- The length of the span can change the governing failure mode. In the case of Test 1B-T-S (650 mm span), even though the beam was simply-supported, the usual causes of the failure; bending, longitudinal shear, and bearing were not present. Instead, the top flange ruptured. In contrast, Test 1B-T-L (2 m span) was also asymmetrically loaded but acted as a simply-supported beam and failed due to bending.

- The placement of the load when multiple beams are connected also changed the failure mode. The difference between Tests 2B-T and 2B-G was the location of the load on either side of the tongue and groove connection holding them together. The results showed that Test 2B-T failed by bending whereas the tongue and groove connection failed in Test 2B-G.
- Tests 3B-M and 2L1S-M reinforced the conclusion that the tongue and groove connection is the weakest link in GuarDeck®. Although the load was evenly distributed to two sets of tongue and groove connections, the groove-side connection failed. Additionally, this failure mode has minimal ductility.

7.1.2 Experimental Testing of the DG Connections

The second type of experiment was designed to test the deck-to-girder (DG) connections, since it is difficult to theoretically estimate how much resistance the connections can provide due to the many slip planes, unknown friction coefficients, and uncertainty of the bolt force. The following conclusions are made based on this work:

- The clamp tests showed that the DG system does not immediately lose capacity when the peak load is reached. The resistance gradually reduces as the isolation layer is worn down, as evidenced by the dust found under the specimen during the experiments.
- As was predicted, the rougher surface of the SB specimens resulted in higher peak loads than the smoother MS specimens.
- Specimen S-SB-3 demonstrated that the peak load can be increased if the bolt is tensioned again after wearing of the isolation layer.

7.1.3 Beam Tests Compared to Design Provisions and FE Analysis

The results of the beam tests were compared to the CSA S157 beam calculations [6]. The following conclusions are made based on this work:

- The failure mode of Test 1B-T-S was not predicted by the beam calculations but the value of the peak load was closely approximated. This is likely a coincidence as

ultimate tensile stress at the bottom flange probably occurred nearly simultaneously with the ultimate shear stress at the top flange. Shear failure has minimal ductility, while tensile beam failure has more ductility and therefore, a crack developed in the shear location first. Predicting the shear failure of the top flange is difficult using CSA S157 because the analysis would need to be done in 3D.

- The CSA S157 calculations predicted the failure load for the 2 m span tests, except Test 2L1S-M, at the transition from linear material properties to plastic. This is a result of the linear-elastic theory used to determine moment resistance where the equation is based on linearity and the ultimate strength input uses plastic properties.
- The equations were conservative - so much so that the failure load of the tongue and groove connection was higher than the CSA S157 results. In general, CSA S157 can be used to conservatively calculate the ultimate strength of the beams even if the connection fails. It is important to note that the analysis used the averaged mill certificate properties. The CSA S157 properties would be more conservative.

Subsequently, the results of the beam tests were compared to shell and brick models, where both types of models represent the experiments in 3D but shell models were composed of 2D shell elements and brick models were composed of 3D brick elements. The following conclusions are made based on this work:

- The shell models adequately predicted the peak load of the beams that did not fail due to the connection and could generally predict the behaviour of all of the beams prior to the peak load.
- The brick models were able to predict the behaviour of tongue and groove failures due to the connections being modelled, but should be used with caution since the predicted peak load was less accurate as model complexity increased. As the brick models with connection failure increased in complexity, from Test 2B-G to Test 3B-M to Test 2L1S-M, the predicted capacities were less accurate.
- In Test 1B-T-S, the brick model showed high stress at the tension flange and the top flange where the rupture occurred.
- Neither the shell nor brick models accurately predicted displacement in the plastic regions of the graphs but material properties were simplified from the mill certificates and softening was not included.

- The two FE models and the beam calculations serve to validate each other, especially if laboratory testing is not available. This is particularly important in the early stages of design, where the deck cannot be tested until it is ready to be produced at full-scale.

7.1.4 Clamp Tests Compared to Design Provisions and FE Analysis

The experimental results of the clamp tests were compared to mechanics-based design calculations, which resulted in conservative estimates of the capacity. Consequently, when the friction coefficient was calculated from the experimental results, the friction coefficients were much higher than the assumed value of 0.3 for MS. The clamp tests were also compared to a 3D FE model where the geometry was simplified and a friction coefficient of 0.3 was used. The following conclusions for both structural analysis methods are made based on this work:

- The mechanics-based calculation gave a very conservative estimate of the MS specimen capacity. The calculation accounts for the normal forces between the clamp face and the steel as well as the steel and the beam. Another face of the clamp is in contact with the steel in the initial configuration (i.e. before testing) but the normal force is zero.
- The FE model also provided a conservative estimate of the MS specimen capacity but was less conservative than the calculation. When the steel displaces, the clamps rotate in the direction of the movement and an edge is pressed against the steel, sometimes causing delamination of the isolation layer. The FE model captured the rotation and calculated a corresponding normal force.
- From both analysis methods, the friction coefficient of 0.3 for mill scale and the isolation layer was found to be a conservative value. This is important to note since the value is intended to be representative for aluminum in contact with aluminum, steel in contact with steel, or aluminum in contact with steel.

7.1.5 DG Reactions under Thermal and Braking Loads

The DG connection analysis in [Chapter 6](#) consisted of an analytical parametric study conducted using FE to begin to determine how the applied forces of braking and thermal

expansion affect the reaction of the DG connections. Various parameters were systematically increased and decreased in an FE model of a case study bridge. The highest force in the springs connecting the deck and girders, representing DG connections with arbitrary linear stiffness, along the span was recorded and plotted against the parameter. The linear stiffness of the springs was variable and ranged from practically zero stiffness to nearly infinite stiffness. Relationships were developed between the parameter and the spring force associated with infinite stiffness as well as between infinite stiffness and lower stiffnesses. The goal was to easily identify the highest force a DG connection with a particular stiffness would be required to resist. The results of this study are preliminary but the following conclusions are drawn from the results:

- The maximum spring force relationships with *deck width* and *deck thickness* are non-linear. The non-linearity is currently quantified using fitted logarithmic and polynomial equations. Furthermore, increasing *deck thickness* is more efficient at increasing maximum spring force than increasing *deck width*.
- The relationship between the parameter *maximum temperature difference* and the maximum spring force is linear where any stiffness curve that was developed can be linearly scaled for any temperature difference.
- The relationship between the parameter *temperature gradient* and the maximum spring force is linear but insignificant since increasing or decreasing the gradient value hardly changed the results.
- The weight of a vehicle (only one tire was used for this study) plus an associated braking force was placed at three locations on a case study bridge span. The first was *arriving* where the vehicle was moving onto the bridge, the second was *middle* where the vehicle was in the middle of the span, and the third was *exiting* where the vehicle was moving off of the bridge. The *arriving* case governed for nearly all stiffnesses and this did not change with span length. One spring directly below the vehicle braking load carries the entirety of the braking force plus more due to gravity.

7.2 Recommendations

The objectives listed in [Section 1.1](#) were written as a task list to be finished to some extent by the end of this research. All tasks have results that can be improved or expanded. The following sections give insight into what may be improved or the next steps for each task.

7.2.1 Experimental Testing of the Beams

A smaller subset of the beams was tested in comparison to what was originally planned. Due to the COVID-19 pandemic, fatigue testing was put on hold and was still paused at the time of writing this thesis. Fatigue and other recommendations for experimental testing of the beams are as follows:

- The beam tests could have included a negative bending test. That is, conduct Test 1B-T-L but flip the beam up-side down. The GuarDeck® system was designed in Quebec, Canada where it is expected to be installed across three girders, which would induce negative bending.
- A beam test using the clamps would have provided useful information regarding how the clamps react under real loads as opposed to the clamp tests in [Section 3.2](#).
- Fatigue testing of the beams was postponed at the time of writing this thesis. The two confirmed fatigue tests which are scheduled to be done are:
 - Test the set-up from Test 2B-G under constant amplitude, cyclic loading ranging from 12.5 kN to 50 kN.
 - Test the set-up from Test 2L1S-M under constant amplitude, cyclic loading. Loading will be determined based on the results of the first fatigue test.
- As mentioned in [Section 7.1.1](#), the tongue and groove connection is a governing failure mode and should be improved in the next design iteration of the product.

7.2.2 Experimental Testing of the DG Connections

Similar to the beam tests, the clamp tests were intended to have a fatigue component. In addition, many other surface finishes could have been tested in this arrangement. The following are recommendations for future clamp tests:

- The clamp tests should have included a surface finish with corrosion-resistant paint such as the one used on the case study bridge girders but the cost of a small amount of the paint was prohibitive.
- The clamps should be tested to failure in the short direction of the bridge. There is load, although minor, in this direction and the failure mode is unclear.

- In [Section 7.1.2](#) where it is stated that the peak load could be increased if the bolt is re-tensioned after the isolation layer is worn down, testing the clamps without the grit could result in higher peak loads. The force would be distributed more evenly over the blue part of the isolation layer resulting in slower wear.
- The fatigue portion of the clamp tests is scheduled to be done under quasi-static, cyclic loading. Both the mill scale and sandblasted surface finishes are to be tested.

7.2.3 Beam Tests Compared to Design Provisions and FE Analysis

The relevant CSA S157 calculations [6] for the beam tests were completed, but there are multiple factors involved that are difficult to account for in these types of calculations. To continue this task, calculations from different codes could be performed. The Aluminum Design Manual (ADM) and Eurocode 9: Design of Aluminium Structures contain the design provisions for aluminum structures in the USA and Europe, respectively. Calculations from both of these could be compared to the CSA S157 and experimental results.

The FE models of the beam tests could certainly be improved. The recommendations for improving this work and future models are as follows:

- Higher-order elements should have been used for the brick modelling of the beams but the size of the model and computation time prevented this. If more processing power is available, higher-order brick elements should be tested.
- No mesh convergence study was completed for any of the models as the models are large. Either more computing power is needed or smaller models could be used. For the beam tests, a symmetry condition could have been used to halve the number of elements.
- The tire load could be modelled more realistically as a steel plate on top of rubber on the beam. In addition, the results may be closer to the experimental results if the tire load is applied as a displacement instead of a force.

7.2.4 Clamp Tests Compared to Design Provisions and FE Analysis

Improving the mechanics-based calculations would be difficult as calculating the normal force between the clamp edge and steel requires assumptions including rotation of the

clamps and normal force as a function of rotation. Continuing the FE analysis is more obvious and recommendations for future work are as follows:

- Include the beam geometry and the custom T-bolt in the clamp test.
- Model the clamps as part of beam tests.

7.2.5 DG Reactions under Thermal and Braking Loads

The end goal of the study is far from accomplished and much more work is needed for the ideas presented to be useful for designing a bridge with an aluminum deck and steel girders. Some of the next steps in this study might include:

- A relationship could be determined between the spring force and a more useful cross-section parameter than deck width or thickness. A more useful cross-section parameter for example could be a function of moment of inertia.
- The next step for the thermal expansion results would be to develop a mechanics-based method for calculating spring force as a function of temperature difference. The equation for shear flow may be useful for this endeavour.
- The study included summer thermal expansion conditions because deck buckling is a concern since aluminum expands twice as much as steel. Relationships should be developed for winter conditions as well as summer. The relationship would certainly be linear but still important for design.
- Only three locations were used for the vehicle braking portion of this preliminary study. Every point should be checked to ensure the spring forces do not increase any higher than the arriving case and an influence line could be developed for this purpose.
- Similar to the thermal expansion results, it would be useful to develop a mechanics-based equation between the braking force and the resulting maximum spring forces as well as develop relationships between maximum spring force and bridge geometry.

References

- [1] Paul Arrien, Josée Bastien, and Denis Beaulieu. Rehabilitation of bridges using aluminum decks. *Canadian Journal of Civil Engineering*, 28(6):992–1002, 2001.
- [2] Subodh K. Das and J. Gilbert Kaufman. Aluminum alloys for bridges and bridge decks. In *The Minerals, Metals & Materials Society Annual Meeting*, number May, pages 61–72, 2007.
- [3] J. Dobmeier, B. Barton, J. Gomez, P. Massarelli, and W. McKeel Jr. Failure Study of an Aluminum Bridge Deck Panel. *Journal of Performance of Constructed Facilities*, 15(May):68–75, 2001.
- [4] Mychèle Gagnon, Valérie Gaudreault, and Donald Overton. Age of Public Infrastructure : A Provincial Perspective. Technical Report 11, Statistics Canada: Investment and Capital Stock Division, Ottawa, Canada, 2008.
- [5] CSA Group. *CAN/CSA S6-14: Canadian Highway Bridge Design Code*. Mississauga, Canada, 2014.
- [6] CSA Group. *CAN/CSA S157-17: Strength Design in Aluminum*. Toronto, Canada, 2017.
- [7] Osman Hag-Elsafi and Sreenivas Alampalli. Cost-effective rehabilitation of two aluminum bridges on Long Island, New York. *Practice Periodical on Structural Design and Construction*, 7(3):111–117, 2002.
- [8] Torsten Höglund and Lars Nilsson. Aluminium in bridge decks and in a new military bridge in Sweden. *Structural Engineering International: Journal of the International Association for Bridge and Structural Engineering (IABSE)*, 16(4):348–351, 2006.
- [9] Applied Bolting Technology Products Inc. DTI installation and inspection, n.d.

- [10] MAADI Group Inc. Bridge deck. Email, 2019.
- [11] MAADI Group Inc. Photo of bridge with GuarDeck, 2019.
- [12] MAADI Group Inc. Diagram of GuarDeck clamping system, 2020.
- [13] MAADI Group Inc. GuarDeck flyer: Weld-free bridge decking, 2020.
- [14] ASTM International. *ASTM B308/308M-10: Standard specification for Aluminum-alloy 6061-T6 standard structural profiles*. West Conshohocken, PA 19428-2959, 2010.
- [15] Julien Leclerc. Utilisation innovatrice de l'aluminium dans les ponts : Effets de la variation de la température sur le comportement structural d'un tablier à platelage d'aluminium sur poutres d'acier, à action composite. diploma thesis, Université Laval, 2018.
- [16] Johan Maljaars, Frans Soetens, and IJsbrand Van Straalen. Fatigue of aluminium bridge decks. *Structural Engineering International: Journal of the International Association for Bridge and Structural Engineering (IABSE)*, 16(4):305–311, 2006.
- [17] Federico M. Mazzolani. *Aluminum alloy structures*. E and FN Spon, London, England, 2 edition, 1995.
- [18] Federico M. Mazzolani. Aluminium structures in refurbishment: Case of the real Ferdinando bridge on Garigliano river. *Structural Engineering International: Journal of the International Association for Bridge and Structural Engineering (IABSE)*, 16(4):352–355, 2006.
- [19] Federico M. Mazzolani. Structural applications of aluminium in civil engineering. *Structural Engineering International: Journal of the International Association for Bridge and Structural Engineering (IABSE)*, 16(4):280–285, 2006.
- [20] Aluminium Association of Canada. Portrait of the canadian primary aluminium industry, 2018.
- [21] American Association of State Highway and Transportation Officials (AASHTO). AASHTO LRFD bridge design specifications. September 2017.
- [22] Ontario. Ministry of Transportation. Quality and Standards Division. *Ontario highway bridge design code*. Government of Ontario, 2 edition, 1991.

- [23] Ichiro Okura, Nobuyasu Hagiwara, Makoto Naruo, and Hitoshi Toda. Fatigue behavior of aluminum deck fabricated by friction stir welding. *Structural Engineering/Earthquake Engineering*, 20(1):55s–67s, 2003.
- [24] Melanie Perreault, Scott Walbridge, and Alexandre de la Chevrotiere. Key challenges of developing an aluminum bridge deck. pages 258–259, Tokyo, 2019. International Aluminum Conference.
- [25] Melanie Perreault, Scott Walbridge, and Alexandre de la Chevrotiere. Theoretical and experimental analysis of a modular aluminum bridge deck. Saskatoon, 2020. Canadian Society for Civil Engineering (CSCE) Annual Conference.
- [26] Muhammad A. Saleem, Amir Mirmiran, Jun Xia, and Kevin MacKie. Alternative deck system for moveable bridges. In *Structures Congress 2010*, pages 403–416, 2010.
- [27] Muhammad A. Saleem, Amir Mirmiran, Jun Xia, and Kevin MacKie. Experimental evaluation of aluminum bridge deck system. *Journal of Bridge Engineering*, 17(1):97–106, 2012.
- [28] Tomasz Siwowski. Aluminium bridges - Past, present and future. *Structural Engineering International: Journal of the International Association for Bridge and Structural Engineering (IABSE)*, 16(4):286–293, nov 2006.
- [29] Tomasz Siwowski. FEM modelling and analysis of a certain aluminium bridge deck panel. *Archives of Civil Engineering*, 55(3):347–365, 2009.
- [30] Lars Svensson and Lars Pettersson. Aluminium Extrusion Bridge Rehabilitation System. *Bridge Management*, pages 777–783, 1990.
- [31] Engineering ToolBox. Bolt torque calculator, 2018.
- [32] Viami International Inc. and The Technology Strategies Group. Market Study for Aluminium Use in Roadway Bridges. Technical report, Viami International Inc. & The Technology Strategies Group, Montreal, Canada, 2013.
- [33] LG Vigh. Virtual experiments of fsw-fabricated aluminium structural elements. In *Proceedings of the sixth conference on Computational structures technology*, pages 243–244, 2002.
- [34] Scott Walbridge and Alexandre de la Chevrotière. Opportunities for the use of aluminum in vehicular bridge construction. 2012.

APPENDICES

Appendix A

Experimental Results

This appendix contains the experimental results presented in [Section 4.1](#).

A.1 Beam Tests

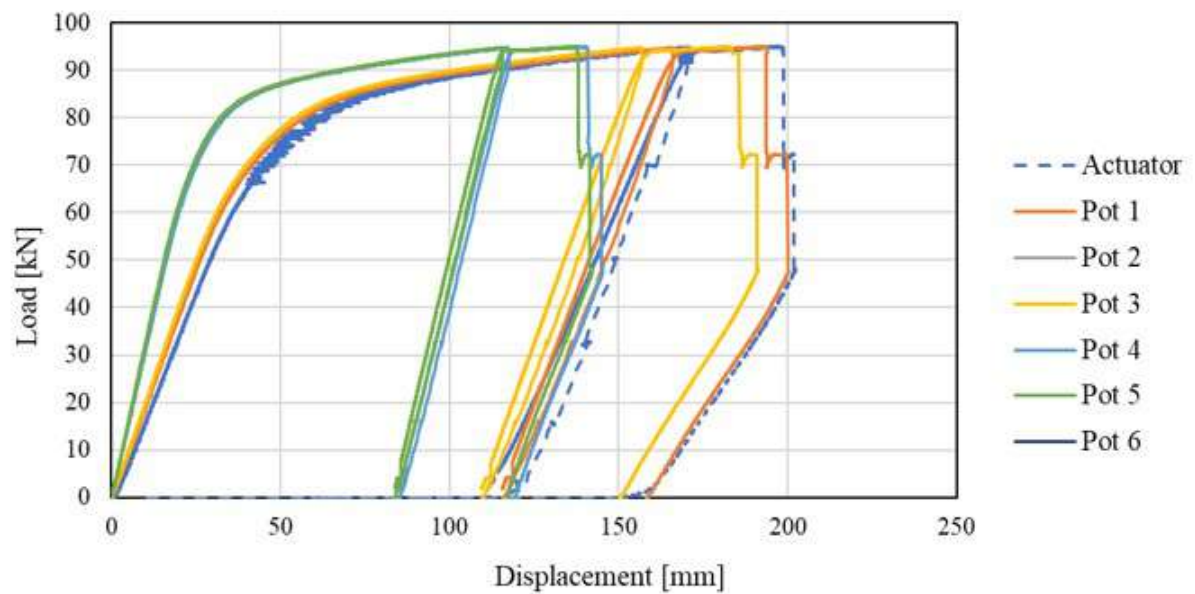


Figure A.1: Load-displacement graph for Test 1B-T-L.

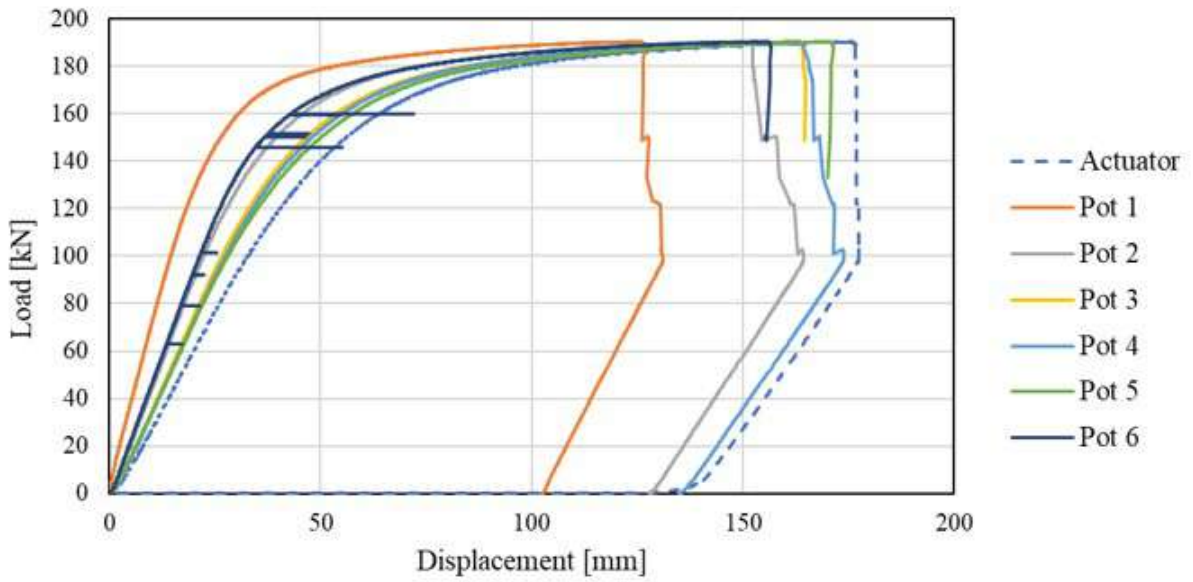


Figure A.2: Load-displacement graph for Test 2B-T.

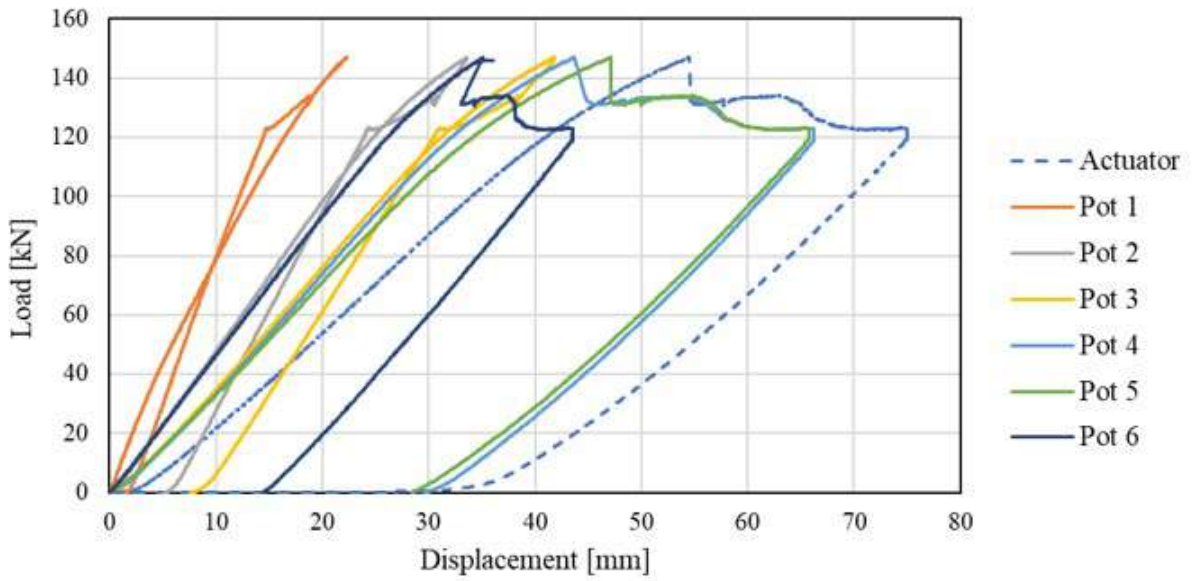


Figure A.3: Load-displacement graph for Test 2B-G.

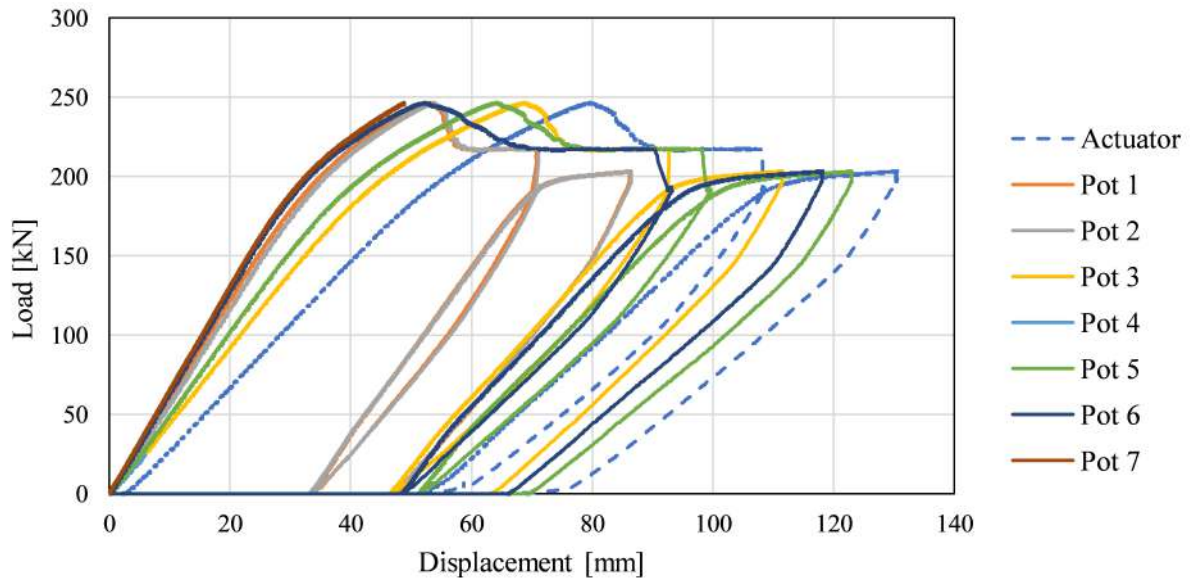


Figure A.4: Load-displacement graph for Test 3B-M.

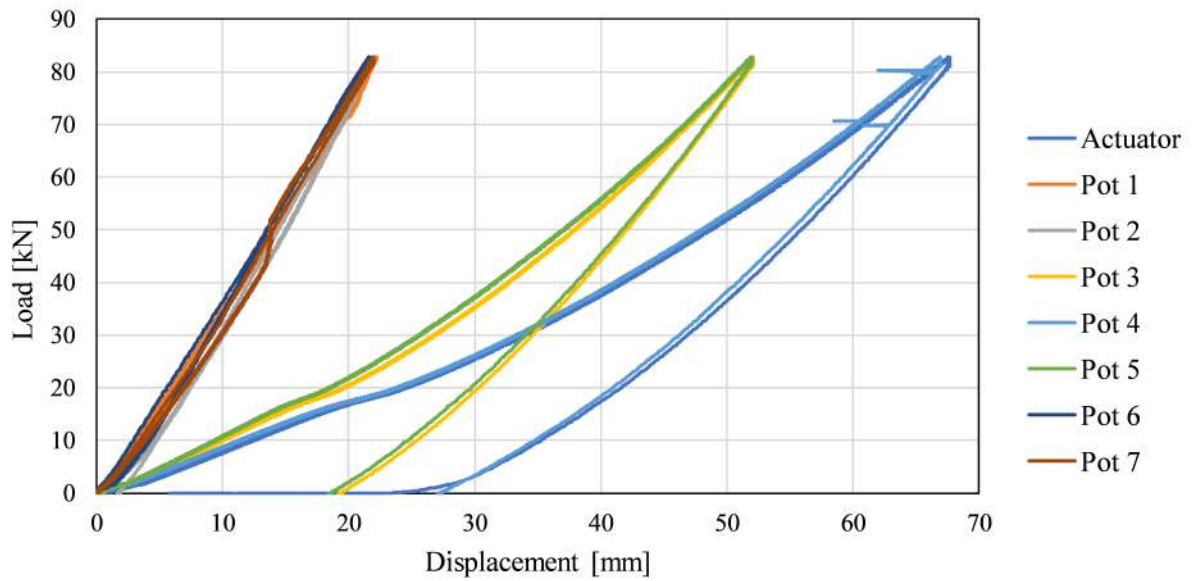


Figure A.5: Load-displacement graph for Test 2L1S-M attempt 1.

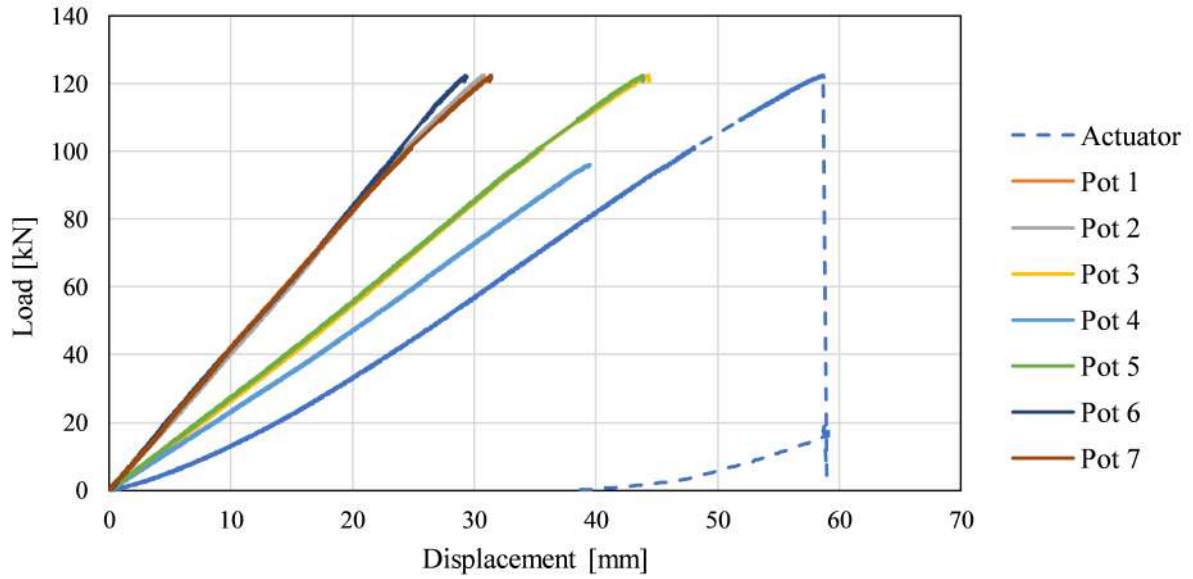


Figure A.6: Load-displacement graph for Test 2L1S-M attempt 2.

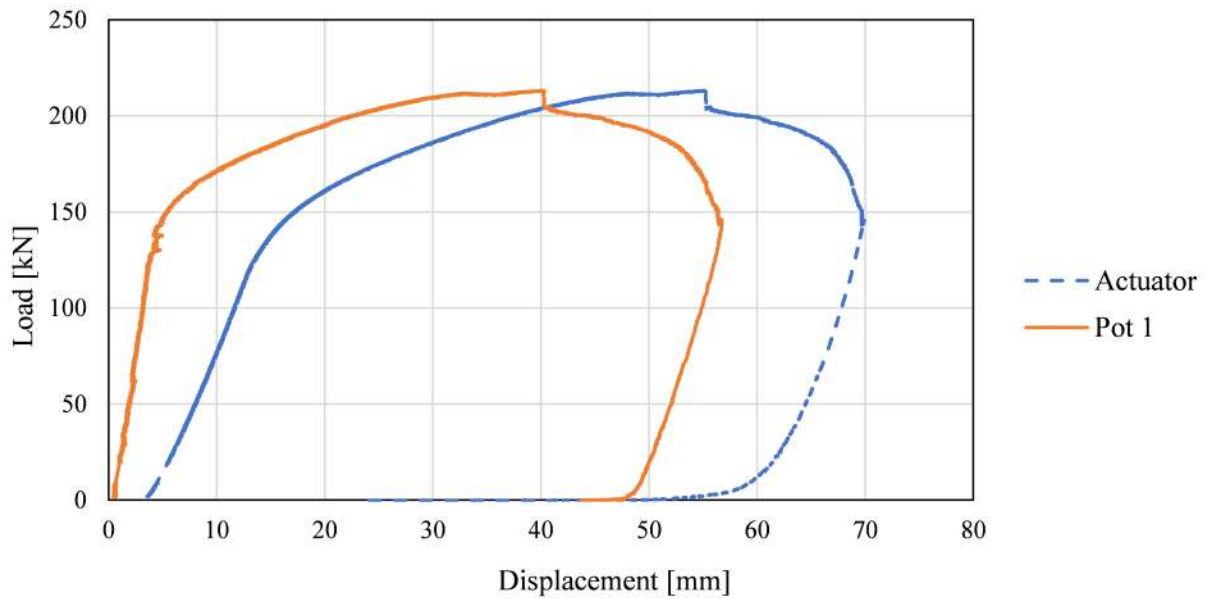


Figure A.7: Load-displacement graph for Test 1B-T-S.

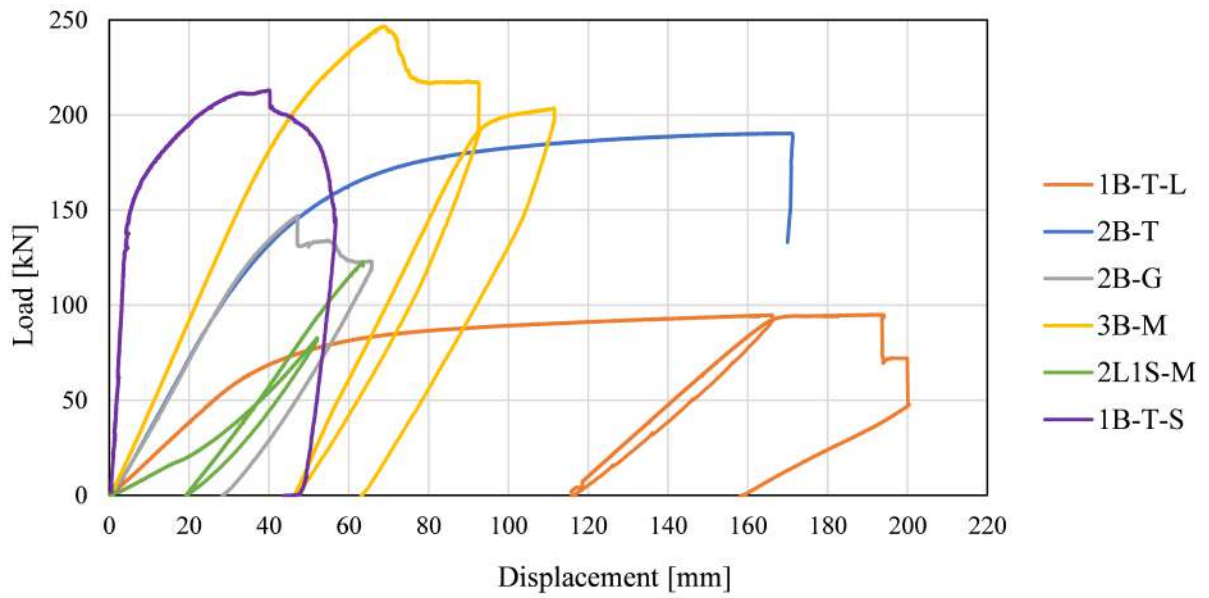


Figure A.8: Comparison of all beam tests.

A.2 Clamp Tests

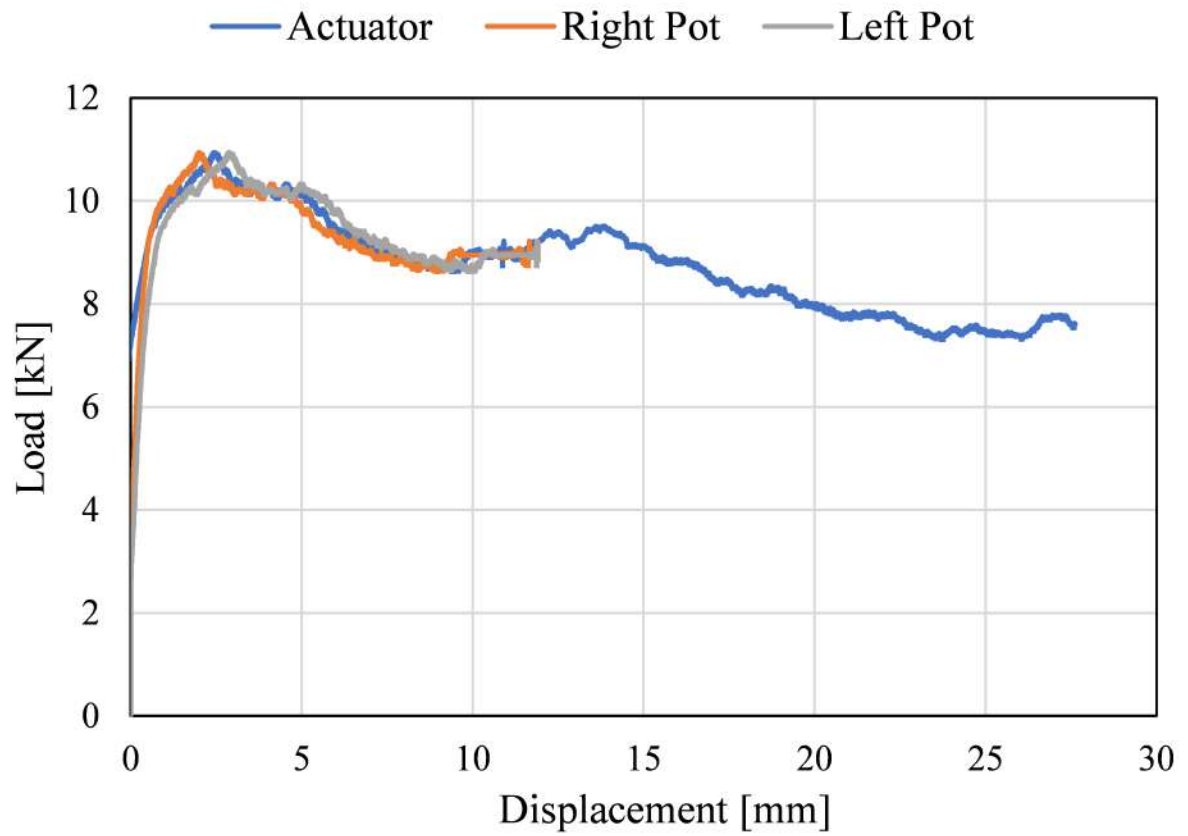


Figure A.9: Load-displacement graph for S-MS-1.

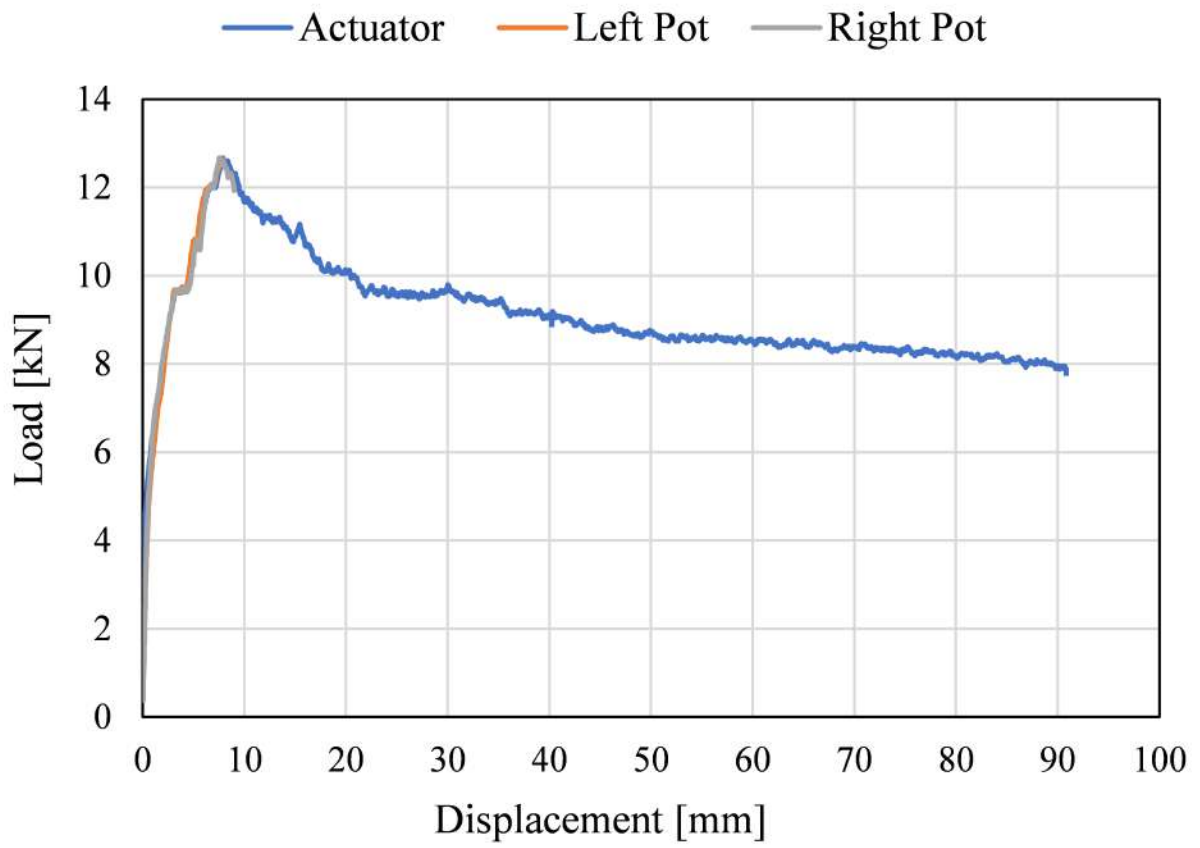


Figure A.10: Load-displacement graph for S-MS-2.

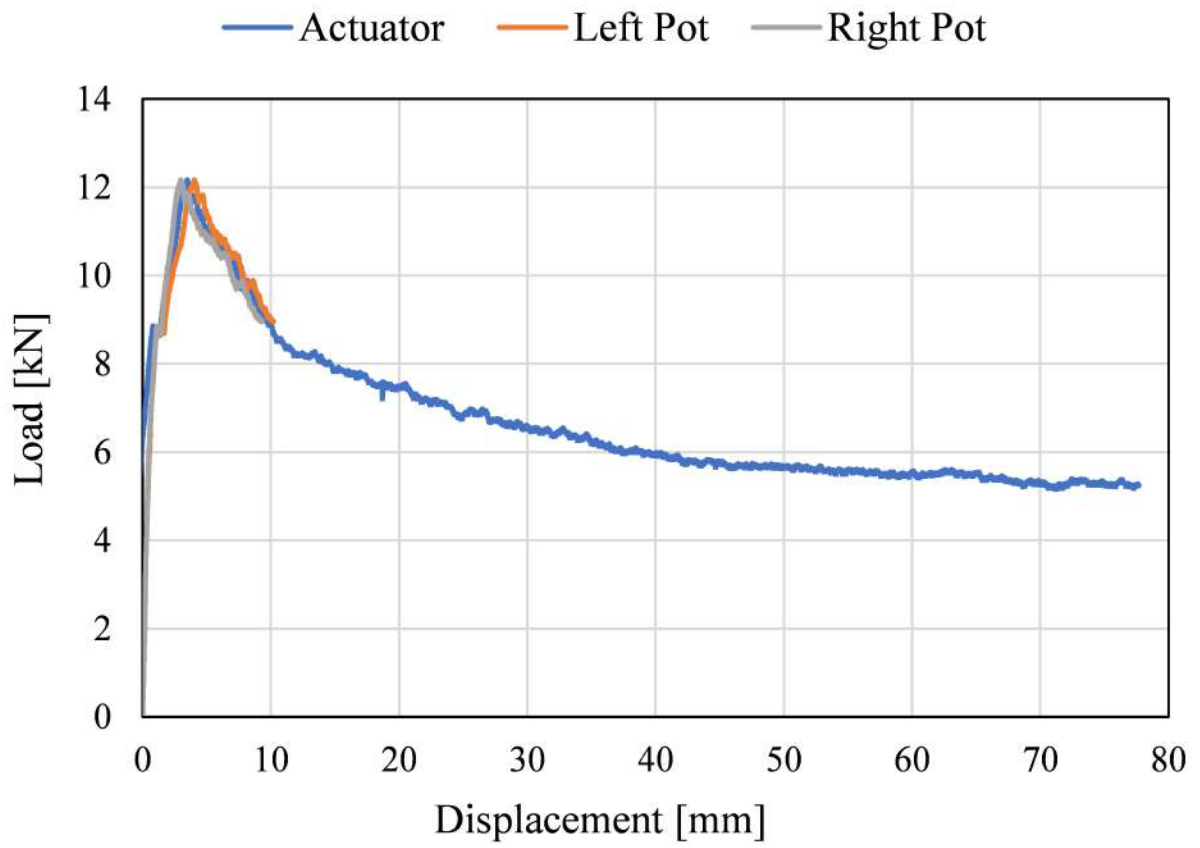


Figure A.11: Load-displacement graph for S-MS-3.

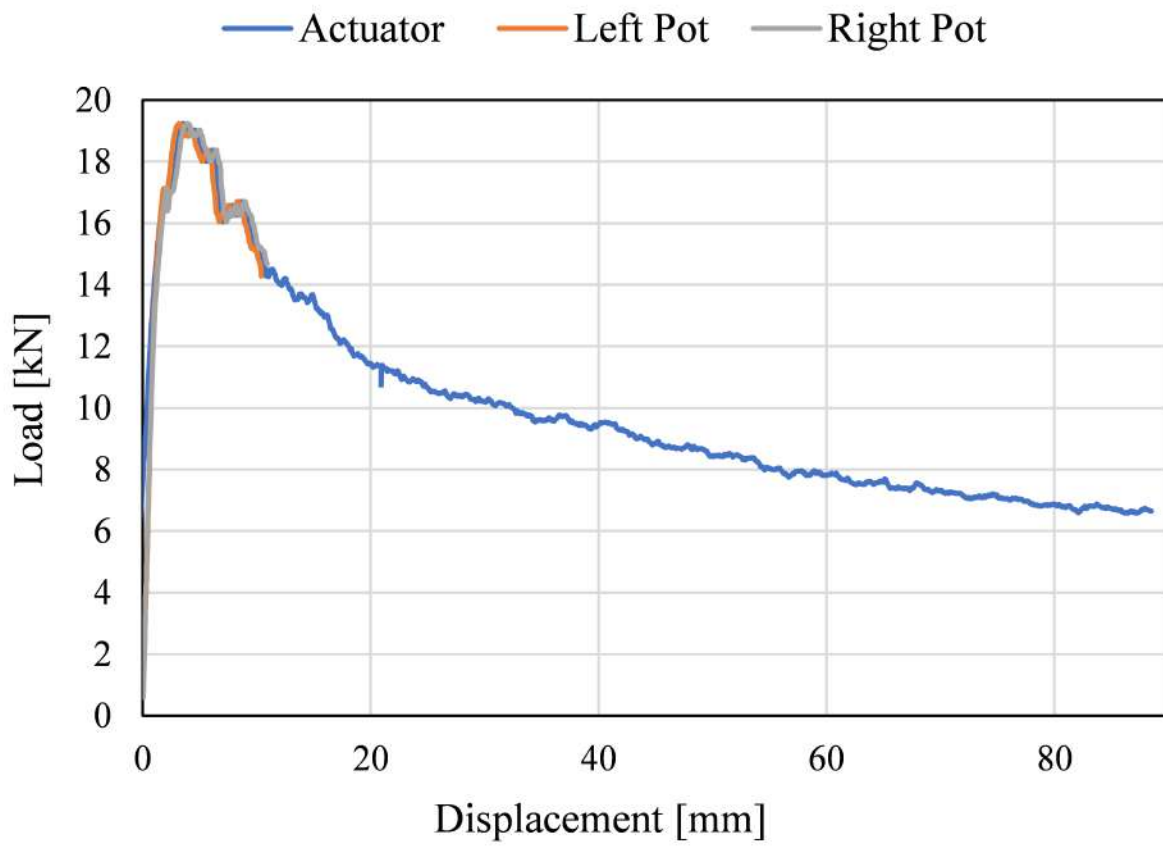


Figure A.12: Load-displacement graph for S-SB-1.

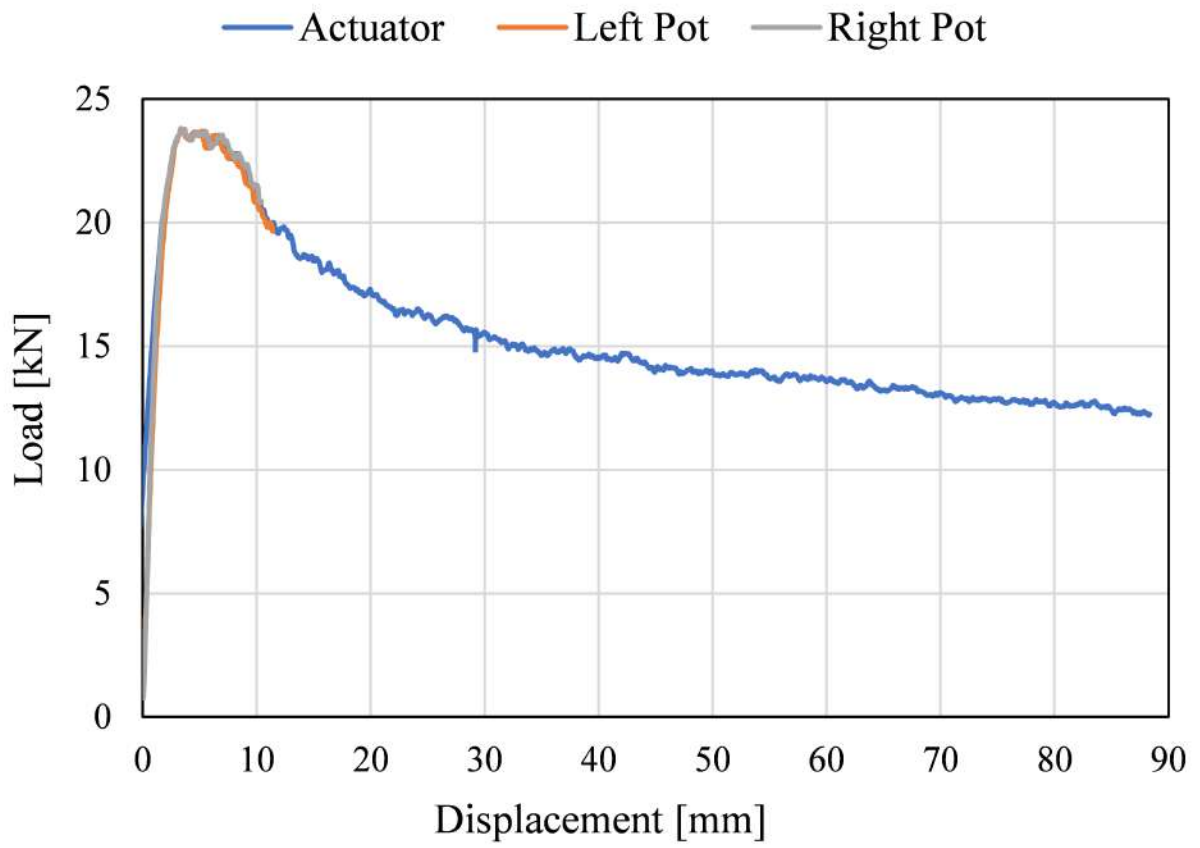


Figure A.13: Load-displacement graph for S-SB-2.

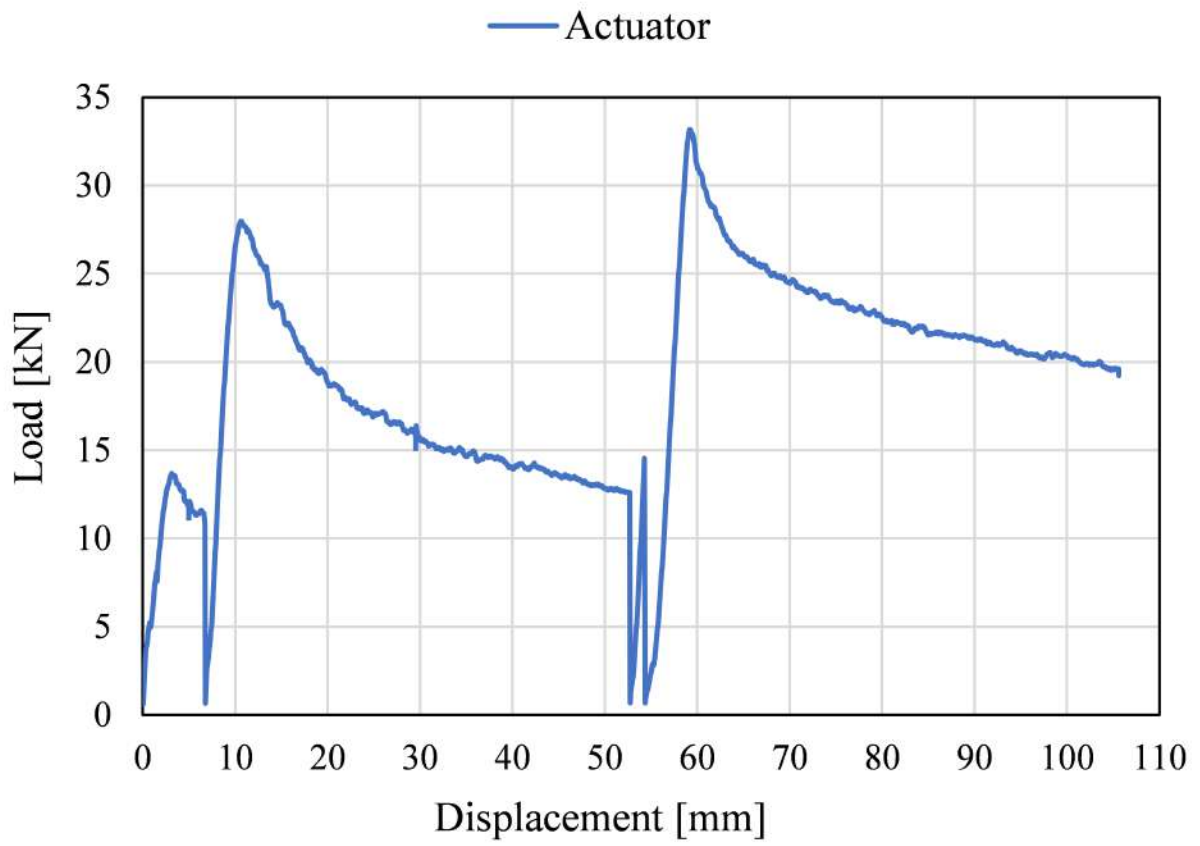


Figure A.14: Load-displacement graph for S-SB-3.

Appendix B

Beam Calculations

This appendix contains the beam calculations. The calculations are based on CSA S157 and are done both sets of material properties in Table 5.2.

B.1 Sample Calculation

The CSA S157 beam calculations for Test 1B-T are provided in this section.

B.1.1 Bending

Assume beam is not subject to lateral-torsional bending.

Clause 7.5.2.2 Elements in uniform compression

For components in bending, such as decking profiles, where $\frac{a}{w} < 2.5 \frac{b}{t}$

$$\frac{a}{w} = \frac{70.39 \text{ mm}}{4.5 \text{ mm}} = 15.642 < 2.5 \frac{b}{t} = 2.5 \frac{110.68 \text{ mm}}{6.5 \text{ mm}} = 42.569 \Rightarrow \text{ok!}$$

$$m = 1.25 + 0.2 \frac{\frac{a}{w}}{\frac{b}{t}} = 1.25 + 0.2 \frac{\frac{70.39 \text{ mm}}{4.5 \text{ mm}}}{\frac{110.68 \text{ mm}}{6.5 \text{ mm}}} = 1.434 < 1.65 \Rightarrow \text{ok!}$$

$$\lambda = \frac{mb}{t} = \frac{(1.434)(110.68 \text{ mm})}{6.5 \text{ mm}} = 24.413$$

Clause 10.1.1 Factored compressive strength and limiting stress

$F_0 = F_y$ when there is no welding or local buckling, the yield strength of the base material

Clause 10.1.2 Normalized slenderness

$$\bar{\lambda} = \frac{\lambda}{\pi} \sqrt{\frac{F_0}{E}} = \frac{24.413}{\pi} \sqrt{\frac{240 \text{ MPa}}{70,000 \text{ MPa}}} = 0.455$$

Clause 11.1 Classification of members in bending

$$0.3 < [\bar{\lambda} = 0.455] < 0.5 \Rightarrow \text{ok!}$$

Class 2 Section: capable of carrying moment up to the onset of yielding in compression without local buckling.

Clause 11.2 Moment resistance of members not subject to lateral-torsional buckling (LBT)

For class 2 sections:

for compression fibres:

$$M_r = \phi_y M_y = \phi_y S F_y = \phi_y \frac{I}{y_{Top}} F_y = (0.9) \frac{6.18 \times 10^6 \text{ mm}^4}{36.462 \text{ mm}} (240 \text{ MPa}) = 36.589 \text{ kNm}$$

for tension fibres:

$$M_r = \phi_u S_n F_u = \phi_u \frac{I}{y_{Bottom}} F_u = (0.75) \frac{6.18 \times 10^6 \text{ mm}^4}{52.863 \text{ mm}} (260 \text{ MPa}) = 22.783 \text{ kNm}$$

Peak Load and Deflection

$$P_r = \frac{4M_r}{L} = \frac{4(22.783 \text{ kNm})}{2 \text{ m}} = 45.6 \text{ kN}$$

$$\Delta = \frac{PL^3}{48EI} = \frac{(22.8 \times 10^3 \text{ N})(2000 \text{ mm})^3}{48(70,000 \text{ MPa})(6.18 \times 10^6 \text{ mm}^4)} = 18 \text{ mm}$$

B.1.2 Shear

12.1.2 Flat webs without stiffeners

$$F_0 = 0.6F_y = 0.6(240 \text{ MPa}) = 144 \text{ MPa}$$

$$\lambda_s = 1.4 \frac{h}{w} = 1.4 \frac{70.39 \text{ mm}}{4.5 \text{ mm}} = 21.899$$

$$\bar{\lambda} = \frac{\lambda_s}{\pi} \sqrt{\frac{F_0}{E}} = \frac{21.899}{\pi} \sqrt{\frac{144 \text{ MPa}}{70,000 \text{ MPa}}} = 0.316$$

Clause 10.1.3 Buckling stress

$\alpha = 0.2$ for unwelded fully heat-treated columns, beams, and elements $\bar{\lambda}_0 = 0.5$ for elements

$$\beta = \frac{1 + \alpha(\bar{\lambda} - \bar{\lambda}_0) + \bar{\lambda}^2}{2\bar{\lambda}^2} = \frac{1 + 0.2(0.316 - 0.5) + 0.316^2}{2(0.316)^2} = 5.323$$

$$\bar{F} = \beta - \sqrt{\beta^2 - \frac{1}{\bar{\lambda}^2}} = 5.323 - \sqrt{5.323^2 - \frac{1}{0.316^2}} = 1.043 \text{ MPa}$$

Clause 12.1.2 Flat webs without stiffeners

For one of the four webs:

$$F_{sc} = F_0 \bar{F} = (144 \text{ MPa})(1.043) = 150.164 \text{ MPa}$$

$$V_r = \phi_y h w F_{sc} = (0.9)(70.39 \text{ mm})(4.5 \text{ mm})(150.164 \text{ MPa}) = 42.809 \text{ kN}$$

For all four webs:

$$V_r = 4 \times V_r = 4 \times 42.809 \text{ kN} = 171.234 \text{ kN}$$

Peak Load and Deflection

$$P_r = 2V_r = 2(171.234 \text{ kN}) = 342.5 \text{ kN}$$

$$\Delta = \frac{PL^3}{48EI} = \frac{(342.5 \times 10^3 \text{ N})(2000 \text{ mm})^3}{48(70,000 \text{ MPa})(6.18 \times 10^6 \text{ mm}^4)} = 132 \text{ mm}$$

B.1.3 Bearing

For one of the four webs:

Clause 12.3 Web Crippling

$$k = 0.5 \left[1 + \frac{e}{\frac{n}{2+h}} \right] = 0.5 \left[1 + \frac{66.75 \text{ mm}}{\frac{75 \text{ mm}}{2 + 70.39 \text{ mm}}} \right] = 32.714 > 1 \Rightarrow k = 1$$

Clause 7.5.2.1 Elements bending in their own plane

$$\sigma_c = f_1 = \frac{My_{Top}}{I} = \frac{(1 \text{ Nmm})(36.46)}{6.18 \times 10^6 \text{ mm}^4} = 5.903 \times 10^{-6}$$

$$\sigma_t = f_2 = \frac{My_{Bottom}}{I} = \frac{(1 \text{ Nmm})(-52.04)}{6.18 \times 10^6 \text{ mm}^4} = -8.559 \times 10^{-6}$$

$$\frac{f_1}{f_2} = \frac{5.903 \times 10^{-6}}{-8.559 \times 10^{-6}} = -1.450 < -1$$

$$m = \frac{1.3}{1 - \frac{f_1}{f_2}} = \frac{1.3}{1 - (-1.450)} = 0.531$$

$$\lambda = \frac{mb}{t} = \frac{(0.531)(75 \text{ mm})}{4. \text{ mm}} = 8.844$$

Clause 10.1.2 Normalized Slenderness

$$\bar{\lambda} = \frac{\lambda}{\pi} \sqrt{\frac{F_0}{E}} = \frac{8.844}{\pi} \sqrt{\frac{240 \text{ MPa}}{70,000 \text{ MPa}}} = 0.165$$

Clause 10.1.3 Buckling stress

$\alpha = 0.2$ for unwelded fully heat-treated columns, beams, and elements $\bar{\lambda}_0 = 0.5$ for elements

$$\beta = \frac{1 + \alpha(\bar{\lambda} - \bar{\lambda}_0) + \bar{\lambda}^2}{2\bar{\lambda}^2} = \frac{1 + 0.2(0.165 - 0.5) + 0.165^2}{2(0.165)^2} = 17.667$$

$$\bar{F} = \beta - \sqrt{\beta^2 - \frac{1}{\bar{\lambda}^2}} = 17.667 - \sqrt{17.667^2 - \frac{1}{0.165^2}} = 1.074 \text{ MPa}$$

$$F_{bc} = F_c = \bar{F}F_0 = (1.074)(240 \text{ MPa}) = 257.800 \text{ MPa}$$

Clause 12.3 Web crippling

$$f_{bf} = \sigma_c = \frac{M_{max}y}{I} = \frac{(22.783 \times 10^6 \text{ Nmm})(36.462 \text{ mm})}{(6.18 \times 10^6 \text{ mm}^4)} = 135.000 \text{ MPa}$$

$$F'_c = \frac{\pi^2 E w^2}{4h^2} \left[1 - \left(\frac{f_{bf}}{F_{bc}} \right)^2 \right] = \frac{\pi^2 (70,000 \text{ MPa})(4.5 \text{ mm})^2}{4(70.39 \text{ mm})^2} \left[1 - \left(\frac{135 \text{ MPa}}{257.8 \text{ MPa}} \right)^2 \right] = 513.755 \text{ MPa}$$

For flat webs:

$$C_r = \phi_y k(n+h)wF'_c = (0.9)(1)(75 \text{ mm} + 70.39 \text{ mm})(4.5 \text{ mm})(513.755 \text{ MPa}) = 302.514 \text{ kN}$$

or

$$C_r = \phi_y n m F_y = (0.9)(75 \text{ mm})(4.5 \text{ mm})(240 \text{ MPa}) = 72.900 \text{ kN} \Rightarrow \text{governs!}$$

For all four webs:

$$C_r = 4C_r = 4(72.900 \text{ kN}) = 291.6 \text{ kN}$$

Peak Load and Deflection

$$P_r = 2R_r = 2(291.6 \text{ kN}) = 583.2 \text{ kN}$$

$$\Delta = \frac{PL^3}{48EI} = \frac{(583.2 \times 10^3 \text{ N})(2000 \text{ mm})^3}{48(70,000 \text{ MPa})(6.18 \times 10^6 \text{ mm}^4)} = 225 \text{ mm}$$

B.2 CSA S157 Properties and Resistance Factors

The results of the beam calculations with resistance factors and CSA S157 material properties are found in this section.

Table B.1: CSA S157 calculations for 1B-T with CSA S157 material properties.

Variables			Bending		Shear			Bearing	
w or t	4.5	mm	a/w	15.642	Fo	144	MPa	k calculated	32.714
a or h	70.39	mm	2.5b/t	42.569	λ_s	21.899		k actual	1
b	110.68	mm	ok?	ok	λ bar	0.316		f1	5.90E-06 MPa
t	6.5	mm	m	1.434	β	5.318		f2	-8.56E-06 MPa
Span Length	2	m	m<1.65?	ok	F bar	1.043	MPa	f2/f1	-1.450 <-1
Full Length	2133.5	mm	λ	24.413	Fsc	150.164		m	0.531
e	66.75	mm	λ bar	0.455	Vr	171.2	kN	λ	8.844
n	75	mm	0.3< λ bar<0.5	yes	Pr	342.5	kN	λ bar	0.165
M	1	Nmm	Mr (comp)	36.589	Δ_{max}	132	mm	β	17.667
I	6.18E+06	mm ⁴	Mr (tension)	22.783	Pf (DLA + α L)	143.9	kN	F bar	1.074 MPa
y pos	36.462	mm	Mr	22.8				F bc	257.800 MPa
y neg	-52.863	mm	Pr	45.6				f bf	135 MPa
Fy	240	MPa	Δ_{max}	18				F'c	513.755 MPa
Fu	260	MPa	Pf (DLA + α L)	19.1				Cr (buckling)	302.514 kN
E	70000	MPa						Cr (crushing)	72.900 kN
α	0.2							Cr	291.6 kN
λ bar o	0.5							Pr	583.2 kN
M max	2.278E+07	Nmm						Δ_{max}	225 mm
phi y	0.9							Pf (DLA + α L)	245.0 kN
phi u	0.75								

Table B.2: CSA S157 calculations for 2B-T & 2B-G with CSA S157 material properties.

Variables		Bending		Shear		Bearing	
w or t	4.5 mm	a/w	15.642	Fo	144 MPa	k calculated	32.714
a or h	70.39 mm	2.5b/t	42.569	λ_s	21.899	k actual	1
b	110.68 mm	ok?	ok	λ bar	0.316	f1	2.95E-06 MPa
t	6.5 mm	m	1.434	β	5.318	f2	-4.28E-06 MPa
Span Length	2 m	m<1.65?	ok	F bar	1.043 MPa	f2/f1	-1.450 <-1
Full Length	2133.5 mm	λ	24.413	Fsc	150.164	m	0.531
e	66.75 mm	λ bar	0.455	Vr	171.2 kN	λ	8.844
n	75 mm	0.3< λ bar<0.5	yes	Pr	342.5 kN	λ bar	0.165
M	1 Nmm	Mr (comp)	73.178 kNm	Δ_{max}	66 mm	β	17.667
I	1.24E+07 mm ⁴	Mr (tension)	45.567 kNm	Pf (DLA + α L)	143.9 kN	F bar	1.074 MPa
y pos	36.462 mm	Mr	45.6 kNm			F bc	257.800 MPa
y neg	-52.863 mm	Pr	91.1 kN			f bf	135 MPa
Fy	240 MPa	Δ_{max}	18 mm			F'c	513.755 MPa
Fu	260 MPa	Pf (DLA + α L)	38.3 kN			Cr (buckling)	302.514 kN
E	70000 MPa					Cr (crushing)	72.900 kN
α	0.2					Cr	291.6 kN
λ bar o	0.5					Pr	583.2 kN
M max	4.557E+07 Nmm					Δ_{max}	112 mm
phi y	0.9					Pf (DLA + α L)	245.0 kN
phi u	0.75						

Table B.3: CSA S157 calculations for 3B-M with CSA S157 material properties.

Variables		Bending		Shear		Bearing	
w or t	4.5 mm	a/w	15.642	Fo	144 MPa	k calculated	32.714
a or h	70.39 mm	2.5b/t	42.569	λ_s	21.899	k actual	1
b	110.68 mm	ok?	ok	λ bar	0.316	f1	1.97E-06 MPa
t	6.5 mm	m	1.434	β	5.318	f2	-2.85E-06 MPa
Span Length	2 m	m<1.65?	ok	F bar	1.043 MPa	f2/f1	-1.450 <-1
Full Length	2133.5 mm	λ	24.413	Fsc	150.164	m	0.531
e	66.75 mm	λ bar	0.455	Vr	171.2 kN	λ	8.844
n	75 mm	0.3< λ bar<0.5	yes	Pr	342.5 kN	λ bar	0.165
M	1 Nmm	Mr (comp)	109.766 kNm	Δ max	44 mm	β	17.667
I	1.85E+07 mm ⁴	Mr (tension)	68.350 kNm	Pf (DLA + α L)	143.9 kN	F bar	1.074 MPa
y pos	36.462 mm	Mr	68.4 kNm			F bc	257.800 MPa
y neg	-52.863 mm	Pr	136.7 kN			f bf	135 MPa
Fy	240 MPa	Δ max	18 mm			F'c	513.755 MPa
Fu	260 MPa	Pf (DLA + α L)	57.4 kN			Cr (buckling)	302.514 kN
E	70000 MPa					Cr (crushing)	72.900 kN
α	0.2					Cr	291.6 kN
λ bar o	0.5					Pr	583.2 kN
M max	6.835E+07 Nmm					Δ max	75 mm
phi y	0.9					Pf (DLA + α L)	245.0 kN
phi u	0.75						

Table B.4: CSA S157 calculations for 650 mm with CSA S157 material properties.

Variables			Bending			Shear			Bearing		
w or t	4.5	mm	a/w	15.642		Fo	144	MPa	k calculated	42.293	
a or h	70.39	mm	2.5b/t	42.569		λ_s	21.899		k actual	1	
b	110.68	mm	ok?	ok		λ bar	0.316		f1	5.90E-06	MPa
t	6.5	mm	m	1.434		β	5.318		f2	-8.56E-06	MPa
Span Length	0.65	m	m<1.65?	ok		F bar	1.043	MPa	f2/f1	-1.450	<-1
Full Length	736.6	mm	λ	24.413		Fsc	150.164		m	0.531	
e	43.3	mm	λ bar	0.455		Vr	171.2	kN	λ	4.422	
n	37.5	mm	0.3< λ bar<0.5	yes		Pr	342.5	kN	λ bar	0.082	
M	1	Nmm	Mr (comp)	36.589	kNm	Δ_{max}	5	mm	β	67.956	
I	6.18E+06	mm ⁴	Mr (tension)	22.783	kNm	Pf (DLA + α L)	143.9	kN	F bar	1.092	MPa
y pos	36.462	mm	Mr	22.8	kNm				F bc	262.049	MPa
y neg	-52.863	mm	Pr	140.2	kN				f bf	135	MPa
Fy	240	MPa	Δ_{max}	2	mm				F'c	519.935	MPa
Fu	260	MPa	Pf (DLA + α L)	58.9	kN				Cr (buckling)	227.188	kN
E	70000	MPa							Cr (crushing)	36.450	kN
α	0.2								Cr	145.8	kN
λ bar o	0.5								Pr	291.6	kN
M max	2.278E+07	Nmm							Δ_{max}	4	mm
phi y	0.9								Pf (DLA + α L)	122.5	kN
phi u	0.75										

B.3 Mill Certificate Properties and Resistance Factors Set to Unity

The results of the beam calculations with no resistance factors and mill certificate material properties are found in this section.

Table B.5: CSA S157 calculations for 1B-T with mill certificate material properties.

Variables		Bending		Shear		Bearing	
w or t	4.5 mm	a/w	15.642	Fo	159.72 MPa	k calculated	32.714
a or h	70.39 mm	2.5b/t	42.569	λ_s	21.899	k actual	1
b	110.68 mm	ok?	ok	λ bar	0.333	f1	5.90E-06 MPa
t	6.5 mm	m	1.434	β	4.859	f2	-8.56E-06 MPa
Span Length	2 m	m<1.65?	ok	F bar	1.039 MPa	f2/f1	-1.450 <-1
Full Length	2133.5 mm	λ	24.413	Fsc	165.987	m	0.531
e	66.75 mm	λ bar	0.479	Vr	210.3 kN	λ	8.844
n	75 mm	0.3< λ bar<0.5	yes	Pr	420.6 kN	λ bar	0.174
M	1 Nmm	Mr (comp)	45.092 kNm	Δ_{max}	162 mm	β	16.007
I	6.18E+06 mm ⁴	Mr (tension)	34.596 kNm	Pf (DLA + α L)	176.7 kN	F bar	1.072 MPa
y pos	36.462 mm	Mr	34.6 kNm			F bc	285.457 MPa
y neg	-52.863 mm	Pr	69.2 kN			f bf	204 MPa
Fy	266.2 MPa	Δ_{max}	27 mm			F'c	344.557 MPa
Fu	296.1 MPa	Pf (DLA + α L)	29.1 kN			Cr (buckling)	225.428 kN
E	70000 MPa					Cr (crushing)	89.843 kN
α	0.2					Cr	359.4 kN
λ bar o	0.5					Pr	718.7 kN
M max	3.460E+07 Nmm					Δ_{max}	277 mm
phi y	1					Pf (DLA + α L)	302.0 kN
phi u	1						

Table B.6: CSA S157 calculations for 2B-T & 2B-G with mill certificate material properties.

Variables			Bending		Shear		Bearing		
w or t	4.5	mm	a/w	15.642	Fo	159.72	MPa	k calculated	32.714
a or h	70.39	mm	2.5b/t	42.569	λ_s	21.899		k actual	1
b	110.68	mm	ok?	ok	λ bar	0.333		f1	2.95E-06 MPa
t	6.5	mm	m	1.434	β	4.859		f2	-4.28E-06 MPa
Span Length	2	m	m<1.65?	ok	F bar	1.039	MPa	f2/f1	-1.450 <-1
Full Length	2133.5	mm	λ	24.413	Fsc	165.987		m	0.531
e	66.75	mm	λ bar	0.479	Vr	210.3	kN	λ	8.844
n	75	mm	0.3< λ bar<0.5	yes	Pr	420.6	kN	λ bar	0.174
M	1	Nmm	Mr (comp)	90.185	Δ_{max}	81	mm	β	16.007
I	1.24E+07	mm ⁴	Mr (tension)	69.191	Pf (DLA + α L)	176.7	kN	F bar	1.072 MPa
y pos	36.462	mm	Mr	69.2				F bc	285.457 MPa
y neg	-52.863	mm	Pr	138.4				f bf	204 MPa
Fy	266.2	MPa	Δ_{max}	27				F'c	344.557 MPa
Fu	296.1	MPa	Pf (DLA + α L)	58.1				Cr (buckling)	225.428 kN
E	70000	MPa						Cr (crushing)	89.843 kN
α	0.2							Cr	359.4 kN
λ bar o	0.5							Pr	718.7 kN
M max	6.919E+07	Nmm						Δ_{max}	139 mm
phi y	1							Pf (DLA + α L)	302.0 kN
phi u	1								

Table B.7: CSA S157 calculations for 3B-M with mill certificate material properties.

Variables		Bending		Shear		Bearing	
w or t	4.5 mm	a/w	15.642	Fo	159.72 MPa	k calculated	32.714
a or h	70.39 mm	2.5b/t	42.569	λ_s	21.899	k actual	1
b	110.68 mm	ok?	ok	λ bar	0.333	f1	1.97E-06 MPa
t	6.5 mm	m	1.434	β	4.859	f2	-2.85E-06 MPa
Span Length	2 m	m<1.65?	ok	F bar	1.039 MPa	f2/f1	-1.450 <-1
Full Length	2133.5 mm	λ	24.413	Fsc	165.987	m	0.531
e	66.75 mm	λ bar	0.479	Vr	210.3 kN	λ	8.844
n	75 mm	0.3< λ bar<0.5	yes	Pr	420.6 kN	λ bar	0.174
M	1 Nmm	Mr (comp)	135.277 kNm	Δ max	54 mm	β	16.007
I	1.85E+07 mm ⁴	Mr (tension)	103.787 kNm	Pf (DLA + α L)	176.7 kN	F bar	1.072 MPa
y pos	36.462 mm	Mr	103.8 kNm			F bc	285.457 MPa
y neg	-52.863 mm	Pr	207.6 kN			f bf	204 MPa
Fy	266.2 MPa	Δ max	27 mm			F'c	344.557 MPa
Fu	296.1 MPa	Pf (DLA + α L)	87.2 kN			Cr (buckling)	225.428 kN
E	70000 MPa					Cr (crushing)	89.843 kN
α	0.2					Cr	359.4 kN
λ bar o	0.5					Pr	718.7 kN
M max	1.038E+08 Nmm					Δ max	92 mm
phi y	1					Pf (DLA + α L)	302.0 kN
phi u	1						

Table B.8: CSA S157 calculations for 650 mm with mill certificate material properties.

Variables			Bending		Shear		Bearing		
w or t	4.5	mm	a/w	15.642	Fo	159.72	MPa	k calculated	42.293
a or h	70.39	mm	2.5b/t	42.569	λ_s	21.899		k actual	1
b	110.68	mm	ok?	ok	λ bar	0.333		f1	5.90E-06 MPa
t	6.5	mm	m	1.434	β	4.859		f2	-8.56E-06 MPa
Span Length	0.65	m	m<1.65?	ok	F bar	1.039	MPa	f2/f1	-1.450 <-1
Full Length	736.6	mm	λ	24.413	Fsc	165.987		m	0.531
e	43.3	mm	λ bar	0.479	Vr	210.3	kN	λ	4.422
n	37.5	mm	0.3< λ bar<0.5	yes	Pr	420.6	kN	λ bar	0.087
M	1	Nmm	Mr (comp)	45.092	Δ_{max}	6	mm	β	61.375
I	6.18E+06	mm ⁴	Mr (tension)	34.596	Pf (DLA + α L)	176.7	kN	F bar	1.091 MPa
y pos	36.462	mm	Mr	34.6				F bc	290.397 MPa
y neg	-52.863	mm	Pr	212.9				f bf	204 MPa
Fy	266.2	MPa	Δ_{max}	3				F'c	356.748 MPa
Fu	296.1	MPa	Pf (DLA + α L)	89.5				Cr (buckling)	173.203 kN
E	70000	MPa						Cr (crushing)	44.921 kN
α	0.2							Cr	179.7 kN
λ bar o	0.5							Pr	359.4 kN
M max	3.460E+07	Nmm						Δ_{max}	5 mm
phi y	1							Pf (DLA + α L)	151.0 kN
phi u	1								

Appendix C

Deck-to-Girder Parametric Study Results

This appendix contains the FE results of the parametric study discussed in [Chapter 6](#).

C.1 Thermal Expansion

Table C.1: Spring force in N with large cross-section and varying deck width (Part 1).

	L [m]	40	40	40
Steel Properties	d [mm]	1250	1250	1250
	w [mm]	13	13	13
	b [mm]	300	300	300
	t [mm]	25	25	25
	A [mm ²]	30600	30600	30600
	I [mm ⁴]	7.50E+09	7.50E+09	7.50E+09
Aluminum Properties	Deck Thickness [mm]	6	6	6
	Deck Width [mm]	686	1372	2744
Temperature Properties	Max Temp. [C]	51	51	51
	Temp. Gradient [C]	10	10	10
Transformed Section Properties	n	2.857	2.857	2.857
	Transformed Deck Width [mm]	240.1	480.2	960.4
	Transformed Area [mm]	32040.6	33481.2	36362.4
	Transformed Centroid [mm]	653.24	679.04	724.52
	Transformed Moment of Inertia [mm ⁴]	8.04E+09	8.54E+09	9.41E+09
	Stiffness [N/mm]			
Spring Force [N]	1.00E+00	8	8	8
	1.00E+01	81	82	82
	1.00E+02	713	759	784
	1.00E+03	3558	4561	5431
	1.00E+04	10034	13613	17683
	1.00E+05	20920	29364	37644
	1.00E+06	28679	40108	50465
	1.00E+07	30224	42210	52927
	1.00E+08	30395	42444	53200
	1.00E+09	30413	42467	53227
1.00E+10	30415	42470	53230	

Table C.2: Spring force in N with large cross-section and varying deck width (Part 2).

	L [m]	40	40	40	40	40	40	40	40	40	40	40	40	40
Steel Properties	d [mm]	1250	1250	1250	1250	1250	1250	1250	1250	1250	1250	1250	1250	1250
	w [mm]	13	13	13	13	13	13	13	13	13	13	13	13	13
	b [mm]	300	300	300	300	300	300	300	300	300	300	300	300	300
	t [mm]	25	25	25	25	25	25	25	25	25	25	25	25	25
	A [mm ²]	30600	30600	30600	30600	30600	30600	30600	30600	30600	30600	30600	30600	30600
I [mm ⁴]	7.50E+09	7.50E+09	7.50E+09	7.50E+09	7.50E+09	7.50E+09	7.50E+09	7.50E+09	7.50E+09	7.50E+09	7.50E+09	7.50E+09	7.50E+09	
Aluminum Properties	Deck Thickness [mm]	6	6	6	6	6	6	6	6	6	6	6	6	6
	Deck Width [mm]	100	200	300	400	500	600	700	800	900	1000			
Temperature Properties	Max Temp. [°C]	51	51	51	51	51	51	51	51	51	51	51	51	51
	Temp. Gradient [°C]	10	10	10	10	10	10	10	10	10	10	10	10	10
Transformed Section Properties	n	2.857	2.857	2.857	2.857	2.857	2.857	2.857	2.857	2.857	2.857	2.857	2.857	2.857
	Transformed Deck Width [mm]	35	70	105	140	175	210	245	280	315	350			
	Transformed Area [mm]	30810	31020	31230	31440	31650	31860	32070	32280	32490	32700			
	Transformed Centroid [mm]	629.28	633.50	637.67	641.78	645.83	649.84	653.79	657.68	661.53	665.33			
	Transformed Moment of Inertia [mm ⁴]	7.58E+09	7.66E+09	7.74E+09	7.82E+09	7.90E+09	7.98E+09	8.05E+09	8.13E+09	8.20E+09	8.28E+09			
Stiffness [N/mm]														
Spring Force	1.00E+10	5793	12535	17209	21224	24704	28110	30724	33031	35085	37054			

Table C.3: Spring force in N with large cross-section and varying deck width (Part 3).

	L [m]	40	40	40	40	40	40	40
Steel Properties	d [mm]	1250	1250	1250	1250	1250	1250	1250
	w [mm]	13	13	13	13	13	13	13
	b [mm]	300	300	300	300	300	300	300
	t [mm]	25	25	25	25	25	25	25
	A [mm ²]	30600	30600	30600	30600	30600	30600	30600
	I [mm ⁴]	7.50E+09	7.50E+09	7.50E+09	7.50E+09	7.50E+09	7.50E+09	7.50E+09
Aluminum Properties	Deck Thickness [mm]	6	6	6	6	6	6	6
	Deck Width [mm]	1100	1200	1300	1400	1500	2500	3500
Temperature Properties	Max Temp. [°C]	51	51	51	51	51	51	51
	Temp. Gradient [°C]	10	10	10	10	10	10	10
Transformed Section Properties	n	2.857	2.857	2.857	2.857	2.857	2.857	2.857
	Transformed Deck Width [mm]	385	420	455	490	525	875	1225
	Transformed Area [mm]	32910	33120	33330	33540	33750	35850	37950
	Transformed Centroid [mm]	669.08	672.78	676.44	680.05	683.61	716.97	746.63
	Transformed Moment of Inertia [mm ⁴]	8.35E+09	8.42E+09	8.49E+09	8.56E+09	8.63E+09	9.27E+09	9.84E+09
	Stiffness [N/mm]							
Spring Force	1.00E+10	38695	40185	41546	42839	43981	51919	56424

Table C.4: Spring force in N with large cross-section and varying deck thickness.

	L [m]	40	40	40	40	40
Steel Properties	d [mm]	1250	1250	1250	1250	1250
	w [mm]	13	13	13	13	13
	b [mm]	300	300	300	300	300
	t [mm]	25	25	25	25	25
	A [mm ²]	30600	30600	30600	30600	30600
	I [mm ⁴]	7.50E+09	7.50E+09	7.50E+09	7.50E+09	7.50E+09
Aluminum Properties	Deck Thickness [mm]	1.5	3	6	12	24
	Deck Width [mm]	1372	1372	1372	1372	1372
Temperature Properties	Max Temp. [C]	51	51	51	51	51
	Temp. Gradient [C]	10	10	10	10	10
Transformed Section Properties	n	2.857	2.857	2.857	2.857	2.857
	Transformed Deck Width [mm]	480.2	480.2	480.2	480.2	480.2
	Transformed Area [mm ²]	31320.3	32040.6	33481.2	36362.4	42124.8
	Transformed Centroid [mm]	639.39	653.17	679.04	725.00	799.27
	Transformed Moment of Inertia [mm ⁴]	7.78E+09	8.04E+09	8.54E+09	9.43E+09	1.09E+10
	Stiffness [N/mm]					
Spring Force [N]	1.00E+00		8	8	8	
	1.00E+01		82	82	82	
	1.00E+02		712	759	785	
	1.00E+03		3506	4561	5478	
	1.00E+04		9428	13613	18670	
	1.00E+05		17849	29364	43496	
	1.00E+06		21428	40108	67080	
	1.00E+07		22334	42210	73296	
	1.00E+08		22396	42444	74040	
	1.00E+09		22403	42467	74116	
1.00E+10	2835	22403	42470	74124	115537	

Table C.5: Spring force in N with large cross-section and constant deck area.

	L [m]	40	40	40	40	40	40	40
Steel Properties	d [mm]	1250	1250	1250	1250	1250	1250	1250
	w [mm]	13	13	13	13	13	13	13
	b [mm]	300	300	300	300	300	300	300
	t [mm]	25	25	25	25	25	25	25
	A [mm ²]	30600	30600	30600	30600	30600	30600	30600
	I [mm ⁴]	7.50E+09	7.50E+09	7.50E+09	7.50E+09	7.50E+09	7.50E+09	7.50E+09
Aluminum Properties	Deck Thickness [mm]	1.5	3	4.5	6	9	12	24
	Deck Width [mm]	5488	2744	1829.3	1372	914.7	686	343
	Deck Area [mm ²]	8232	8232	8231.85	8232	8232.3	8232	8232
Temperature Properties	Max Temp. [°C]	51	51	51	51	51	51	51
	Temp. Gradient [°C]	10	10	10	10	10	10	10
Transformed Section Properties	n	2.857	2.857	2.857	2.857	2.857	2.857	2.857
	Transformed Deck Width [mm]	1920.8	960.4	640.255	480.2	320.145	240.1	120.05
	Transformed Area [mm ²]	33481.2	33481.2	33481.15	33481.2	33481.31	33481.2	33481.2
	Transformed Centroid [mm]	678.85	678.91	678.98	679.04	679.17	679.30	679.82
	Transformed Moment of Inertia [mm ⁴]	8.53E+09	8.53E+09	8.54E+09	8.54E+09	8.54E+09	8.55E+09	8.57E+09
	Stiffness [N/mm]							
Spring Force	1.00E+10	19332	29560	36781	42157	49462	54114	62106

Table C.6: Spring force in N with large cross-section and varying span length.

	L [m]	5.12	10.24	20.16	40
Steel Properties	d [mm]	1250	1250	1250	1250
	w [mm]	13	13	13	13
	b [mm]	300	300	300	300
	t [mm]	25	25	25	25
	A [mm ²]	30600	30600	30600	30600
	I [mm ⁴]	7.50E+09	7.50E+09	7.50E+09	7.50E+09
Aluminum Properties	Deck Thickness [mm]	6	6	6	6
	Deck Width [mm]	1372	1372	1372	1372
Temperature Properties	Max Temp. [C]	51	51	51	51
	Temp. Gradient [C]	10	10	10	10
Transformed Section Properties	n	2.857	2.857	2.857	2.857
	Transformed Deck Width [mm]	480.2	480.2	480.2	480.2
	Transformed Area [mm]	33481.2	33481.2	33481.2	33481.2
	Transformed Centroid [mm]	679.04	679.04	679.04	679.04
	Transformed Moment of Inertia [mm ⁴]	8.54E+09	8.54E+09	8.54E+09	8.54E+09
	Stiffness [N/mm]				
Spring Force [N]	1.00E+00				8
	1.00E+01				82
	1.00E+02				759
	1.00E+03				4561
	1.00E+04				13613
	1.00E+05				29364
	1.00E+06				40108
	1.00E+07				42210
	1.00E+08				42444
	1.00E+09				42467
	1.00E+10	40986	42144	42156	42470

Table C.7: Spring force in N with small cross-section and varying deck thickness and deck width.

		Deck Thickness			Deck Width		
L [m]		20.16	20.16	20.16	20.16	20.16	20.16
Steel Properties	d [mm]	688	688	688	688	688	688
	w [mm]	13	13	13	13	13	13
	b [mm]	300	300	300	300	300	300
	t [mm]	21	21	21	21	21	21
	A [mm ²]	20998	20998	20998	20998	20998	20998
	I [mm ⁴]	1.69E+09	1.69E+09	1.69E+09	1.69E+09	1.69E+09	1.69E+09
Aluminum Properties	Deck Thickness [mm]	3	6	12	6	6	6
	Deck Width [mm]	1372	1372	1372	686	1372	2744
Temperature Properties	Max Temp. [°C]	51	51	51	51	51	51
	Temp. Gradient [°C]	10	10	10	10	10	10
Transformed Section Properties	n	2.857	2.857	2.857	2.857	2.857	2.857
	Transformed Deck Width [mm]	480.2	480.2	480.2	240.1	480.2	960.4
	Transformed Area [mm]	22438.6	23879.2	26760.4	22438.6	23879.2	26760.4
	Transformed Centroid [mm]	366.18	385.87	419.37	366.28	385.87	418.72
	Transformed Moment of Inertia [mm ⁴]	1.85E+09	2.00E+09	2.25E+09	1.86E+09	2.00E+09	2.24E+09
Stiffness [N/mm]							
Spring Force [N]	1.00E+00	4	4	4	4	4	4
	1.00E+01	41	41	41	41	41	41
	1.00E+02	396	404	407	397	404	407
	1.00E+03	2821	3255	3527	2872	3255	3492
	1.00E+04	9132	12676	16426	9552	12676	15674
	1.00E+05	17572	27650	39052	20316	27650	34274
	1.00E+06	21399	37483	59039	27739	37483	45690
	1.00E+07	21966	39330	63918	29162	39330	47799
	1.00E+08	22026	39533	64488	29319	39533	48029
	1.00E+09	22032	39553	64546	29334	39553	48053
1.00E+10	22033	39555	64552	29336	39555	48055	

C.2 Vehicle Braking

Table C.8: Spring force in N with large cross-section and varying vehicle location (Part 1).

		Gravity		
		Arriving	Middle	Exiting
L [m]		40	40	40
Steel Properties	d [mm]	1250	1250	1250
	w [mm]	13	13	13
	b [mm]	300	300	300
	t [mm]	25	25	25
	A [mm ²]	30600	30600	30600
	I [mm ⁴]	7.50E+09	7.50E+09	7.50E+09
Aluminum Properties	Deck Thickness [mm]	6	6	6
	Deck Width [mm]	1372	1372	1372
Vehicle Braking Properties	Gravity [kN]	53.1	53.1	53.1
	Braking [kN]			
Transformed Section Properties	n	2.857	2.857	2.857
	Transformed Deck Width [mm]	480.2	480.2	480.2
	Transformed Area [mm ²]	33481.2	33481.2	33481.2
	Transformed Centroid [mm]	679.04	679.04	679.04
	Transformed Moment of Inertia [mm ⁴]	8.54E+09	8.54E+09	8.54E+09
Stiffness [N/mm]				
Spring Force [N]	1.00E+00	0	2	0
	1.00E+01	0	21	0
	1.00E+02	5	192	5
	1.00E+03	47	985	47
	1.00E+04	392	1554	392
	1.00E+05	1679	1620	1679
	1.00E+06	2599	1665	2599
	1.00E+07	2754	1674	2754
	1.00E+08	2770	1675	2770
	1.00E+09	2772	1675	2772
	1.00E+10	2772	1675	2772

Table C.9: Spring force in N with large cross-section and varying vehicle location (Part 2).

		Gravity & Braking			Braking	
		Arriving	Middle	Exiting	Arriving	Middle
L [m]		40	40	40	40	40
Steel Properties	d [mm]	1250	1250	1250	1250	1250
	w [mm]	13	13	13	13	13
	b [mm]	300	300	300	300	300
	t [mm]	25	25	25	25	25
	A [mm ²]	30600	30600	30600	30600	30600
	I [mm ⁴]	7.50E+09	7.50E+09	7.50E+09	7.50E+09	7.50E+09
Aluminum Properties	Deck Thickness [mm]	6	6	6	6	6
	Deck Width [mm]	1372	1372	1372	1372	1372
Vehicle Braking Properties	Gravity [kN]	53.1	53.1	53.1		
	Braking [kN]	13.3	13.3	13.3	13.3	13.3
Transformed Section Properties	n	2.857	2.857	2.857	2.857	2.857
	Transformed Deck Width [mm]	480.2	480.2	480.2	480.2	480.2
	Transformed Area [mm ²]	33481.2	33481.2	33481.2	33481.2	33481.2
	Transformed Centroid [mm]	679.04	679.04	679.04	679.04	679.04
	Transformed Moment of Inertia [mm ⁴]	8.54E+09	8.54E+09	8.54E+09	8.54E+09	8.54E+09
Stiffness [N/mm]						
Spring Force [N]	1.00E+00	106	19	106	106	106
	1.00E+01	111	114	110		106
	1.00E+02	161	291	148		114
	1.00E+03	560	1063	423		181
	1.00E+04	2963	1586	1838	2624	522
	1.00E+05	9798	1646	6024		1445
	1.00E+06	13941	2123	8812	11816	2225
	1.00E+07	14737	2255	9282		2383
	1.00E+08	14823	2270	9332	12368	2400
	1.00E+09	14832	2271	9337		2402
	1.00E+10	14833	2271	9338	12374	2402

Table C.10: Spring force in N with large cross-section, vehicle braking at middle location, and varying span length.

	Gravity				Gravity and Braking			
	5.12	10.24	20.16	40	5.12	10.24	20.16	40
L [m]	1250	1250	1250	1250	1250	1250	1250	1250
d [mm]	13	13	13	13	13	13	13	13
w [mm]	300	300	300	300	300	300	300	300
b [mm]	25	25	25	25	25	25	25	25
t [mm]	30600	30600	30600	30600	30600	30600	30600	30600
A [mm^2]	7.50E+09	7.50E+09	7.50E+09	7.50E+09	7.50E+09	7.50E+09	7.50E+09	7.50E+09
I [mm^4]								
Deck Thickness [mm]	6	6	6	6	6	6	6	6
Deck Width [mm]	1372	1372	1372	1372	1372	1372	1372	1372
Gravity [kN]	53.1	53.1	53.1	53.1	53.1	53.1	53.1	53.1
Braking [kN]					13.3	13.3	13.3	13.3
n	2.857	2.857	2.857	2.857	2.857	2.857	2.857	2.857
Transformed Deck Width [mm]	480.2	480.2	480.2	480.2	480.2	480.2	480.2	480.2
Transformed Area [mm]	33481.2	33481.2	33481.2	33481.2	33481.2	33481.2	33481.2	33481.2
Transformed Centroid [mm]	679.04	679.04	679.04	679.04	679.04	679.04	679.04	679.04
Transformed Moment of Inertia [mm^4]	8.54E+09	8.54E+09	8.54E+09	8.54E+09	8.54E+09	8.54E+09	8.54E+09	8.54E+09
Stiffness [N/mm]								
Spring Force	1200	1616	1675	1675	1330	1710	2296	2271

Table C.11: Spring force in N with large cross-section, vehicle braking at arriving location, and varying span length.

	Gravity			Gravity and Braking				
	5.12	10.24	20.16	40	5.12	10.24	20.16	40
L [m]	1250	1250	1250	1250	1250	1250	1250	1250
d [mm]	13	13	13	13	13	13	13	13
w [mm]	300	300	300	300	300	300	300	300
b [mm]	25	25	25	25	25	25	25	25
t [mm]	30600	30600	30600	30600	30600	30600	30600	30600
A [mm^2]	7.50E+09	7.50E+09	7.50E+09	7.50E+09	7.50E+09	7.50E+09	7.50E+09	7.50E+09
I [mm^4]								
Deck Thickness [mm]	6	6	6	6	6	6	6	6
Deck Width [mm]	1372	1372	1372	1372	1372	1372	1372	1372
Gravity [kN]	53.1	53.1	53.1	53.1	53.1	53.1	53.1	53.1
Braking [kN]					13.3	13.3	13.3	13.3
n	2.857	2.857	2.857	2.857	2.857	2.857	2.857	2.857
Transformed Deck Width [mm]	480.2	480.2	480.2	480.2	480.2	480.2	480.2	480.2
Transformed Area [mm]	33481.2	33481.2	33481.2	33481.2	33481.2	33481.2	33481.2	33481.2
Transformed Centroid [mm]	679.04	679.04	679.04	679.04	679.04	679.04	679.04	679.04
Transformed Moment of Inertia [mm^4]	8.54E+09	8.54E+09	8.54E+09	8.54E+09	8.54E+09	8.54E+09	8.54E+09	8.54E+09
Stiffness [N/mm]								
Spring Force	2773	2773	2772	2772	14906	14864	14843	14833

Table C.12: Spring force in N with large cross-section, vehicle braking at arriving location, and varying deck width.

		Deck Width		
L [m]		40	40	40
Steel Properties	d [mm]	1250	1250	1250
	w [mm]	13	13	13
	b [mm]	300	300	300
	t [mm]	25	25	25
	A [mm ²]	30600	30600	30600
	I [mm ⁴]	7.50E+09	7.50E+09	7.50E+09
Aluminum Properties	Deck Thickness [mm]	6	6	6
	Deck Width [mm]	686	1372	2744
Vehicle Braking Properties	Gravity [kN]	53.1	53.1	53.1
	Braking [kN]	13.3	13.3	13.3
Transformed Section Properties	n	2.857	2.857	2.857
	Transformed Deck Width [mm]	240.1	480.2	960.4
	Transformed Area [mm ²]	32040.6	33481.2	36362.4
	Transformed Centroid [mm]	653.24	679.04	724.52
	Transformed Moment of Inertia [mm ⁴]	8.04E+09	8.54E+09	9.41E+09
Stiffness [N/mm]				
Spring Force [N]	1.00E+00		106	
	1.00E+01		111	
	1.00E+02		161	
	1.00E+03		560	
	1.00E+04		2963	
	1.00E+05	9923	9798	9706
	1.00E+06		13941	
	1.00E+07		14737	
	1.00E+08		14823	
	1.00E+09		14832	
	1.00E+10	14859	14833	14774

Table C.13: Spring force in N with large cross-section, vehicle braking at arriving location, and varying deck thickness.

		Deck Thickness						
L [m]		40	40	40	40	40	40	40
Steel Properties	d [mm]	1250	1250	1250	1250	1250	1250	1250
	w [mm]	13	13	13	13	13	13	13
	b [mm]	300	300	300	300	300	300	300
	t [mm]	25	25	25	25	25	25	25
	A [mm ²]	30600	30600	30600	30600	30600	30600	30600
	I [mm ⁴]	7.50E+09	7.50E+09	7.50E+09	7.50E+09	7.50E+09	7.50E+09	7.50E+09
Aluminum Properties	Deck Thickness [mm]	0.75	1.5	3	6	12	24	48
	Deck Width [mm]	1372	1372	1372	1372	1372	1372	1372
Vehicle Braking Properties	Gravity [kN]	53.1	53.1	53.1	53.1	53.1	53.1	53.1
	Braking [kN]	13.3	13.3	13.3	13.3	13.3	13.3	13.3
Transformed Section Properties	n	2.857	2.857	2.857	2.857	2.857	2.857	2.857
	Transformed Deck Width [mm]	480.2	480.2	480.2	480.2	480.2	480.2	480.2
	Transformed Area [mm]	30960.15	31320.3	32040.6	33481.2	36362.4	42124.8	53649.6
	Transformed Centroid [mm]	632.27	639.39	653.17	679.04	725.00	799.27	903.83
	Transformed Moment of Inertia [mm ⁴]	7.64E+09	7.78E+09	8.04E+09	8.54E+09	9.43E+09	1.09E+10	1.30E+10
Stiffness [N/mm]								
Spring Force [N]	1.00E+00			107	106	105	105	
	1.00E+01			117	111	109		
	1.00E+02			210	161	136		
	1.00E+03			897	560	370		
	1.00E+04			4491	2963	1959		
	1.00E+05			11139	9798	8295	7371	
	1.00E+06			13567	13941	14803		
	1.00E+07			13965	14737	16226		
	1.00E+08			14006	14823	16390		
	1.00E+09			14010	14832	16407		
1.00E+10	13459	13630	14010	14833	16408	18871	20914	

Table C.14: Spring force in N with small cross-section, vehicle braking at arriving location, and varying deck thickness and deck width.

		Deck Thickness			Deck Width		
L [m]		20.16	20.16	20.16	20.16	20.16	20.16
Steel Properties	d [mm]	688	688	688	688	688	688
	w [mm]	13	13	13	13	13	13
	b [mm]	300	300	300	300	300	300
	t [mm]	21	21	21	21	21	21
	A [mm ²]	20998	20998	20998	20998	20998	20998
	I [mm ⁴]	1.69E+09	1.69E+09	1.69E+09	1.69E+09	1.69E+09	1.69E+09
Aluminum Properties	Deck Thickness [mm]	3	6	12	6	6	6
	Deck Width [mm]	1372	1372	1372	686	1372	2744
Vehicle Braking Properties	Gravity [kN]	53.1	53.1	53.1	53.1	53.1	53.1
	Braking [kN]	13.3	13.3	13.3	13.3	13.3	13.3
Transformed Section Properties	n	2.857	2.857	2.857	2.857	2.857	2.857
	Transformed Deck Width [mm]	480.2	480.2	480.2	240.1	480.2	960.4
	Transformed Area [mm ²]	22438.6	23879.2	26760.4	22438.6	23879.2	26760.4
	Transformed Centroid [mm]	366.18	385.87	419.37	366.28	385.87	418.72
	Transformed Moment of Inertia [mm ⁴]	1.85E+09	2.00E+09	2.25E+09	1.86E+09	2.00E+09	2.24E+09
Stiffness [N/mm]							
Spring Force [N]	1.00E+00	209	208	207	208	208	208
	1.00E+01	216	212	210	213	212	211
	1.00E+02		250	231	263	250	243
	1.00E+03	912	596	428	685	596	549
	1.00E+04	4460	2935	1946	3155	2935	2804
	1.00E+05	11064	9676	8158	9827	9676	9575
	1.00E+06	13472	13795	14596	13881	13795	13715
	1.00E+07	13871	14573	15990	14648	14573	14493
	1.00E+08	13912	14658	16152	14731	14658	14579
	1.00E+09	13916	14667	16168	14739	14667	14588
1.00E+10	13917	14667	16170	14740	14667	14588	